Application of the Lattice Boltzmann Method for Analysing the Detachment of Micro-Sized Drug Particles from a Carrier Particle

Dissertation

zur Erlangung des
Doktorgrades der Ingenieurwissenschaften (Dr. -Ing.)

des

Zentrums für Ingenieurwissenschaften

der Martin-Luther-Universität
Halle-Wittenberg

vorgelegt

von Herr Yan Cui
geb. am 19.11.1985 in Anhui, China

Gutachter

1. Prof. Dr.-Ing. habil. Martin Sommerfeld
2. Prof. Mike Reeks

Tag der öffentlichen Verteidigung: 21.07.2016 in Halle

Preface

The present thesis is based on the research work I performed as a scientific assistant at the chair for Mechanical Process Engineering at the Martin-Luther-Universität Halle-Wittenberg from Sep. 2010 to Aug. 2014.

First of all, deepest gratitude has to be attributed to my supervisor, Prof. Martin Sommerfeld, who provided me an interesting and challenging project with excellent working conditions. Especially, I had the opportunity to attend many international conferences all over the world which resulted in lots useful discussions with the other groups and helped me to improve the contribution to the present work. Moreover, I've learned from Sommerfeld on how to handle a project in a scientific way. At this point the financial support of this research project by the Deutsche Forschungsgemeinschaft (DFG) in the frame of the priority research programme PiKo (Partikel im Kontakt) has to be acknowledged. Within PiKo, around 25 research groups from the Germany, Netherlands, Austria and Switzerland came together to break their heads about issues related to particles in contact. Special thanks to my project partner Sarah Zellnitz and Nora Anne Urbanetz from Technische Universität Graz, they did amazing experimental work and allowed the determination of detachment probability.

I'm also thankful to all my colleagues from the chair of Mechanical Process Engineering: Mathias Dietzel, who was the main developer of the LBM code, he kindly gave me many useful instructions about LBM; Martin Ernst, who was the second most important developer of the LBM code and the previous Linux administrator, he is a warm-hearted man and helped me very often in work; Zeeshan Qadir, who was my office roommate and came from our 'brother country', I have a wonderful memory in stay with him and we had many useful discussions about the work; Hai Li, who is the only compatriot in our group, we had lots useful discussion in the detachment model, he gained a big “thank you” for the careful proofreading of this thesis; Silvio Schmalfuß, who was my project partner, we had a good corporation of the project and he gave me a good instruction of OpenFOAM; Thomas Reichardt, who was my first office roommate and helped me quite often in the beginning of my work; Philipp Ruschke, who was the new Linux administrator and prepared the smooth-run computer cluster for our simulations. But also the other members of the institute should not be forgotten: Ali Darvan, Matthias Kuschel, Lars Pasternak, Stefan Horender, Carola Thomas, Maria Jose Moreno Manas, Daya Pandey, Sebastian Stübing, Oscar Sgrott, Brian Qointero Arboleda and Christine Wicke, all of them created a pleasant and humorous atmosphere in the office, thank you all very much!

Finally and the most importantly, I should thank my wife, Ran Zhang. She is my spiritual power and living support. Moreover, special thanks to my parents, Yuhua Cui and Ling Zhang, without their encouragement and support this work would not have been done.

Abstract

Pulmonary drug delivery by dry powder inhaler (DPI) is becoming more and more popular. The small drug particles are mostly blended with a larger carrier particle as one particle cluster for better dispersion by the breathing airstream. What's essential for a good performance of a DPI is the detachment of the drugs from the carrier surface through the fluid stresses and also impacts on walls. Fully resolved simulations based on the lattice Boltzmann method (LBM) were performed to study the influence of the laminar flow, the turbulent flow and the surface roughness on the fluid dynamic forces of the drugs. Moreover when the particle cluster collides onto a wall with a certain impact angle, the inertia force on the drug particle was solved numerically during the collision process. Based on those force studies, three detachment models, i.e. plane wall detachment model, rough wall detachment model and particle-wall collision detachment model, were developed to analyse the efficiency of drug delivery.

In the plane wall detachment study, first the lattice Boltzmann simulations were validated based on a test case where a single particle was situated on a wall and exposed to a linear shear flow. The present simulations were compared with analytical results and other simulations. Moreover, the required small particle resolution and the domain size were properly selected based on an extensive numerical study. The diameter of the carrier particles was 100 μm, while the fine particles had diameters of 3 μm and 5 μm. The range of particle Reynolds numbers considered was between 0.5 and 200. The coverage degree of the carrier by the small particles was varied between 10% and 50% in the simulations, and its influence on the detachment was determined. A shear flow with shear rate 100,962 s^{-1} was simulated. From these simulations the fluid dynamic forces on the drug particles were extracted in dependence of the angular position in order to estimate the possibility of drug particle detachment. Detachment might occur through lift-off, sliding or rolling. Lift-off detachment was found to be not possible due to the acting small normal forces even at Re = 200. The probability of sliding and rolling detachment in dependence of the angular position was estimated based on measured adhesion properties, i.e. van der Waals force, adhesion surface energy and friction coefficient.

Turbulence was generated by a digital filtering technique applied to the inflow velocity boundary. Prior to these studies, this technique is validated by comparing the turbulence intensity at 15 fluid nodes along the stream-wised direction of the computational domain. The particle Reynolds number considered was 200 and the turbulence intensity was varied from 0.3% to 9.0%. These simulations provided the temporal evolution of the fluid dynamic forces on the drug particles in order to estimate the possibility of drug particle detachment. For turbulent conditions (i.e. Re = 200 and I = 9.0%) the fluid force on the drug particles was found to be about 10-times larger than found in laminar flow. Lift-off was found to be of minor importance due to the observed small normal fluid forces even at Re = 200 and I = 9.0%. The remarkable rise of detachment probability for both effects due to the action of turbulence is an important finding of this study.

In order to simulate roughness, only one smooth drug particle was placed on a rough carrier surface. The roughness was simplified by a row of semi-cylinders in the stream-wised direction of the flow on the wall, and was varied by the asperity distance between the rough elements and the size ratio between the semi-cylinder and the drug particle. First the required particle resolution and domain size were properly selected based on an extensive numerical study and parameter study was carried to understand the relationship between the contact distance, the asperity distance, the size ratio and the particle height. The influence of roughness on the velocity profile was studied and the numerical determined hydrodynamic torque around particle mass centre was investigated for a wide range of particle Reynolds number and wall structures. Lift-off was found to be not possible due to the acting small normal forces. The rolling and sliding ratio of the drug particle was estimated by varying the particle Reynolds number, asperity distance and roughness element size.

A new and efficient numerical particle-wall interaction model for simulating the instantaneous forces and velocities on particles during wall collision process is described in chapter 4. During the collision the carrier particle can slides and rolls on the wall. The translational and rotational velocities of the carrier were solved instantaneously during the compression and recovery phases, and the maximum inertia force experienced by the drug particle was determined by initial impact conditions and material properties. The simulation results reveal that the inertia force on the drug particle is much larger than the fluid dynamic force. Nearly half of the drug particles can be detached by lift-off, the remaining particles follow up with a sliding or rolling detachment.

The present studies improve the understanding of drug particle detachment from carrier particles in an inhaler device. The results will be the basis for developing Lagrangian detachment models that eventually should allow the optimisation of dry powder inhalators through computational fluid dynamics.

Contents

Preface I

Abstract III

Contents VII

1 Introduction 1

1.1 Dry Powder Inhaler 1

1.2 Flow over Wall Bounded Particles 4

1.3 Macro Scale Simulation 6

1.4 Structure of the Thesis 9

2 Micro Scale Simulation 11

2.1 Numerical Method 11

2.1.1 Lattice Boltzmann method 12

2.1.2 Boundary condition 14

2.1.3 Local grid refinement 16

2.1.4 Particle near contact 19

2.2 Validation of a Particle attached to the Wall 22

2.3 Setup of Simulation for Particle Clusters 31

2.3.1 Computational domain and resolution 31

2.3.2 Parameter definition 35

2.4 Forces on Drug Particles in Laminar Flow 37

2.4.1 Particle Reynolds number 43

2.4.2 Coverage degree 48

2.4.3 Size ratio 50

2.4.4 Shear rate 51

2.5 Validation of Turbulence Generation 53

2.5.1 Decaying grid turbulence 53

2.5.2 Homogeneous isotropic turbulence 55

2.5.3 Digital filter based turbulence inflow data generation 58

2.5.3.1 Numerical algorithm 59

2.5.3.2 Simulation setup 60

2.5.3.3 Forces on drug particles in turbulent flow 61

3 Flow Detachment Model 67
3.1 Plane Wall Detachment Model 68
3.1.1 Detachment criterion 68
3.1.2 Experimental measurement 71
3.1.3 Lift-off detachment 72
3.1.4 Sliding detachment 73
3.1.5 Rolling detachment 76
3.1.6 Comparison of the sliding and rolling detachment 82
3.1.7 Sliding and rolling detachment in turbulent flow 85
3.2 Rough Wall Detachment Model 89
3.2.1 Introduction 89
3.2.2 Detachment criterion 90
3.2.3 Simulation setup 92
3.2.4 Results analysis 97
4 Wall Collision Detachment Model 109
4.1 Theory formulation 111
4.1.1 Force on particles 111
4.1.2 Case I 114
4.1.3 Case II 119
4.1.4 Case III 120
4.1.5 Detachment criterion 120
4.2 Results analysis 121
4.2.1 Parameter study 122
4.2.2 Detachment study 127
5 Summary and Outlook 133
Nomenclature 139
List of Figures 143
List of Tables 161
Bibliography 163
Curriculum Vitae 171
Erklärung 173

1 Introduction

1.1 Dry Powder Inhaler

Due to the lack of propellants, high patient compliance and high dose carrying capacity pulmonary drug delivery by dry powder inhalers (DPIs) is increasingly being used in the therapy of asthma and other chronicle pulmonary diseases. Therefore, numerous designs of inhalers are on the market (Smith & Parry-Billings, 2003; Islam & Gladki, 2008). Particles that can be administered via dry powder inhalers have to exhibit aerodynamic diameters in the size range of 1 µm to 5 µm as only particles of this size can reach the tiny airways of the deep lung. Particles of such small size are very cohesive and show poor flow properties which leads to difficulties concerning volumetric dosing. To overcome this problem the fine drug powder is mostly blended with larger carrier particles (in the size range of 50 µm to 500 µm). During blending the small active pharmaceutical ingredient (API) particles will stick to the surface of the larger carrier particles so that they will be partially covered. Such large particles exhibit adequate flow ability and can be easily handled.

For achieving high drug delivery efficiency during inhalation, the fine drug particles need to be detached from the carrier within the inhaler device through the stresses in the air flow or collisions with device walls. As a result, the dispersed fine drug particles can be easily transported deep into the lung while the carrier particles remain in the inhaler or are deposited in the upper airways and thereafter naturally cleared. The fluid dynamic detachment of the drug powder in the complex airflow of an inhaler is realised by acceleration/deceleration of the carrier particles (i.e. inertial force), flow shear gradients and turbulent stresses (Telko & Hickey, 2005). In order to deliver a high amount of detached drug particles a proper balancing between the adhesive forces between carrier and drug and the removal forces during the inhalation process is necessary. Thus inter-particle interactions (i.e. adhesion force) between API and carrier play a key role in this kind of formulations. On the one hand they have to be high enough that the API sticks to the carrier surface thus ensuring proper handling as well as uniform dosing and on the other hand low enough that drug detachment from the carrier surface during inhalation is guaranteed. One approach to tailor inter-particle-interactions between drug and carrier is the surface modification of the carrier particles (Zellnitz, et al., 2011). Besides the balancing of inter-particle interactions the inhaler design needs to ensure sufficiently high flow stresses on the carrier particles for yielding high detachment rates. So the detachment of drug particles from the carrier is a prerequisite for a high respirable fraction in vivo that is equivalent to a high fine particle fraction (FPF) in vitro. The FPF is determined by a standardised procedure using cascade impactors and represents the ratio of the fine particle dose (FPD) and the mass of API leaving the inhaler (emitted dose (ED)) in %. The FPD is the mass of drug particles below 5 µm. The FPF is a common parameter to compare the performance of different inhaler types and different formulations among each other.

The impactors used and the procedure of determining of the FPF are described in the monograph “Aerodynamic assessment of fine particles for preparations for inhalation” of the European Pharmacopoeia. Impactor data are an important and principal part of marketing authorization applications for new dry powder inhaler formulations. Consequently, so far the design and optimisation of inhalers is mainly based on experimental analysis. Essential for the performance of an inhaler is a high amount of drug powder (i.e. fine particle fraction) that is able to leave the inhaler and reach the deep lung. As already has been mentioned the determination of the FPF is mainly done using different types of cascade impactors (Steckel & Müller, 1997; de Koning, 2011). Numerous such experimental studies have been conducted for analysing the influence of inhaler devises on the FPF (Srichana, et al., 1998; Telko & Hickey, 2005; Chew, et al., 2002; Newman & Busse, 2002). However, these experimental approaches are rather cumbersome and time-consuming. Therefore, it would be advantageous developing a drug detachment model which could be used in connection with the application of computational fluid dynamics (CFD) for analysing inhaler performance and overcome the time consuming impactor experiments.

In the past CFD has been already applied by a number of research groups for studying the performance of inhalers. These studies are related to an analysis of flow structure and particle motion inside an inhaler mostly. Objectives were for example the study of the particle motion in different inhaler designs (Donovan, et al., 2012), the influence of a grid inserted into the outflow tube (Coates, et al., 2004) or the effect of mouthpiece shape (Coates, et al., 2007). In all of these numerical calculations only the motion of the carrier particles was tracked for visualisation purposes (see Donovan et al. 2012). Describing the detachment of drug particles from the carrier would require additional modelling and was not considered in numerical studies performed so far.

The aim of the present contribution is the development of Lagrangian detachment models which eventually should allow the numerical prediction of inhaler performance and efficiency. For this purpose a multi-scale analysis is adopted here (Fig. 1.1). First the flow field through the entire inhaler device (here the Cyclohaler®) is calculated numerically using OpenFOAM® and the fluid dynamic stresses acting on the carrier particles are recorded and statistically analysed (Cui, et al., 2013; Cui, et al., 2014; Sommerfeld & Schmalfuß, 2015). With these flow conditions micro-scale numerical simulations based on the LBM are conducted for a fixed carrier particle covered with hundreds of drug particles placed into a prescribed flow (Cui & Sommerfeld, 2012; Cui & Sommerfeld, 2015). From the simulated fluid forces acting on the drug particles the possibility of detachment is determined based on measured van der Waals forces and friction coefficients as well as other contact properties (Cui, et al., 2014; Zellnitz, et al., 2013). Moreover, the inertia force experienced by the drugs during the particle-wall collision may yields a potential detachment and is well calculated.

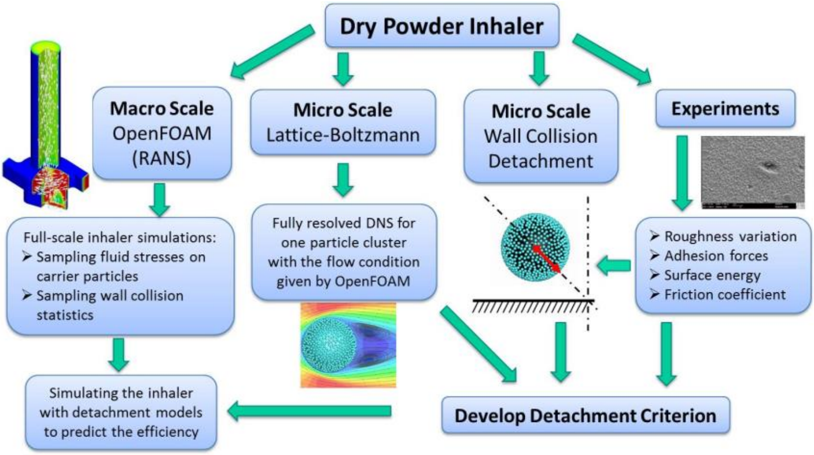
Dry Powder Inhaler
Macro Scale OpenFOAM (RANS)
Micro Scale Lattice-Boltzmann
Micro Scale Wall Collision Detachment
Experiments
Full-scale inhaler simulations:
➤ Sampling fluid stresses on carrier particles
➤ Sampling wall collision statistics
Fully resolved DNS for one particle cluster with the flow condition given by OpenFOAM
➤ Roughness variation
➤ Adhesion forces
➤ Surface energy
➤ Friction coefficient
Simulating the inhaler with detachment models to predict the efficiency
Develop Detachment Criterion

Fig. 1.1 Summary of multi-scale approach for inhaler optimisation and design.

The results from the micro scale simulations (i.e. forces on drug particles) and the experiments (interaction parameters between carrier particles and drug particles) will be used to develop a drug detachment model for Lagrangian calculation of the entire device using OpenFOAM® (macro-scale simulations). Moreover, the calculations need to be validated based on measured fine particle fraction leaving the inhaler by using cascade impactors (Fig. 1.1). The present project is cooperated with S. Schmalfuß (my colleague), S. Zellnitz and N. Urbanetz from Technische Universität Graz, N. Renner and R. Scherließ from Christian-Albrechts-Universität zu Kiel.

1.2 Flow over Wall Bounded Particles

The fluid dynamic forces acting on a spherical particle sitting on a plane or rough wall under linear shear or turbulent flow were already examined for many years, mainly theoretically and experimentally (Saffman, 1965; O`Neill, 1968; Hubbe, 1984; Leighton & Acrivos, 1985; Biasi, et al., 1988; Reeks & Hall, 2001; Sweeney and Finlay, 2007; Zeng, et al., 2009; Larsen et al., 2010; Derksen & Larsen, 2011; Zhang, et al., 2013; Zhang, et al., 2013). Since several years also fully resolved direct numerical simulations (DNS) are being used for determining lift and drag forces acting on single particles attached to a wall (Biasi, et al., 1988; Reeks & Hall, 2001; Sweeney and Finlay, 2007; Zeng et al., 2009; Larsen et al., 2010). In these studies laminar shear or boundary layer flows are considered mostly. From their simulations Sweeney and Finlay (2007) proposed complex fitting curves for the drag (C_D) and lift (C_L) coefficients in dependence of the particle Reynolds number (determined with the centre velocity impinging the sphere). In the work of Zeng et al. (2009) also the situation of a sphere touching the wall was considered and they presented the non-dimensional lift force as a function of the particle Reynolds number determined with the particle radius and the friction velocity. Their own simulations as well as a proposed correlation were compared with several analytical results and also experiments for Reynolds numbers between 1 and 10. More recently Derksen and Larsen (2011) calculated the fluid dynamic forces on random assemblies of particles attached to a plane wall using the LBM combined with an immersed boundary method. These studies were performed for a plane shear flow at low Reynolds numbers. One important finding of this study is the drastic reduction of the drag and lift force with increasing occupancy of the wall with particles. The reason for that is the tendency of the flow to pass over all the particles at high surface occupancy. The values for the lift actually become close to zero for coverage degrees of more than 40%. Later in Section 2.2 the reliability of calculating fluid dynamic forces acting on spherical particles attached to a plane wall under linear shear flow by the present LBM code is demonstrated by comparing to the above experimental and simulation results.

Early theoretical study of particle adhesion and removal was provided by O’Neill (1968). Later the JKR adhesion model was developed by Johnson, Kendall and Roberts (1971), which discussed the influence of surface energy on the contact between elastic solids. Hubbe (1984) gave a theoretical overview on the detachment of colloidal particles from solid surfaces under shear flow. More importantly, Hubbe concluded that the component of hydrodynamic force acting parallel to a sheared wall was usually much larger than the lifting force, and the hydrodynamic force acting over the surface of the particle could be replaced by an effective force acting at a higher position. Later voluminous literature emerged studying the force and moment balance detachment models for individual microspheres on a surface embedded in a viscous sub-layer (e.g. Reeks et al., 1988; Wen and Kasper, 1989; Soltani and Ahmadi, 1994; Phares et al., 2000; Ibrahim et al., 2008; Zhang, et al., 2013; Zhang, et al., 2013). The above-described models for particle resuspension or detachment from plane surfaces may be applicable to the present study, since the carrier particles are much larger than the very fine drug particles. However, they are based on the combined effect of convective flow and turbulence. In the present study, it is aimed at analysing the effect of laminar and turbulent flow separately.

1.3 Macro Scale Simulation

For the numerical calculations of stationary flow through an inhaler the open source code OpenFOAM® is applied, herewith the Reynolds-averaged conservation equations (RANS) in connection with the k-ω-SST turbulence model are solved. The considered inhaler (i.e. the Cyclohaler®) is discretised by a tetrahedral mesh consisting of about 400,000 cells (Fig. 1.2). The flow condition considered here corresponds to 100 L/min which is a typical inspiratory maximum flow rate (Newman & Busse, 2002). In order to obtain an appropriate outflow velocity profile, first a pipe flow (diameter identical to the mouthpiece of the inhaler) was calculated with the present flow rate (i.e. 100 L/min, bulk flow velocity 19.2 m/s). The developed velocity profile and the associated turbulence properties were then used as outlet condition for the inhaler calculation. At the two tangential inlets only the ambient total pressure needs to be prescribed. At the walls standard wall functions were applied. A carrier particle covered with hundreds of drug particles is considered as a point particle and was tracked in the calculated stationary flow field by neglecting their influence on fluid flow and turbulence (i.e. one-way coupling). For each simulation run 1024 point particles were considered initially being regularly distributed in the capsule reservoir. At the beginning of the Lagrangian calculation the particles were released and moved by the fluid dynamic forces through the stationary flow field. The forces considered in particle tracking are drag force, added mass force, slip-shear/slip-rotation lift and gravity.

The velocity and turbulent kinetic energy fields resulting from the flow calculations are shown in Fig. 1.3a & 1.3b for a flow rate of 100 L/min. The highest magnitudes of mean velocities are found in the swirl chamber and near the grid inserted at the entrance to the mouthpiece. The flow in an inhaler is very complex, especially, in the swirl chamber below the grid extremely high velocities are reached (Fig. 1.3a), which also give rise to very high turbulent kinetic energies (Fig. 1.3b). Typical particle trajectories within the inhaler for the three mono-sized particles are shown in Fig. 1.3c. The particles are basically bouncing from wall to wall (i.e. wall-collision dominated behavior) retaining however a swirling motion throughout the mouthpiece. This part of work is done by Sommerfeld and Schmalfuß, more details can be found in Sommerfeld & Schmalfuß (2015).

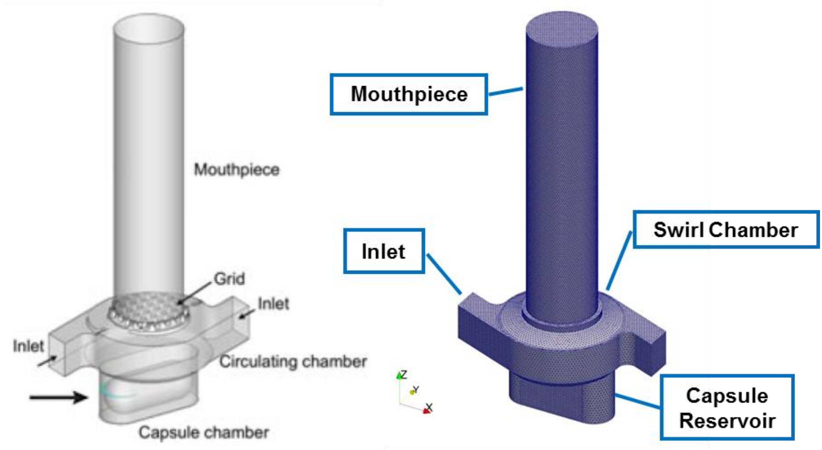
Mouthpiece
Grid
Inlet
Inlet
Circulating chamber
Capsule chamber
Mouthpiece
Inlet
Swirl Chamber
Capsule Reservoir
Z
Y
X

Fig. 1.2 Geometry of a typical swirl-flow inhaler device (left, taken from Donovan et al. 2012) and numerical grid used for the inhaler discretization (right, Sommerfeld & Schmalfuß, 2015).

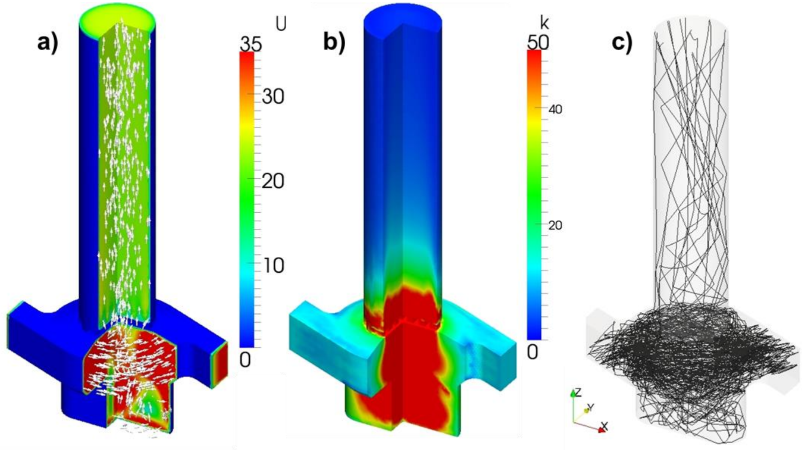
a)
U
35
30
20
10
0
b)
k
50
40
20
0
c)
Z
Y
X

Fig. 1.3 Calculated flow field of the inhaler; a) total velocity modulus and velocity vectors near the inhaler wall; b) turbulent kinetic energy energy (colour scale: m^2/s^2); c) representative particle trajectories for mono-sized particles through the inhaler; (100 L/min) (Sommerfeld & Schmalfuß, 2015).

1.4 Structure of the Thesis

The present thesis is organized as following. In Chapter 2, first the principles of the LBM are shortly introduced including the methods employed for enhancing the spatial resolution of the LBM, namely curved wall boundary condition and local grid refinement. Special emphasis is put on the calculation of the fluid dynamic forces separately for two particles which are in close contact. Then the present simulations are validated by comparing simulated lift and drag for a particle in contact with a plane wall with analytic, experimental as well as numerical results. For the special case of a larger carrier covered with hundreds of micron-sized drug particles studies on the required domain size and the necessary resolution of the fine particles are introduced. Then the calculated fluid dynamic forces acting on the drug particles are analysed and discussed in detail for a range of relevant properties of the particle cluster and the flow. Finally, different turbulence generation methods are discussed and then properly selected. The turbulence simulations conducted for different turbulence intensities and the corresponding fluid dynamic forces on the drug particles are evaluated and compared with the results in the laminar flow.

In Chapter 3, two flow detachment models were introduced, namely plane wall detachment model, rough wall detachment model. First the possibility of drug particle detachment from a smooth surface is evaluated on the basis of experimental information of particle-particle interaction mechanisms and the fluid dynamic forces from the macro-scale simulation. After that, the wall is roughened and the influences of the rough wall on the particle detachment are studied by varying the size and the asperity distance of the rough elements.

The particle-wall collision detachment model was introduced in Chapter 4. At first the model is established on account of instantaneous translational and rotational velocities, resistance force, friction force and inertia force of particles, together with the detachment criterion for the lift-off, sliding and rolling detachment of drug particles. Then the influence of several parameters, i.e. impact angle and friction coefficient on the velocities and forces of the carrier particle are studied, and the forces on drug particles are depicted in dependence on their angular location on the carrier surface. After that the detachment of drug particles for a single collision process is evaluated and compared to the flow detachment study.

2 Micro Scale Simulation

Numerical calculations were performed in this chapter for a particle cluster consisting of a large carrier particle covered with many small spherical drug particles. Due to the complexity of the particle cluster structure, the LBM which is mainly implemented by M. Dietzel and M. Ernst is adopted and further developed for the particle simulation. Prior to these studies, the LBM is validated based on a test case where a single particle is situated on a wall and exposed to a linear shear flow, and the present simulation results are compared with analytical results and other simulations. With regard to the particle cluster the required small particle resolution and the domain size are properly selected based on an extensive numerical study. In simulation the diameter of the carrier particles keeps constant, while the diameter of the fine particles varies. The particle Reynolds numbers are considered in a wide range, as well as the coverage degree of the carrier by the small particles. Different turbulence generation methods are implemented into the LBM codes and are then evaluated. From these simulations the fluid dynamic forces on the drug particles are extracted in dependence of the angular position in order to estimate the possibility of drug particle detachment.

2.1 Numerical Method

The computation of the fluid flow is performed using a three-dimensional LBM. Basically, the LBM (Benzi, et al., 1992; Guo & Shu, 2013; Dietzel & Sommerfeld, 2013; Ernst, et al., 2013) is a class of CFD method for fluid simulation which originated from molecular dynamics models such as Lattice Gas Automata. Instead of solving conservation equations for macroscopic properties as done by using the Navier-Stokes equations, the discrete Boltzmann equation is solved, describing the fluid behaviour on a mesoscopic scale. Fictive fluid elements represented by a probability distribution function move along a lattice grid and collide at the lattice nodes. Besides the spatial discretization realized by the numerical grid, time and velocities are discretized as well. Information is allowed to propagate to a neighbouring lattice node in one of the discrete lattice directions at one time step only, followed by a collision step. The discrete Boltzmann equation is solved with the help of a collision model such as the single relaxation time approach of Bhatnagar–Gross–Krook, abbreviated as BGK (Bhatnagar, et al., 1954). Compared to other grid based CFD approaches, LBM has the advantage of being capable to easily deal with arbitrary and complex shaped wall boundaries and objects embedded in the flow. Thereby, forces acting on walls or obstacles inside the flow domain can be directly calculated from the change of state of the distribution function along the obstacle surface.

In the following a brief outline of the applied LBM is given. More detailed method description as well as examples of validation cases of the applied LBM can be found in Hölzer & Sommerfeld (2009), Dietzel & Sommerfeld (2009), Ernst & Sommerfeld (2012), Dietzel & Sommerfeld (2013), Ernst, et al. (2013) and Cui & Sommerfeld (2015).

2.1.1 Lattice Boltzmann method

The discretized lattice Boltzmann equation combined with a single relaxation time collision operator approximated by the BGK approach is given below:

$$f_{\sigma i}\left(\mathbf{x}+\boldsymbol{\xi}_{\boldsymbol{\sigma}\mathbf{i}}\Delta t, t+\Delta t\right)-f_{\sigma i}\left(\mathbf{x},t\right)=-\frac{\Delta t}{\tau}\left(f_{\sigma i}\left(\mathbf{x},t\right)-f_{\sigma i}{}^{(0)}\left(\mathbf{x},t\right)\right)+\Delta t\,F_{ext,i} \qquad 2.1$$

where $\Delta x = \xi_{\sigma i}\,\Delta t$ is the width of the spatial discretization, Δt the duration of one time step, τ the relaxation time and $f_{\sigma i}{}^{(0)}$ is the discrete equilibrium distribution function. The forcing term $F_{ext,i}$ is used to introduce an external vector-valued force **F** into the lattice Boltzmann equation.

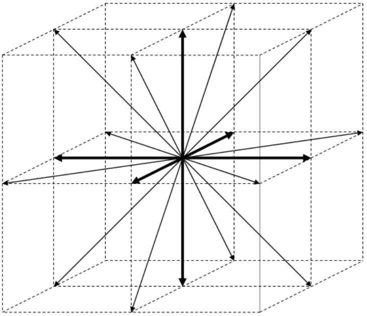

Fig. 2.1 Directions of discrete equilibrium distribution function of the D3Q19 model.

In this work the D3Q19 model which applies to a three dimensional grid and provides 19 propagation directions is used as shown in Fig. 2.1. These directions can be distinguished in six vertical and horizontal velocity vectors (σ = 1), twelve diagonal velocity vectors (σ = 2) and one direction for zero velocity (σ = 0). During the propagation step, information is transported along these lattice directions, left side of Eq. 2.1, followed by the collision step, right side of Eq. 2.1. The discrete equilibrium distribution function (EDF) is given by:

$$f_{\sigma i}^{(0)}\left(\mathbf{x},t\right)=\omega_{\sigma i}\rho\left(1+\frac{3\boldsymbol{\xi}_{\boldsymbol{\sigma}\mathbf{i}}\mathbf{u}}{c^2}+\frac{9\left(\boldsymbol{\xi}_{\boldsymbol{\sigma}\mathbf{i}}\mathbf{u}\right)^2}{2c^4}-\frac{3\mathbf{u}^2}{2c^2}\right) \tag{2.2}$$

$$c=\frac{\Delta x}{\Delta t}=\sqrt{3}\,c_s\,,\ \ \omega_{\sigma i}=\begin{cases}1/3\,; & \sigma=0, i=1\\ 1/18\,; & \sigma=1, i=1\ldots 6\\ 1/36\,; & \sigma=2, i=1\ldots 12\end{cases} \tag{2.3}$$

$\omega_{\sigma i}$ are the weighting factors for the D3Q19 model, **u** is the velocity vector and c is the grid constant which can be defined as a ratio of spatial and temporal discretization which is related to the speed of sound c_s. Fluid density and momentum can be obtained from moments of the discrete distribution functions in the following way:

$$\begin{aligned} \rho(\mathbf{x},t) &= \sum_{\sigma}\sum_{i} f_{\sigma i}(\mathbf{x},t) \\ \rho(\mathbf{x},t)\,\mathbf{u}(\mathbf{x},t) &= \sum_{\sigma}\sum_{i} \boldsymbol{\xi}_{\boldsymbol{\sigma}\mathbf{i}}\ f_{\sigma i}(\mathbf{x},t) \end{aligned} \qquad 2.4$$

The local pressure can be derived from the local density and the speed of sound:

$$p(\mathbf{x},t) = c_s^2 \rho(\mathbf{x},t) = \frac{1}{3}\frac{\Delta x^2}{\Delta t^2}\rho(\mathbf{x},t) \qquad 2.5$$

The relationship between the dynamic viscosity of the lattice Boltzmann scheme and the relaxation parameter can be described in the following way:

$$\eta = \frac{1}{6}\rho c^2 (2\tau - \Delta t) \qquad 2.6$$

The numerical stability of the LBM is influenced by several criteria such as the upper limit of the Mach number (normally: $Ma = u / c_s < 0.2$) and the lower bound of the relaxation time parameter ($\tau / \Delta t > 0.5$) which limits the maximum Reynolds number that can be realized depending on the resolution of the numerical grid (Dietzel & Sommerfeld, 2013).

2.1.2 Boundary condition

In the LBM the forces and moments on any object (e.g. fine particles) are obtained through the change of the distribution function when being reflected at a solid surface, i.e. bounce-back boundary condition. For improving the spatial resolution the exact location of any curved boundary is accounted for in the bounce-back scheme (Bouzidi, et al., 2001; Guo, et al., 2002; Dietzel & Sommerfeld, 2013). This approach allows much more accurate force calculations compared to the standard stepwise representation of boundaries.

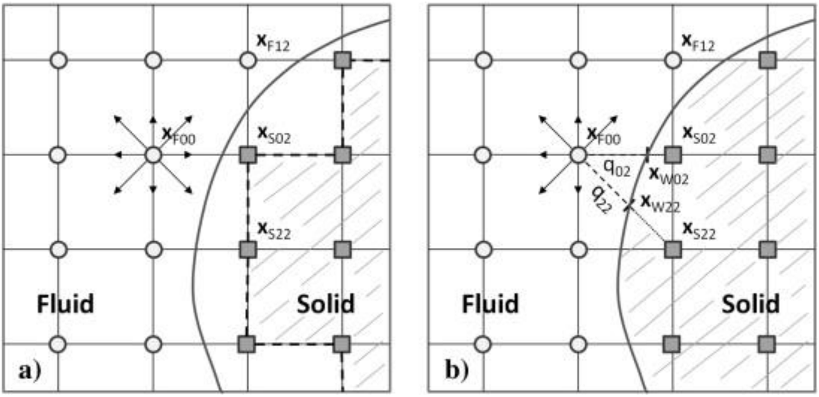

Fig. 2.2 Treatment of the wall boundary condition on the particle surface applying the bounce-back approach: (a) stepwise representation of the particle surface inscribing the given geometry; (b) curved-wall boundary condition using the exact wall distance q between fluid node (x_{F00}) and obstacle surface (x_W) (Dietzel & Sommerfeld, 2013).

A standard stepwise approach of a curved solid surface is illustrated in Fig. 2.2a. The full distance between the fluid node at position $\mathbf{x}_{F00}$ and the neighbouring solid nodes ($\mathbf{x}_S$) is considered for the application of the bounce-back scheme, regardless of the exact location of the solid boundary. This standard wall boundary condition needs a large number of grid nodes for resolving the particle contour properly for randomly generated particles. In order to relax this requirement, the curved no-slip boundary condition Wang, et al. (1998) and Chen & Doolen (1998) is imposed on the particle surface. This boundary model is an extension of the bounce-back procedure and uses an extrapolation scheme which evaluates the proper distance between the wall position $\mathbf{x}_W$ and the adjacent fluid node at location $\mathbf{x}_{F00}$ (Fig. 2.2b). The corresponding interception parameter *q* is considered for each relevant propagation direction of the adapted bounce-back scheme. This method ensures that the particle shape is accurately reproduced and that forces on the particles are determined correctly regardless of the particle location within the grid (which would be very important for movable particles). Moreover, less computational grids are required to discretize the particle using the curved no-slip boundary condition.

Another advantage of the LBM is that forces acting on objects are not determined by integrating the pressure and shear stress distribution around them. Instead, the momentum exchange between the fluid and the particle is obtained based on the bounce-back approach. Therefore, the difference of fluid momentum before and after contact with the obstacle wall yields the local force $\mathbf{F}_{\boldsymbol{\sigma}\mathbf{i}}$:

$$\mathbf{F}_{\boldsymbol{\sigma}\mathbf{i}}\left(\mathbf{x},t+\Delta t/2\right)=\frac{\Delta V}{\Delta t}\left(f_{\sigma i}\left(\mathbf{x},t+\Delta t\right)-f_{\sigma i}\left(\mathbf{x},t^{*}\right)\right)\boldsymbol{\xi}_{\boldsymbol{\sigma}\mathbf{i}} \tag{2.7}$$

t^{*} is the time after collision step. The local torque follows from local forces and their distance to the centre of rotation:

$$\mathbf{T}_{\boldsymbol{\sigma}\mathbf{i}}\left(\mathbf{x},t+\Delta t/2\right)=\left(\mathbf{x}-\mathbf{x}_{\mathbf{R}}\right)\times\mathbf{F}_{\boldsymbol{\sigma}\mathbf{i}}\left(\mathbf{x},t+\Delta t/2\right) \tag{2.8}$$

Summarizing all local forces and torques along the obstacle surface leads to the total force or torque, respectively (Hölzer & Sommerfeld, 2009; Dietzel & Sommerfeld, 2013):

$$\begin{aligned}\mathbf{F}\left(t+\Delta t/2\right)&=\sum_{\mathbf{x}}\sum_{\sigma i}\mathbf{F}_{\boldsymbol{\sigma}\mathbf{i}}\left(\mathbf{x},t+\Delta t/2\right)\\ \mathbf{T}\left(t+\Delta t/2\right)&=\sum_{\mathbf{x}}\sum_{\sigma i}\mathbf{T}_{\boldsymbol{\sigma}\mathbf{i}}\left(\mathbf{x},t+\Delta t/2\right)\end{aligned} \tag{2.9}$$

2.1.3 Local grid refinement

Generally, LBM is a direct numerical simulation (DNS) method. In order to simulate the flow around agglomerates, the computational power needed leads to a tremendous numerical effort because of the wide range of scales involved in fluid dynamics. However, the smallest scales are often localized in a relatively limited computational area. Therefore, the local grid refinement method was introduced to reduce the computational costs by enabling different discretization levels with the computational domain.

Region of small scale or small gradients of flow variables are discretized by fine grid cells whereas the large scales need to be discretized by larger grid cells. For example, as shown in Fig. 2.3, the region close to the particle cluster is applied with fine mesh whereas a coarser mesh is applied far from the cluster.

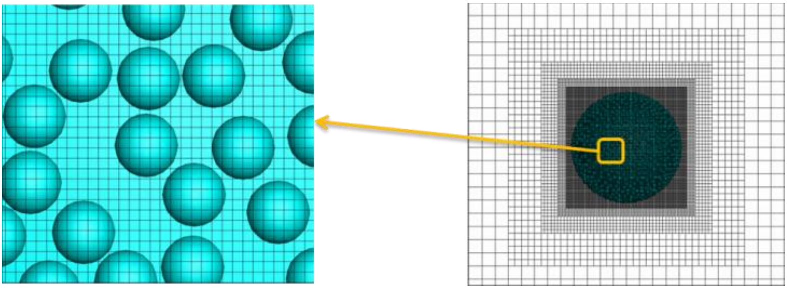

Fig. 2.3 Local grid refinement of a carrier particle covered by many small particles.

Grid refinement technique was initially introduced into lattice Boltzmann equation (LBE) by Filippova and Hänel (FH) (1998). In their approach a coarse mesh is first used to cover the flow field, and then one or more patches with refined resolutions will be inserted into some region on the coarse mesh where the flow may change significantly (Guo & Shu, 2013). Recently, many of the development and progress have been published in both the refinement strategy and the underlying data structure. In this thesis, we use the node-based approach which was initially introduced by Crouse (2003), and was further developed by M. Dietzel (Dietzel & Sommerfeld, 2013). In their method, a sensor variable, which is based on heuristic expressions for primary or derived quantities of the flow field, is used to detect the location of new refinement zones. The adaptive refinement begins with an initial grid. After a preliminary solution is achieved, the sensor is evaluated in every cell surrounded by some neighbouring nodes. If the value of the sensor in a cell exceeds a critical value, the cell will be marked for refinement. The unknown distribution functions on the new refined grid nodes can be constructed from the parent cells using certain interpolation schemes as used in the FH method, and simulation process continues then on the improved grid (Guo & Shu, 2013).

Fig. 2.4 shows two adjacent regions with different grid resolution. The fine region appears by dividing each former coarse cell into eight fine cells in 3D, so that the edge length of the fine cells corresponds to half of size of the coarse cells. A grid refinement convention in this work is that adjacent grid cells can only be identical or half of the grid length. This limitation is basically introduced to improve the stability of the numerical scheme. Since both the viscosity and propagation velocity (and the corresponding lattice constant) must be a constant across the whole fluid domain, the time step and relaxation parameter have to be adjusted depending on the refinement level. Local grid width and local time step follow from the actual grid level (*gl*) (Dietzel & Sommerfeld, 2013):

$$\Delta x_{gl} = \frac{1}{2^{gl}} \Delta x_0 , \Delta t_{gl} = \frac{1}{2^{gl}} \Delta t_0 \qquad 2.10$$

The coarsest grid level corresponds to $gl = 0$ and the finest level is depending on the considered problem. Because of the time step is reduced in the fine grid regions, the information needs to be propagated more often compared to the coarse grid, to ensure a constant propagation velocity. A sequence control manages the cycles of propagation and relaxation for each grid level so that the entire grid is at the same time level at the end of a global iteration (Crouse, 2003). Alternatively to the constant ratio of spatial and time discretization for all refinement levels, other approaches such as a constant relaxation time or a constant time step are available (Alemani, et al., 2007).

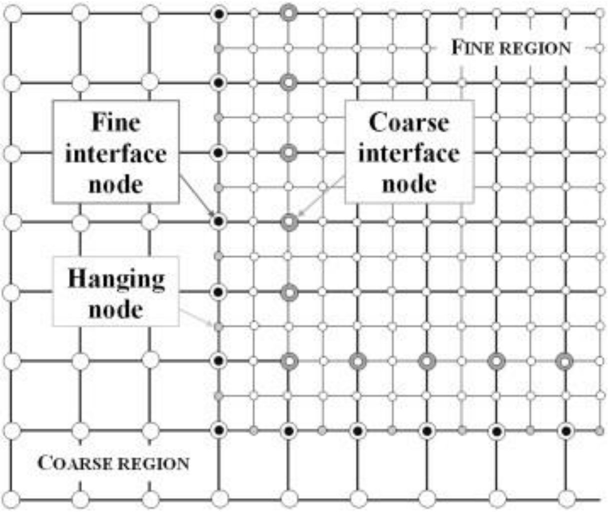

Fig. 2.4 Definition of node types at the interface between coarse and fine grid sections (Dietzel & Sommerfeld, 2013).

2.1.4 Particle near contact

In the present simulations the forces on hundreds of fine drug particles adhered to a carrier particle shall be determined. However, when two particles are in near contact, i.e. less than one lattice spacing, there exists a problem to calculate the forces on these particles separately.

Normally, the nodes inside the particle are declared as solid nodes and outside of the particle are fluid nodes. The forces over a particle are obtained from a momentum balance at the solid surface (reflection of the fluid elements at the particle boundary). When particles are in close contact (separation less than one lattice), there is a lack of fluid nodes between the particles as shown in Fig. 2.5, and consequently some solid nodes are included to calculate the particle force. However, those solid nodes have no fluid information and therefore the force calculation will be wrong. One way to avoid this problem is to introduce some fluid property to the solid nodes within that particle (stars in Fig. 2.5) wherefore the fluid dynamic forces shall be calculated. For that purpose, the EDF is assigned to these solid nodes and the velocity is set to be identical to the particle surface velocity, i.e. no slip condition at the particle surface (Ernst, et al., 2013). With the application of this method, it is possible to separately calculate the forces on particles in close contact or a particle in contact with a wall.

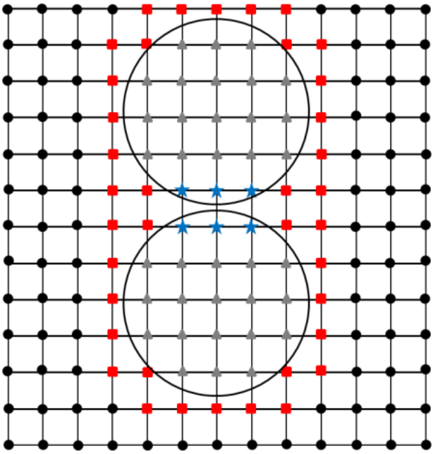

Fig. 2.5 Nodes around two particles near contact: the cycles indicate the fluid nodes far away the particle; the squares indicate the adjacent fluid nodes near the particle surface; the triangles indicate the solid nodes inside the particle; the stars indicate the solid-fluid nodes near its neighbouring particle.

Additionally, Ladd (1994) and Pietro, et al. (2006) found that for approaching particles, the LBM breaks down at very small distances between two particles due to the lack of spatial resolution in the gap between the particles. He solved this problem by introducing an extra lubrication force which accounts for the contribution to the hydrodynamic forces due to the unresolved part of the flow field. The lubrication force (acting along the centreline of two particles *i* and *j*) is given by:

$$\boldsymbol{F}_{lub} = -\frac{3\pi\mu a}{s}\,\hat{\boldsymbol{x}}_{\boldsymbol{ij}}\;\hat{\boldsymbol{x}}_{\boldsymbol{ij}}\cdot\left(\boldsymbol{u}_i - \boldsymbol{u}_j\right) \qquad 2.11$$

where $s = R / a - 2$ is the dimensionless gap width (R is the distance between the centres of the particles) and $\boldsymbol{x}_{ij} = \boldsymbol{x}_i - \boldsymbol{x}_j \cdot \boldsymbol{x}_i$ and $\boldsymbol{x}_j$ are the coordinates of the particles and $\hat{\boldsymbol{x}}_{ij} = \boldsymbol{x}_{ij} / \left| \boldsymbol{x}_{ij} \right|$; $\boldsymbol{u}_i$ and $\boldsymbol{u}_j$ are the particle velocities. This method is generalized by casting the interaction between particles in the grand-resistance-matrix formulation (Nguyen & Ladd, 2002) using friction coefficients given by Kim & Karilla (1991). This method also accounts for tangential friction and allows the accurate calculation of the particle stresslet (Cyrus & Jonathan, 2010). As the near field hydrodynamic force plays a critical role in our simulation, we used an improved version for the lubrication force given by Kim & Karilla (1991), in which a logarithmic correction is included:

$$\boldsymbol{F}_{lub} = -\left(\frac{3\pi\mu a}{s} + \frac{27\pi\mu a}{20} log \frac{1}{s} \right) \hat{\boldsymbol{x}}_{\boldsymbol{ij}} \; \hat{\boldsymbol{x}}_{\boldsymbol{ij}} \cdot \left(\boldsymbol{u}_i - \boldsymbol{u}_j \right) \qquad 2.12$$

In conclusion, for stationary particles, the EDF is assigned to those solid nodes which are adjacent to another particle’s surface. Hence the solid nodes are converted into the solid-fluid nodes (solid nodes with fluid information). For the particles which have relative motion, lubrication force should be taken into consideration.

2.2 Validation of a Particle attached to the Wall

The reliability of calculating fluid dynamic forces acting on spherical particles by the present LBM code was already demonstrated for a wide range of particle Reynolds numbers (i.e. 0.3 to 480) by Hölzer and Sommerfeld (2009). These simulations captured the main features of the flow structure around the sphere and the drag coefficient was predicted with reasonable accuracy. In order to ensure the proper performance of the model for calculating the forces on particles in close contact, a widely considered test case is chosen where a particle is attached to a plane wall and is exposed to a linear shear flow (Fig. 2.6). The results of the present simulations are compared with available analytic results, experimental correlations or other simulations. This situation is also very similar as the problem considered in this contribution, where small drug particles are attached to a much larger carrier particle. The plane wall is just the limiting case with a carrier particle of diameter infinity. For the particle cluster carrier particle Reynolds numbers up to 200 were examined. This implies that for the size ratio $D_{drug}/D_{carrier}$ = 5 µm/100 µm the fine particle Reynolds number is at most 10. Consequently, the validation test case was simulated for Reynolds numbers between 0.01 and 10, respectively.

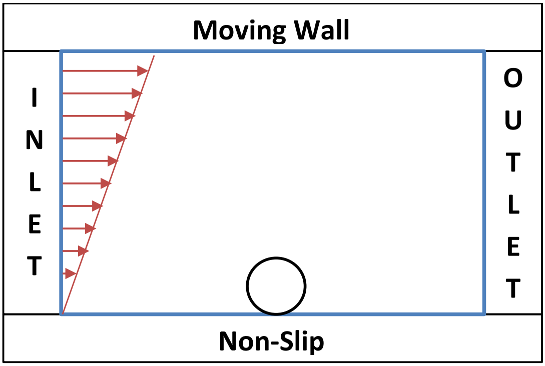

Fig. 2.6 Boundary conditions for the simulation of a particle attach to the wall under the linear shear flow; the moving wall indicates the full-slip boundary condition; the outlet boundary has zero gradients for all parameters.

The numerical calculations were performed for a rectangular domain where the particle is placed in the middle on the bottom wall (Fig. 2.6). In this case the particle was in direct contact with the wall and fluid properties were assigned to the solid nodes within the particle near the contact point (see Section 2.1.4). The upper wall is moving with a predefined velocity in order to induce the linear shear flow and the desired particle Reynolds number. At the side faces symmetry boundary conditions are applied. For this validation the drag coefficient is plotted versus the particle Reynolds number and the lift coefficient versus the shear Reynolds number. The particle Reynolds number for this situation is defined with the barycentre velocity ($U_{bc} = R_P \cdot G$), where G is the shear rate:

$$Re_p = \frac{\rho D_P (R_P G)}{\mu} \qquad 2.13$$

On the other hand the shear Reynolds number of the particle is given by (Crowe, et al., 2012):

$$Re_S = \frac{\rho D_P^2 G}{\mu} \qquad 2.14$$

This implies that for the present simple case, i.e. linear shear flow with zero velocity at the wall, $Re_S = 2 \cdot Re_P$.

Before presenting the results of the resistance coefficients, computations were conducted to determine the required size of the computational domain. For each case the particles were resolved by 40 grid cells of the finest mesh when using three grid refinement levels as shown in Fig. 2.7.

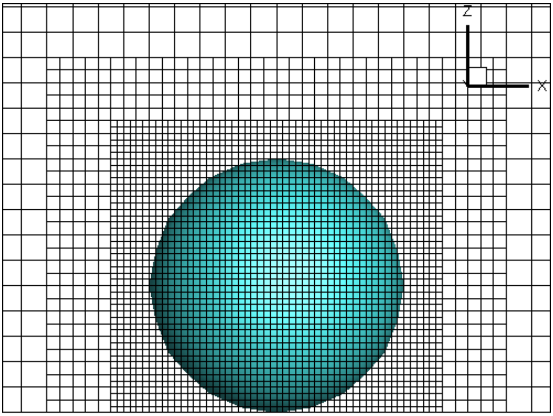

Fig. 2.7 Discretized mesh of a particle attach to the wall, 40 grids cells of the finest mesh pro particle diameter with three-level grid refinement (x,y,z refer to the length, width and height of the fluid domain).

The variation of the domain size in stream-wise direction (x/D) for fixed dimensions in the lateral and vertical directions (y/D = 12, z/D = 12) reveals that 18 particle diameters are sufficient to obtain coefficients which are independent of this dimension (Fig. 2.8 upper row). Moreover, the vertical dimension of the domain was varied by fixing the stream-wise and the lateral domain size (x/D = 18, y/D = 12). The results show (Fig. 2.8 lower row), that a vertical dimension of 18 particle diameters should be sufficient although the lift coefficient has not yet fully approached a limiting value. As a result of this study all the calculations for this test case were done for a domain size of x/D = y/D = z/D = 18. Three grid refinement levels were created and as a result the particle was resolved by 40 grid cells of the finest mesh. Consequently, the total number of grid cells was 5,953,158 for this case. The final results of the drag and the lift coefficients in dependence of Reynolds number are presented in the following.

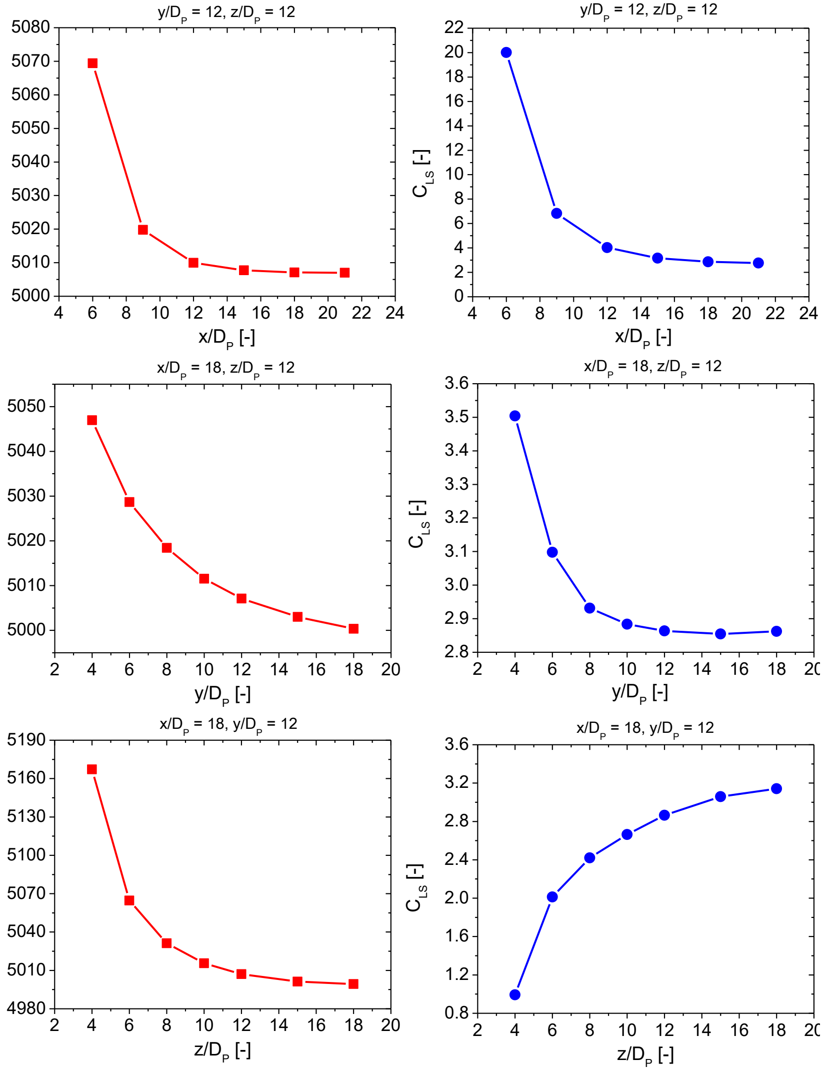

Fig. 2.8 Domain size validation for a particle attached to a plane wall in a linear shear flow; domain size normalized by particle diameter; upper row: variation of domain size in stream-wise direction for constant dimensions in the lateral and vertical directions (y/D = 12, z/D = 12); middle row: variation of lateral dimension of the

domain for x/D = 18, z/D = 12; lower row: variation of vertical dimension of the domain for x/D = 18, y/D = 12; left column: drag coefficient; right column: coefficient for slip-shear lift (3 refinement levels, particle Reynolds number Re = 0.01, shear Reynolds number Re_S = 0.02).

The drag coefficient is defined in the classical way with the simulated drag force F_D and the barycentre velocity:

$$C_D = \frac{F_D}{\frac{\rho}{2}\left(R_P G\right)^2 A_P} \qquad 2.15$$

The lift coefficient (i.e. for shear-slip lift) is defined according to the extended Saffman (1965) lift force (see Sommerfeld 2010, Crowe et al. 2012):

$$C_{LS} = \frac{F_L}{\frac{\rho}{2}\left(D_P G U_{bc}\right)^2 A_P} \qquad 2.16$$

Regarding the drag coefficient, the results of the present LBM simulations are first compared with the extended analytic solution of O`Neill (1968) given by:

$$C_{D,W} = 1.7009 \frac{24}{Re_P}\left(1 + 0.15\, Re_P^{0.687}\right) \qquad 2.17$$

Additionally other simulation results are considered. In the work of Derksen and Larsen (2011) a linear shear flow moving over a single particle attached to a wall has been simulated by the LBM and was used to validate their simulations with regard to domain size and grid resolution. The no-slip conditions at the surface of the particle were enforced by the immersed boundary method. Their results, for optimum settings, agree very well with those of O`Neill (1968) for $Re_P < 1$ (Fig. 2.9). For higher particle Reynolds numbers Zeng (2009) performed direct numerical simulations by a spectral element method. They presented results for the drag coefficient in case there is a very small gap between particle and wall (i.e. $\delta = 0.005D_p$). Also these results agree very well with the correlation according to Eq. 2.17 for a range of $2 < Re < 200$.

In the numerical simulations of Liu et al. (2011) a commercial code was used to calculate the drag coefficient of a particle placed on a wall within a boundary layer velocity field developing along a flat plate. The obtained drag coefficients are slightly below the extended correlation of O`Neill (1968); see Eq. 2.17.

In the present analysis the drag coefficient was calculated for a particle Reynolds number between 0.01 and 100 (Fig. 2.9). For higher Reynolds numbers the results match very well with the extended correlation (Eq. 2.17), however, at lower values a slight over-prediction is observed. This could be probably improved by further increasing the domain size, which would of course remarkably increase storage requirements and computational time.

Secondly the simulated lift coefficient on the particle attached to a wall in a linear shear flow was compared with analytic solutions and other simulations. The analytic result of Leighton and Acrivos (1985) for this situation and in the limit of very small shear Reynolds numbers gives a constant value of $C_{LS} = 2.935$ (Fig. 2.10). Another small Reynolds number analytic solution for a particle freely rotating in an unbounded linear shear flow is available from Saffman (1965), which is included here, as a limiting case:

$$C_{LS} = \frac{4.1126}{\sqrt{Re_S}} \qquad 2.18$$

The high Reynolds number simulations of Zeng (2009) yield lift coefficients which are below the line of Saffman (1965), which is of course not valid in this regime. By fitting these simulation data they proposed a correlation for the non-dimensional lift which is re-arranged to yield the lift coefficient as a function of shear Reynolds number as:

$$C_{LS} = \frac{2.4845}{\left(Re_S\right)^{0.44}} \tag{2.19}$$

This fitting curve is naturally not valid for $Re_S < 1$. From the depicted simulation results it is obvious that the lift coefficient is constant for $Re_S < 0.75$, in accordance with the result of Leighton and Acrivos (1985). With further increasing shear Reynolds number the lift coefficient is continuously decreasing, being smaller than the Saffman lift (Saffman 1965).

The simulation data of Derksen and Larsen (2011) seem to reflect nicely the transition between low and high Re_S although their value for the lift coefficient at $Re_S = 0.02$ is with $C_{LS} = 2.75$ slightly below the result of Leighton and Acrivos (1985). The present simulation results for the lift coefficient agree very well with the analytical result and the other simulations. Also the transition from low to high Re_S is captured by the LBM simulations. From the present simulation data a correlation for the non-dimensional lift can be obtained (red curve in Fig. 2.10) and is expressed by:

$$C_{LS} = \frac{c_5}{c_1 + c_2\left(Re_S\right)^{n} + c_3\left(Re_S\right)^{n/2} + c_4\left(Re_S\right)^{n/3}} \tag{2.20}$$

where $c_1 = -0.17321$, $c_2 = 0.15216$, $c_3 = -0.92055$, $c_4 = 0.94868$, $c_5 = 0.01486$ and $n = 0.20067$. The shear Reynolds number for this fitting curve is valid from 0.02 to 20.

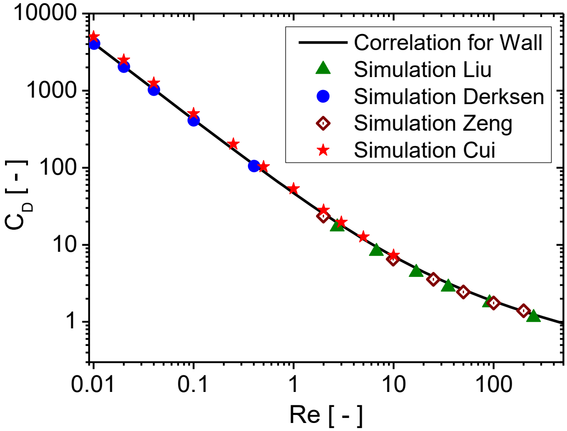

Fig. 2.9 Drag coefficient C_D of a particle attached to a wall as a function of particle Reynolds number *Re*, comparison of a universal correlation (Eq. 2.17) based on the result of O`Neill (1968) with several simulation data obtained by different numerical methods (Derksen and Larsen, 2011; Liu et al., 2011; Zeng et al., 2009).

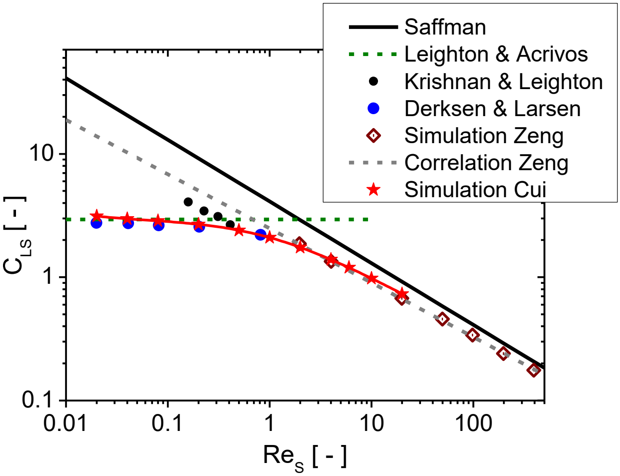

Fig. 2.10 Lift coefficient C_{LS} of a particle attached to a wall as a function of the shear Reynolds number Re_S, comparison of analytic results of Leighton and Acrivos (1985) for a wall attached fixed sphere and

Saffman (1965) for a freely rotating particle in an unbounded linear shear flow with several simulation data obtained by different numerical methods (Derksen and Larsen, 2011; Zeng et al., 2009).

2.3 Setup of Simulation for Particle Clusters

The simulations of the flow about a particle clusters consisting of one spherical carrier (in this case $D_{carrier}$ = 100 µm) and a mono-layer of randomly distributed fine spherical drugs (i.e. D_{drug} = 3 or 5 µm) first requires a generation process. This implies that the spatial distribution of drug powder on the surface of the carrier was created through a random procedure. The target value in this generation process is the degree of coverage which is calculated as the cross-section area of all drug particles divided by the surface area of a sphere with the diameter ($D_{drug}+D_{carrier}$). This coverage was varied between 10% and 50% in the present study. Consequently, the number of drug particles being randomly distributed on the carrier was obtained by assuring that only a mono-layer was produced, i.e. each fine particle must have contact with the carrier particle surface and no overlapping or contact of neighbouring drug particles was allowed. As an example, for the size ratio of 5 µm/100 µm and coverage degrees of 10% and 50%, 176 and 882 drug particles are obtained in total. Besides the size of the drug particles (i.e. D_{drug} = 3 or 5 µm), also the degree of coverage was varied between 10% and 50%. Simulating a cluster with the size ratio 3 µm/100 µm requires of course much more drug particles and a finer grid resolution which will be specified below. The coverage degrees 10% and 50% correspond to 472 and 2358 drug particles, respectively. For all these cluster properties the fluid dynamic forces on the drug particles in dependence of the angular location and the Reynolds number was calculated. The relevant Reynolds number is defined with the diameter of the carrier particle $D_{carrier}$ and the inflow velocity U_0:

$$Re = \frac{\rho D_{carrier} U_0}{\mu} \qquad 2.21$$

2.3.1 Computational domain and resolution

For the flow simulations, the particle cluster was centrally fixed in a rectangular flow domain illustrated in Fig. 2.11 and exposed to different kinds of flow situations. The present study mainly focusses on a particle cluster being placed into a laminar or turbulent plug flow, which are defined at the inlet. At the outlet a gradient free condition is applied and at all side faces symmetry boundary conditions are being used (Fig. 2.11). For the shear flow, the upper and bottom wall boundaries are changed into the moving wall which are moving with a predefined velocity in order to induce the desired particle Reynolds number. For the cluster calculations a very small gap of $0.01 \cdot D_{drug}$ was used between particles to prevent that one solid node belongs to two adjacent particles. Solid nodes within the drug particle near the contact point were assigned with fluid properties in order to allow correct calculations of the fluid forces on the drug particles (see Section 2.1.4).

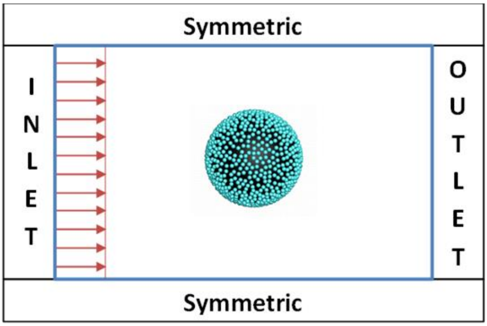

Fig. 2.11 Computational domain with applied boundary conditions.

The selection of the grid dimension (i.e. resolution of drug particles) and the size of the computational domain were based on an extensive parameter study for optimizing accuracy and computational effort. The number of refinement regions around the particle cluster was 3 to 5, depending on the flow conditions, i.e. *Re* number. First the required resolution of the fine drug particle was analysed by calculating the forces on these particles (i.e. in stream-wise and vertical direction) at different angular positions on the carrier particle (Fig. 2.12). For these simulations the domain size was fixed, however the grid size Δx was decreased with increasing resolution. For a low number of grids per drug particle the forces strongly fluctuate and only from 6 grids per particle diameter the forces remain almost constant, except for the vertical force at the stagnation point (Fig. 2.12 upper row, right). Nevertheless, with respect to computational requirements, in all the simulations the fine particle diameter was resolved by at least 6 grid cells on the fine mesh (see Fig. 2.3).

The analysis of the required domain size for obtaining grid-independent results is shown in Fig. 2.12 middle and lower rows. Here the stream-wise force on the fine drug particles is determined for various angular locations and plotted versus the domain size normalised by the diameter of the carrier particle. For Re = 10 all the forces smoothly approach an almost constant value at x/D about 8 (Fig. 2.12 middle row). The variation of the domain size in the lateral directions shows a similar behaviour and a value of y/D = z/D = 6.5 was selected for this Reynolds number (Fig. 2.12 lower row). The final selection of the dimensions of the computational domain for the low Re case is summarised in Table 2.1. For this case 4 refinement levels were used. The required domain size specified in terms of the carrier particle diameter and the number of meshes used for the coarse base-grid, was found to depend on the Reynolds number which is defined with the diameter of the carrier particle $D_{carrier}$ and the inflow velocity U_0. Consequently, for the higher Reynolds numbers the grid size was halved and the domain size slightly increased in all directions. Therefore only 3 refinement levels were necessary. The resulting total number of fluid nodes including refinement regions is also specified in Table 2.1.

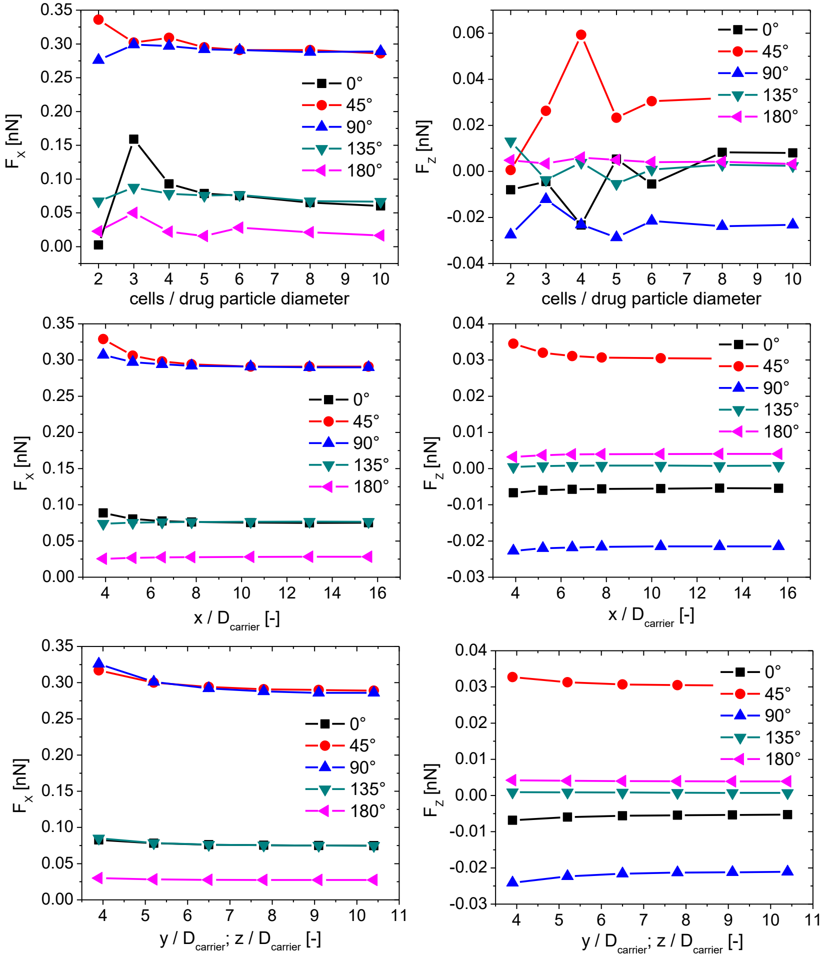

Fig. 2.12 Simulated forces on the fine drug particles in stream-wise (left column) and vertical (right column) direction at different angular positions on the carrier particle; upper row: variation of grid size with increasing resolution, i.e. cells per drug particle diameter ($x/D_{carrier}$ = 7.8, $y/D_{carrier}$ = $z/D_{carrier}$ = 6.5); middle row: variation of stream-wise dimension of the domain for $y/D_{carrier}$ = $z/D_{carrier}$ = 6.5; lower row: variation of lateral dimension of the domain for $x/D_{carrier}$ = 7.8 (Re = 10, D_{drug}/ $D_{carrier}$ = 10/100, coverage degree = 25%, 242 drug particles).

	Stream-wise direction	**Lateral direction**	**Total no. of grids**	**No. of refinement levels**
Re<100	$7.8 \cdot D_{carrier}$ $60 \cdot \Delta x_{coarse}$	$6.5 \cdot D_{carrier}$ $50 \cdot \Delta x_{coarse}$	3.8 million	4
Re>100	$10.4 \cdot D_{carrier}$ $160 \cdot \Delta x_{coarse}$	$9.1 \cdot D_{carrier}$ $140 \cdot \Delta x_{coarse}$	5.7 million	3

Table 2.1 Domain size specified in terms of carrier particle size and the number of cells for the coarse base-grid, as well as the total number of grid cells used for the fluid domain.

2.3.2 Parameter definition

In the present study mainly the forces acting on the fine drug particles in dependence of their location on the carrier surface and the Reynolds number were analysed. The forces relevant to possibly detach the fine particle are illustrated in Fig. 2.13. The fluid dynamic fore deriving from the LBM simulation is named as F_{total} which can be separated in a normal (F_n) and a tangential (F_t) component. The normal force is positive when it points out of the carrier surface. The adhesion force (i.e. van der Waals), F_{vdW}, is acting against the normal fluid force. The tangential force is always a positive value and is balanced by the friction force which is resulted from the Coulombs law of friction. The gravity of the drug particle is rather small and was thus neglected. All forces in Fig. 2.13 are relevant for a potential detachment by sliding or rolling (Ibrahim, et al., 2008).

The position angle in Fig. 2.13 indicates the angular location of the drug particle on the surface of the carrier particle with respect to the stream-wise direction. The position angle ranges from 0° to 180° and is symmetric with regard to the axis through the carrier particle in stream-wise direction. The position angle is 0° at the front stagnation point, is 90° in the middle of carrier, and is 180° in the rear stagnation point. Later the fluid dynamic forces on drug particles are studied based on its position angle.

The selection of parameters for LBM simulations were based on the RANS simulation introduced in section 1.3.

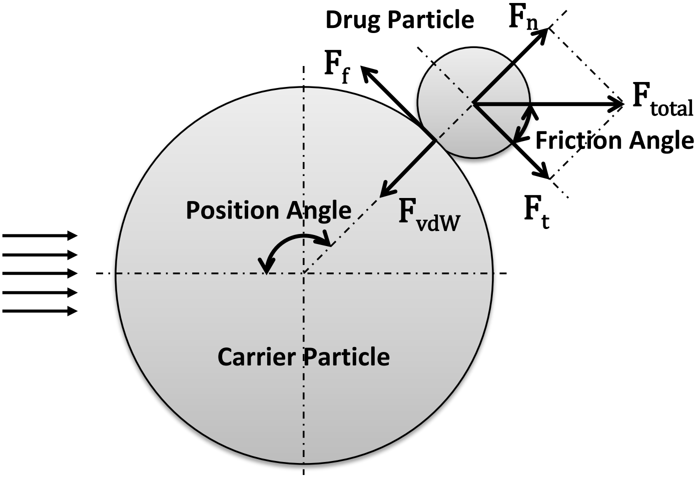
Drug Particle
F_n
F_f
F_{total}
Friction Angle
Position Angle
F_{vdW}
F_t
Carrier Particle

Fig. 2.13 Illustration of forces acting on the fine drug particles positioned on the large carrier particle.

2.4 Forces on Drug Particles in Laminar Flow

The main objective of the numerical studies is the evaluation of the normal and tangential fluid dynamic forces on the fine drug particles as a function of their position on the carrier, the Reynolds number, the degree of coverage and the size ratio ($D_{drug}/D_{carrier}$). The normal force may induce lift-off and the tangential force together with the normal component is relevant for sliding and rolling detachment (Ibrahim, et al., 2008). From this analysis it shall be estimated to what extent and under which conditions the fine drug particles may be detached from the carrier surface.

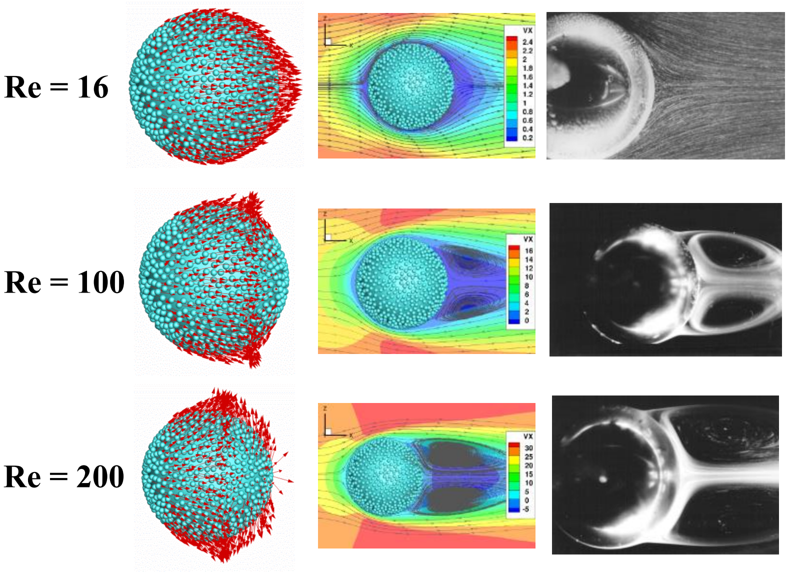

Fig. 2.14 Flow field about the particle cluster and resulting total forces on the drug particles for three particle Reynolds numbers; left column: total force vector on drug particles; middle column: streamlines over the particle cluster; right column: experiment measurement by Taneda (1956) (coverage degree = 50%, $D_{drug}/D_{carrier} = 5/100$).

Exemplarily all total force vectors for the drug particles are shown in Fig. 2.14 for different Reynolds numbers together with the flow field about the cluster. It should be emphasised that the force vectors only indicate the direction and not the magnitude for clarity (i.e. otherwise many force vectors would not be visible). The directions of the forces are strongly correlated with the flow structure about the cluster. Then the flow field is compared to the experimental work by Taneda (1956) from which gives a good correlation. For low Reynolds numbers no wake separation occurs and consequently the force vectors in the wake region are mostly directed away from the carrier in the stream-wise direction. At the equator region the force vectors are almost parallel to the carrier surface. With increasing Reynolds number the region of wake separation increases continuously, which is visible from the direction of the force vectors. Mostly they are directed towards the carrier or radially outward, especially for Re = 200. The angular region of beginning wake separation is clearly visible for all higher Reynolds numbers, since the force vectors are all directed away from the carrier in the radial direction.

Regarding the fluid dynamic behaviour of the clusters the drag coefficient is an important parameter. Therefore, these values were also calculated from the LBM simulations in dependence of the Reynolds number and the degree of coverage and compared to the frequently used correlation of Schiller and Naumann (1933) for a rigid sphere and the experiment data of Roos and Willmarth (1971). It should be noted, that for these calculations the outer cluster diameter (i.e. $D_{cluster} = D_{carrier} + D_{drug} = 110\ \mu m$) was used as an equivalent size. Since the particle clusters may be regarded as a kind of rough sphere, the drag coefficient is expected to be higher than that of a rigid sphere (Fig. 2.15). The drag coefficients for the clusters resulting from the LBM simulations show this behaviour. However, the drag increase also depends on the Reynolds number. For high Reynolds numbers only a marginal increase is observed, at least for the high degree of coverage. For low coverage the values fall onto the sphere correlation curve. When the Reynolds number is decreased the cluster drag becomes increasingly larger than the sphere drag. At high particle Reynolds number the separation behind the drug particles is stronger so that the flow passes mainly over the cluster mimicking a sphere with the cluster cross-section. With decreasing particle Reynolds number the flow moves more and more also between and around the drug particles whereby mainly the friction drag is increased. As shown in Fig. 2.15 and at Re = 77, the drag coefficient is increased with the help of turbulence. The reason for that will be explained later in Section 2.5. In conclusion, the drag coefficient of the cluster is predicted correctly being lager than the sphere drag and increasing with the degree of coverage.

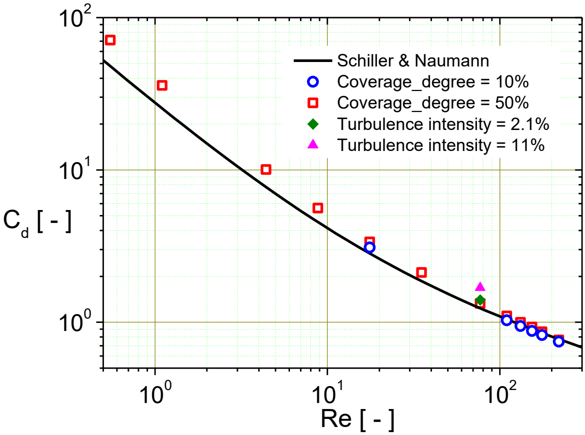

Fig. 2.15 Comparison of the drag coefficient resulting from present simulation results for a particle cluster with the correlation of Schiller and Naumann (1933) for a sphere (particle diameters $D_{cluster} = D_{sphere} = 110$ µm, coverage degree 10% and 50%, $D_{drug}/D_{carrier} = 5/100$).

As a consequence of the random variation of drug particle distribution on the surface of the carrier and the involved fluid dynamic interaction and flow separation between the drugs (see Fig. 2.26b) the fluid forces are different for the same position angle on the carrier surface and are also fluctuating in time. The temporal variation of the fluid dynamic forces depends of course on the carrier Reynolds number. For two Reynolds numbers (i.e. Re = 70 and 100) the temporal variation of the stream-wise force on a single drug particle located at a position angle of 61.5° is shown in Fig. 2.16 from the beginning to the end of the simulation (i.e. 25,000 time steps). As a result of the required assumption for the initial flow field, the force fluctuations are decreasing in time until a quasi-steady situation is reached. For the low carrier Reynolds number the final functions of the force are very small. When the Reynolds number increases these fluctuations also grow remarkably as a consequence of separations between the drug particles (see Fig. 2.26b), i.e. for higher coverage degree the flow is forced to mainly go across the fine drug particles. Additionally, small disturbances are created due to the assumed boundary conditions (see Fig. 2.11) in connection with the need of a finite size of the computational domain. In order to get statistically reliable values for the forces on each drug particle time averaging was done over a certain number of time steps towards the end of the simulation, i.e. when a quasi-steady-state is achieved. This averaging period was adapted according to the Reynolds number and typically ranged from 5,000 to 10,000 time steps for lower and higher Reynolds numbers. Expectedly, also the number of time steps required to reach a quasi-steady-state increased with carrier Reynolds number and was typically between 20,000 and 50,000.

The forces on the drug particles also depend on their specific arrangement on the carrier surface. In order to obtain reasonable approximations of the fluid dynamic forces on the drug particles over the surface of the carrier, i.e. in dependence of angular position, at least four simulation runs were conducted, for each condition with a different randomised drug particle distribution (see Fig. 2.17). Since the flow about the particle cluster is axisymmetric for a plug flow, the forces on all the drug particles may be plotted in dependence of the position angle only (Fig. 2.18). Here all data points from the four simulation runs are shown for Re = 100. Due to the large scatter it is more convenient to consider the result of a polynomial fitting curve through these data points in the following. The maximum of the total force in this case is found at an angle of about 50° from the front stagnation point, where the boundary layer on the cluster is very thin and the streamlines are squeezed together (see Fig. 2.14). This is also the region with the largest scatter of the forces. Within the wake region on the back side of the cluster, i.e. beyond an angle of about 110° at Re = 100, the total force on the drug particles is much smaller. In addition, the scatter of the total force is considerably lower in this region (Fig. 2.18). The PDF of the total force on the drug particles in the range of the maximum (i.e. 40° – 60°) can be closely represented by a normal distribution function (Fig. 2.19), which will simplify the modelling of detachment at a later stage.

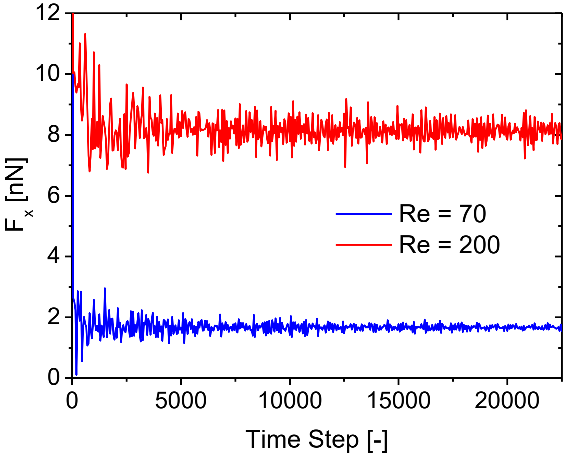

Fig. 2.16 Temporal variation of stream-wise force on a single drug particle at a position angle of 61.5° for two Reynolds numbers (coverage degree = 50%, $D_{drug}/D_{carrier}$ = 5/100, Δt = 0.7 ms).

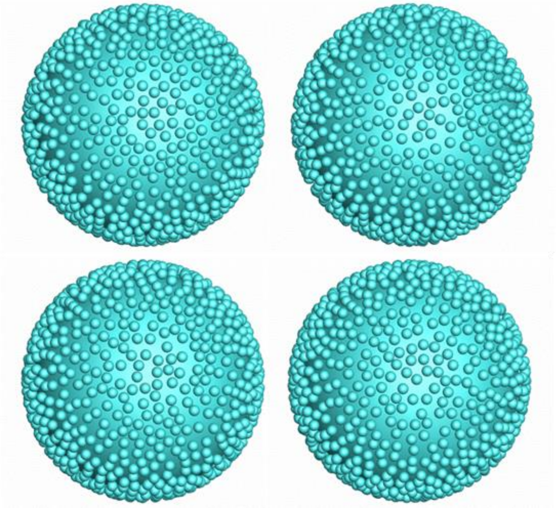

Fig. 2.17 Four times random distribution of drug particles (coverage degree = 50%, $D_{drug}/D_{carrier}$ = 5/100).

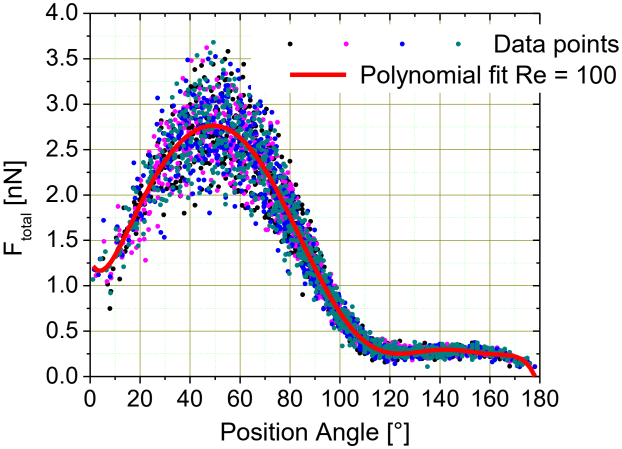

Fig. 2.18 Total force on all the drug particles in dependence of position angle for four different random distributions (coloured dots) and resulting polynomial fitting curve (Re = 100, coverage degree = 50%, $D_{drug}/D_{carrier}$ = 5/100).

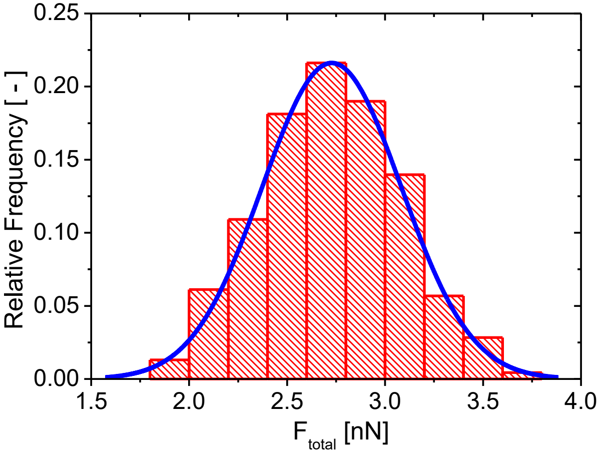

Fig. 2.19 PDF of total force between position angle 40 – 60 degree; Ftotal; mean = 2.73 nN, standard deviation = 0.36 nN (Re = 100, coverage degree = 50%, Ddrug/Dcarrier = 5/100).

2.4.1 Particle Reynolds number

The magnitude of the fluid dynamic forces and the angular location of the force maximum largely depend on the Reynolds number, as indicated in Fig. 2.14 and Fig. 2.18. The fitting curves for the normal force on the drug particles are shown in dependence of the position angle for different Reynolds numbers in Fig. 2.20. As to be expected, the magnitude of the force is increasing with free stream velocity (i.e. Reynolds number). In the front section of the cluster (i.e. position angles smaller than 40 – 50°) the normal force is of course negative implying that these drug particles cannot be detached as they are pushed towards the carrier. Beyond this stagnation region the normal force becomes positive allowing for lift-off detachment of the drug particles when it becomes larger than the van der Waals force. To enable a judgment on the detachment probability however measurements of the van der Waals force are required.

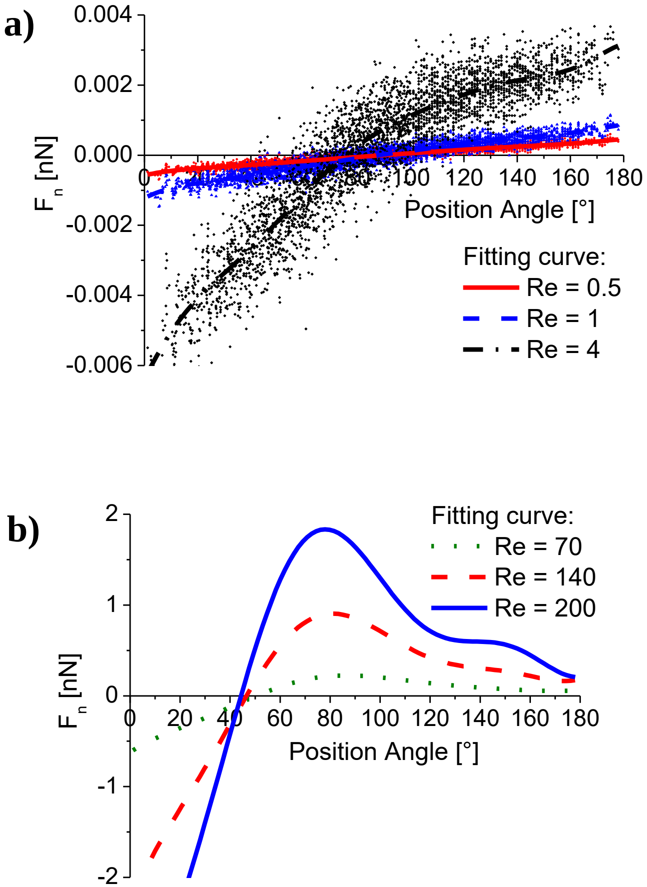

Fig. 2.20 Fitting curves for the normal force on the drug particles as a function of position angle for different Reynolds numbers; a) low Re regime, b) high Re regime (coverage degree = 50%, $D_{drug}/D_{carrier}$ = 5/100).

In the regime of small particle Reynolds numbers the normal force increases continuously from the front to the rear stagnation point (Fig. 2.20a), which is also obvious from Fig. 2.21. As a result of the wake separation behind the particle the maximum of the normal force is continuously shifted towards the front side of the particle. For higher Reynolds numbers (Fig. 2.20b) the maximum in the normal force is found just in front of the equator (i.e. between about 75° to 85°).

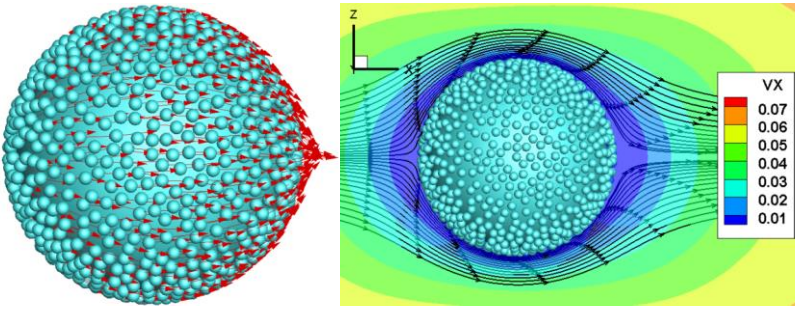

Fig. 2.21 Flow field about the particle cluster and resulting direction of total fluid forces on the drug particles for Re = 0.5 (coverage degree = 50%, $D_{drug}/D_{carrier}$ = 5/100).

The normal force maximum and the respective angular location are both summarised in Fig. 2.22 as a function of Reynolds number. The highest normal force at Re = 200 is only 1.8 nN which is far below any measured value of the van der Waals force (Cui, et al., 2014). Consequently, the drug particles cannot be detached from the carrier through lift-off. The location of maximum normal force continuously moves from the rear of the cluster to the front side, approaching a limiting value of about 78° (Fig. 2.22).

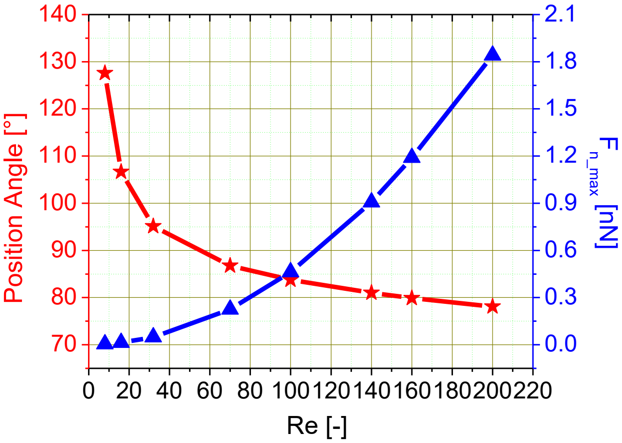

Fig. 2.22 Magnitude and angular location of maximum normal force determined from the fitting curves in dependence of Reynolds number (coverage degree = 50%, $D_{drug}/D_{carrier}$ = 5/100)

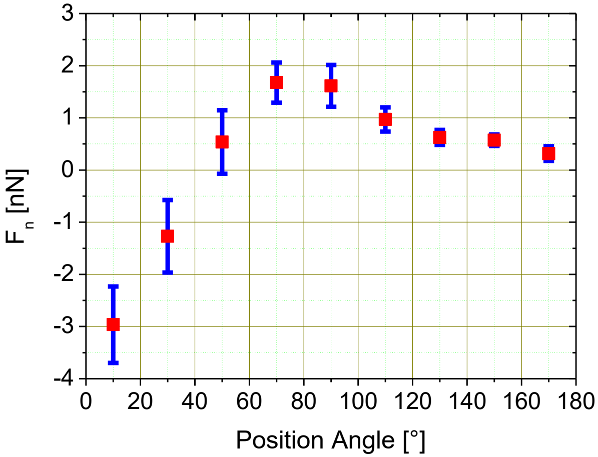

Fig. 2.23 Standard deviation of the normal force on drug particles in dependence of position angle (Re = 200, coverage degree = 50%, $D_{drug}/D_{carrier}$ = 5/100).

In Fig. 2.23 the normal force experienced by the drug particles is evaluated in a certain angular bin. The symbols indicate the mean values averaged over an angular range of 20° and the vertical bars correspond to the standard deviation of the normal force distribution in this angular range. The standard deviation (scatter of normal force) decreases remarkably while increasing the position angle. Although the normal force is negative in the front section of the cluster, a potential sliding or rolling detachment may happen due to the large standard deviation of the normal force.

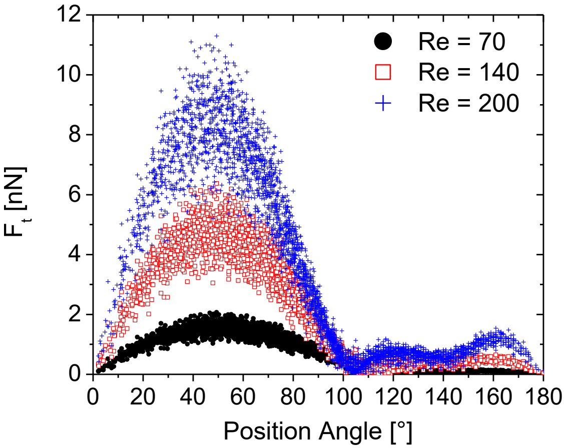

Fig. 2.24 Tangential force on the drug particles as a function of position angle for different particle Reynolds numbers (coverage degree = 50%, $D_{drug}/D_{carrier}$ = 5/100)

The magnitude of the tangential force on drug particles with respect to position angle for different particle Reynolds numbers is plotted in Fig. 2.24. Here again the individual tangential forces acting on each of the drug particles resulting from the four simulation runs are shown in order to illustrate the scatter of the data, which is remarkably increasing with particle Reynolds number as explained above. The distributions with respect to the angular position show a similar behaviour as the total fluid dynamic force (see Fig. 2.18). The maximum tangential force is always found at the front hemisphere of the carrier around a position angle of 50° from the front stagnation point. Here the streamlines for the flow around the cluster are squeezed together yielding high velocities in the vicinity of the cluster (thin boundary layer) whereby also the force vectors are almost parallel to the surface. In the wake region, the magnitude of the force vectors is very small and in some cases they are pointing away from the carrier particle surface (see Fig. 2.14) yielding eventually very small values for the tangential force (Fig. 2.24).

2.4.2 Coverage degree

The technical process of coating carrier particles with the drug powder (also called blending) is realised in a powder mixer. Therefore, a more or less random distribution of the fine powder is obtained; sometimes also including clusters and agglomerates, which are undesired. With respect to drug powder detachment and delivery to the lung, agglomerates should be avoided since they will deposit already in the upper airways due to inertia. In order to quantify the influence of coverage degree on the drug detachment within the inhaler also this effect was analysed through numerical simulations, exemplarily shown here for Re = 100. The simulation results reveal that with decreasing coverage the normal force is increasing (Fig. 2.25). This is an obvious result since in the case of large coverage the flow is going more or less across the drug particles somehow imitating a larger particle. For low degree of coverage the flow about the drug particles becomes again attached to the surface of the carrier behind each drug particle. Hence, the next drug particle is exposed to a stronger flow. This effect is illustrated in Fig. 2.26 showing typical streamlines across the drug particles for low and high degree of coverage. This effect will be of course more pronounced when the Reynolds number decreases and the separation regions behind the drug particles are diminishing. As a consequence, in producing the blends, it should be tried to achieve a low coverage in order to obtain higher fluid dynamic forces and have a better precondition for drug powder detachment in an inhaler.

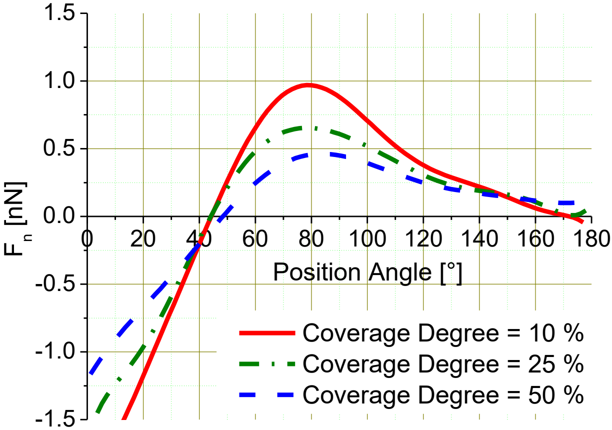

Fig. 2.25 Fitting curves for the normal force on the drug particles as a function of position angle for different degree of coverage (Re = 100, $D_{drug}/D_{carrier}$ = 5/100).

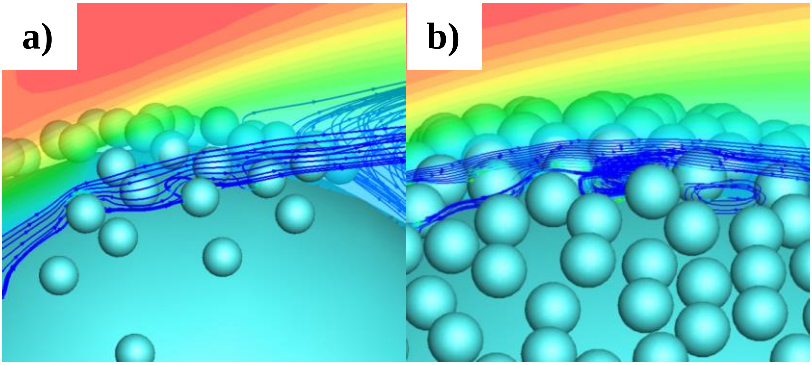

Fig. 2.26 Zoom of the flow structure around the particle cluster for different coverage, a) 10%, b) 50% (Re = 200, $D_{drug}/D_{carrier}$ = 5/100).

2.4.3 Size ratio

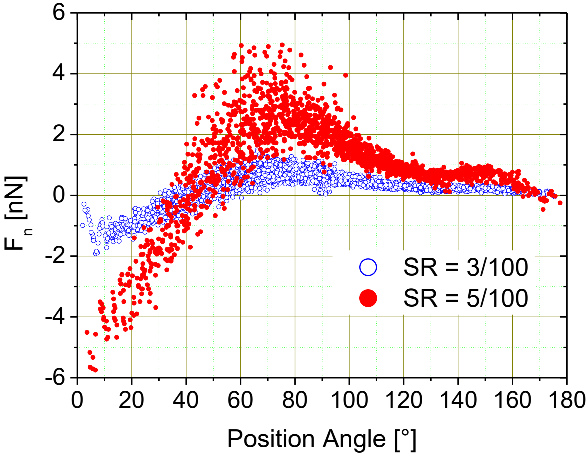

Fig. 2.27 Simulation data and fitting curves for the normal force on the drug particles as a function of position angle for different size ratio (Re = 200, coverage degree = 25%).

Particle size ratio (SR = $D_{drug}/D_{carrier}$) also plays an important role for detachment (see Fig. 2.27). As mentioned above, the drug particles should be smaller than 5 µm in order to ensure that they reach the alveoli of the lung. For comparing different particle sizes, additional simulations were performed for a drug particle diameter of 3 µm. In this case the drug particle diameter was also resolved by 6 cells. The domain size x × y × z was $10D_{carrier} \times 8D_{carrier} \times 8D_{carrier}$ and 5 refinement levels were used in this case. As a result, the simulation was done with 13.6 million fluid cells in total, i.e. solid cells are not counted. As to be expected, the normal force is drastically reduced when decreasing particle size, since the fluid dynamic force is proportional to the cross-section of the particles. Consequently, when the drug particles become smaller a detachment of the particles by fluid dynamic forces becomes more difficult. On the other hand of course the adhesion force will be different. In practice where the drug particles generally have a size distribution, this effect can reduce the efficiency of an inhaler.

2.4.4 Shear rate

Finally, also simulations with a shear flow were realized. For that purpose the upper and lower boundaries of the flow domain were considered as a solid wall with no-slip conditions (see Fig. 2.11). In order to obtain relatively high shear rates and a certain stream-wise (i.e. to the right) gas velocity on the particle centre the upper wall was moved to the right with a higher velocity then the lower wall being moved to the left. The conditions considered yielded a Reynolds number of 70 and a shear rate of 100,962 s^{-1}. This was actually the highest shear rate which could be realized in the simulations. The comparison of the normal force on the drug particles in dependence of the position angle for the case with plug and shear flow is shown in Fig. 2.28 together with the resulting flow structure about the particle cluster. It should be noted, that the shear flow across the cluster is not axisymmetric. Therefore, the normal forces on the drug particles on the front side of the carrier (i.e. up to an angle of about 50°) show a large scatter. The maximum forces appearing at a position angle of about 80° to 90° are almost identical with those obtained from the plug flow. The wake region behind the cluster has almost disappeared under shear flow conditions and the flow is mainly going upward around the cluster. This yields a normal force which is even smaller than in the plug flow case. Consequently a shear flow is not more effective for the detachment of the drug particles from the carrier.

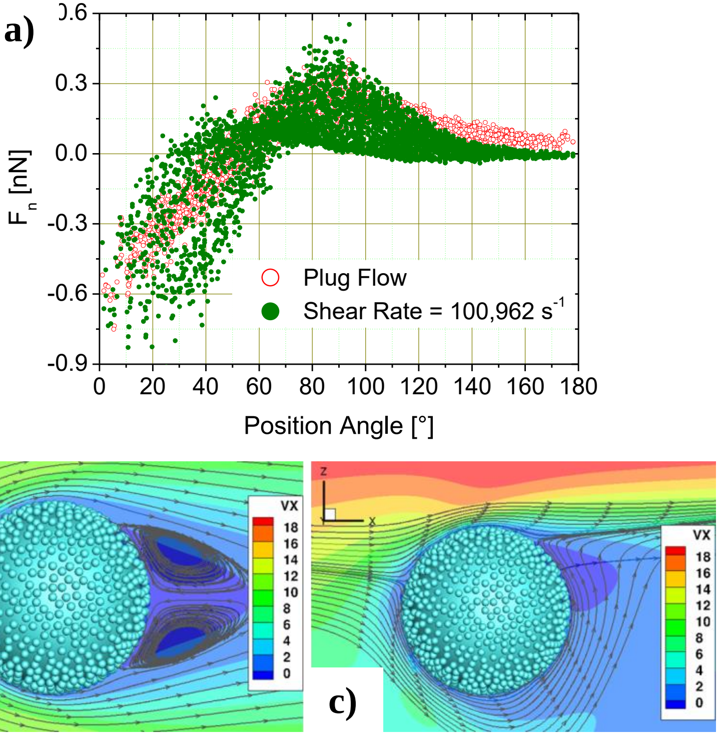

Fig. 2.28 Comparison of plug and shear flow about the particle cluster at identical Reynolds number (Re = 70); (a) normal forces in dependence of the position angle; (b) flow structure for the plug flow; (c) flow structure for the shear flow (coverage degree = 50%, $D_{drug}/D_{carrier}$ = 5/100).

2.5 Validation of Turbulence Generation

As mentioned in connecting with the OpenFOAM simulation (Section 1.3), high turbulence intensity was found in the swirl chamber and near the grid of the inhaler device. The turbulence intensity can reach up to a mean value of 7.4% under the flow rate of 70 L/min (Cui, et al., 2014). Hence the demand of LBM simulations for a highly turbulent flow interacting with a turbulence generator is considerable.

The simplest way for turbulence generation is to take a mean velocity profile with superimposed random fluctuations. However, due to a lack of energy in the low wave number range, this pseudo turbulence is immediately damped to zero, and the result is eventually identical to a laminar inflow. Based on a careful review of available literature, three typical turbulence generation methods are studied in the following sections.

2.5.1 Decaying grid turbulence

Djenidi in 2006 proposed a grid-generated turbulence model in which a grid made up of four by four floating flat square elements is located near the inlet boundary as shown in Fig. 2.29. The turbulence intensity can be modified by changing the size of the grid. As shown in Fig. 2.29, the boundary condition of the grid is non-slip and hence a boundary layer is generated near the grid.

In order to develop the turbulence a long channel is required (see Fig. 2.30). Along the stream-wised direction, the fluid velocity fluctuates a lot in the near grid region and then is decreased and becomes steadier. As mentioned by the author, it’s helpful to acquire a faster convergence if a fluctuating velocity profile is given in the beginning of the simulation.

The velocity fluctuations (u' / U_{mean}) is calculated along with the downstream distance x/M (x is the longitudinal direction and M is the spacing between the grid elements) as shown in Fig. 2.31. A linear decrease of the velocity fluctuations happens along the stream-wised direction. Therefore, it's hard to control the turbulence intensity by this method. Additionally, the simulation is very expensive since a large domain is required (Fig. 2.30).

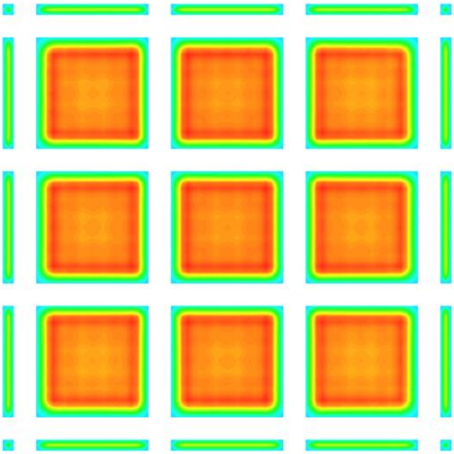

Fig. 2.29 Velocity contour in the cross section area of the grid by the grid generated turbulence method (*porosity = 0.64*).

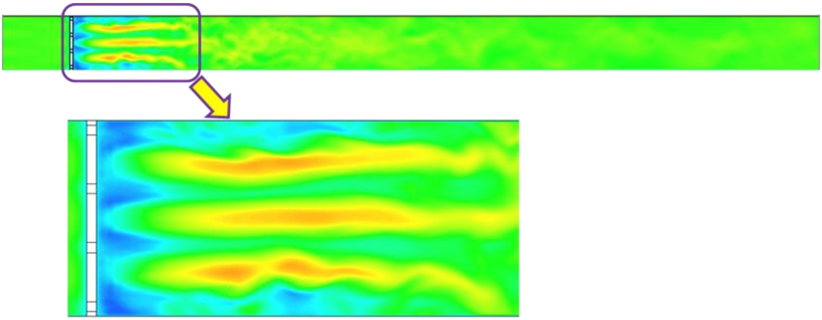

Fig. 2.30 Velocity contour along the stream-wised direction by the grid generated turbulence method (*porosity = 0.64*).

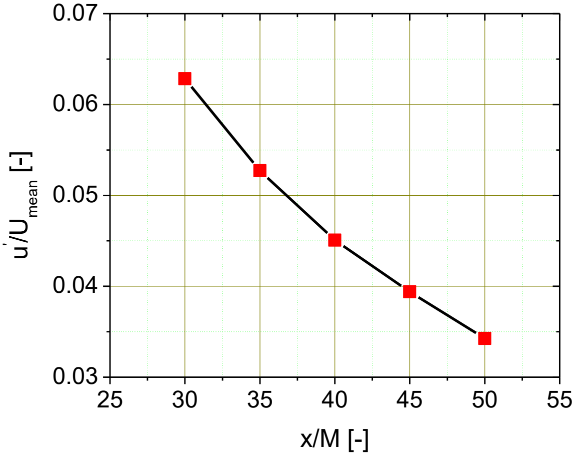

Fig. 2.31 Velocity fluctuations as a function of the downstream distance (*porosity = 0.64*).

2.5.2 Homogeneous isotropic turbulence

Eswaran and Pope in 1988 used a spectral forcing scheme to generate the homogeneous isotropic turbulence (HIT). Recently, Ernst & Sommerfeld in 2012 were implemented this method to the present LBM code and studied the inertial colliding particles. Turbulence is realized by generating a force in spectral space and introducing it as a change of velocity in the flow field. As a result, motion is created at large length scales. This is the basis for the development of motion at small length scales in form of an energy cascade which dissipates over time.

In HIT, the fluid domain is defined as an equal sized cube (Fig. 2.32). All the boundaries are set as the periodic boundary condition. The turbulence is generated all over the fluid domain and the mean velocity on each node keeps zero. In order to determine a non-zero mean velocity, an extra plug flow is added at the inlet. Moreover, a stationary particle is put into the middle of the domain as shown in Fig. 2.32. The particle Reynolds number is controlled by the plug flow and the turbulent kinetic energy can be changed by the forcing amplitude of spectral forcing scheme.

Fig. 2.32 gives a comparison of the flow field under two different turbulence intensities. The streamlines around the particle fluctuate instantaneously and become more unsteady when the turbulence intensity rises up (Fig. 2.32 right). The velocity on each node relies on its neighbouring nodes by the scheme and hence vortexes are generated inside the domain at larger turbulence intensities.

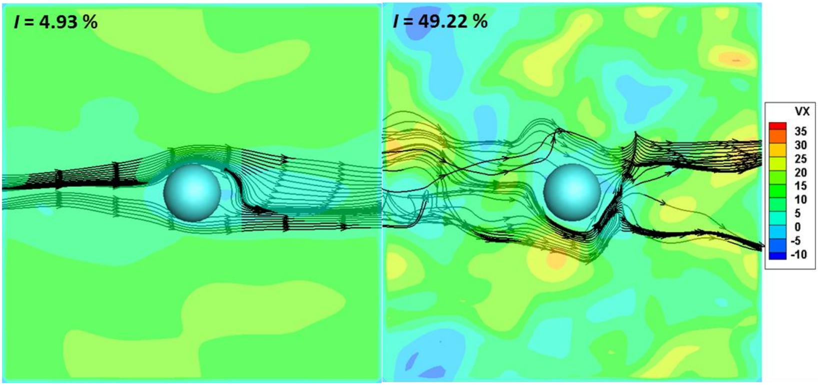

Fig. 2.32 Flow field around a particle under the HIT plus a plug flow; left: I = 4.93%; right: I = 49.22% (Re = 100).

Fig. 2.33 depicts the mean drag coefficient of the particle for different particle Reynolds numbers and turbulence intensities. The mean drag coefficient decreases significantly while increasing the particle Reynolds number. For a certain particle Reynolds number (e.g. Re = 100), the mean drag coefficient increases when the turbulence intensity rises up (see Fig. 2.33). Same phenomenon is also found by Uhlherr & Sinclair (1970) for small particle Reynolds numbers (Re = 10 to 600).

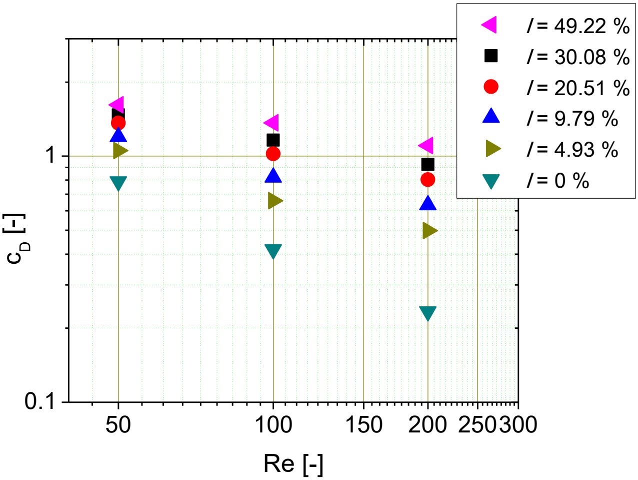

Fig. 2.33 Mean drag coefficient on a spherical particle as a function of the particle Reynolds number for different turbulence intensities.

The relationship between the turbulence intensity and the forcing amplitude of spectral forcing scheme (Eswaran & Pope, 1988; Ernst & Sommerfeld, 2012) is illustrated in Fig. 2.34. The turbulence intensity increases while increasing the forcing amplitude. This correlation offers an opportunity to control the turbulence intensity by altering the forcing amplitude.

Although the HIT model has lots of advantages, there exists a limitation of this method. The local grid refinement method (Section 2.1.3) can hardly be implemented into this model. Hence lots of fluid nodes are generated during the simulation and the capacity of our computer cluster is too limited to solve. However, this method works well for the simulation of equal-sized particles.

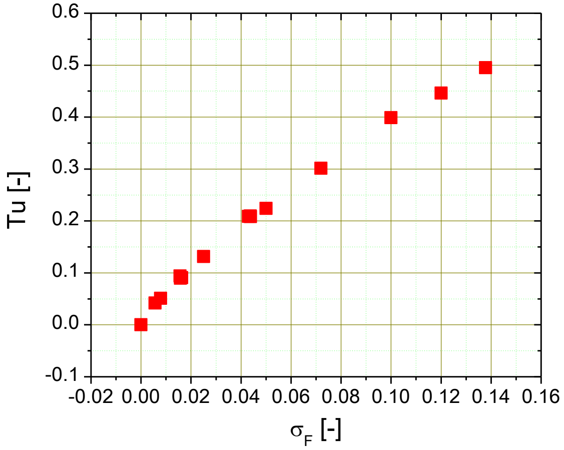

Fig. 2.34 Turbulence intensity as a function of the forcing amplitude of the spectral forcing scheme (Re = 100).

2.5.3 Digital filter based turbulence inflow data generation

After the abandon of previous methods, we did lots of effort on the literature study and finally found one method which is suitable for our agglomerate structure and is easy to be implemented into the present LBM code. This method is proposed by Klein, et al. who in 2003 introduced an efficient inflow generation technique based on a digital filter. The filter induces correlations of the fluctuating components in space and time on the randomly generated data for each grid node of the inlet boundary. The method was successfully used to generate inflow boundary conditions for a DNS of a plane turbulent jet flow (Klein, et al., 2003) and the evaporation of a water droplet at 8°C in a turbulent free air stream of 252°C (Huber, et al., 2011). This method will be briefly introduced in section 2.5.3.1. After the implementation of this method into the present LBM code, numerical simulations are perform for different particle Reynolds numbers and turbulence intensities. The simulation results are than compared to the results of laminar flow (see Section 2.4). The possibility of drug detachment by the turbulence will be studied later in Section 3.1.7.

2.5.3.1 Numerical algorithm

In order to generate turbulent inflow boundary conditions the mean velocity profile $\overline{u_i}\left(x,y,z\right)$ (x indicates the stream-wised direction, y and z indicate the lateral and vertical directions) is superimposed by velocity fluctuations $u_i^{'}$ which is a common approach for the generation of artificial turbulence. At first a provisional three dimensional signal $U_i\left(x,y,z\right)$ is generated for each of the velocity components. According to Lund et al. (1998), U_i have to satisfy the condition $\overline{U_i}=0$ and $\overline{U_iU_j}=1$, and then perform the following transformation: $u_i=\overline{u_i}+a_{ij}U_j$, with the amplitude tensor given by

$$\left(a_{ij}\right)=\begin{pmatrix} \left(R_{11}\right)^{1/2} & 0 & 0 \\ R_{21}/a_{11} & \left(R_{22}-a_{21}^2\right)^{1/2} & 0 \\ R_{31}/a_{11} & \left(R_{32}-a_{21}a_{31}\right)/a_{22} & \left(R_{33}-a_{31}^2-a_{32}^2\right)^{1/2} \end{pmatrix} \qquad 2.22$$

where R_{ij} is the correlation tensor which may be known from experimental data and u_i is the finally needed velocity signal.

In the digital filtering technique proposed by Klein et al. (2003), U_j is based on a multidimensional Newton method which can define the length scale locally for each coordinate direction, and satisfies the autocorrelation condition. More details can be found in their paper. It should be noted that this method is time consuming in three dimensional simulations; in our case the computational time is doubled.

2.5.3.2 Simulation setup

In order to analyse the turbulence two parameters are introduced. The turbulence intensity, also often referred to as turbulence level, is defined as:

$$I = \frac{1}{U_0}\sqrt{\frac{2}{3}k}; \text{ with } k = \frac{1}{2}\left(u_x'^2 + u_y'^2 + u_z'^2\right) \qquad 2.23$$

where U_0 the mean velocity, k the turbulent kinetic energy and u_i' are the mean fluctuating velocity components. The turbulence intensity cannot be pre-defined before simulation runs. We recode the velocity components of several grids in the fluid domain during the simulation and then calculate the turbulence intensity in the end.

Another parameter is the integral time scale T which indicates the time costs of the simulation and is given by:

$$T = \int_0^\infty r(\tau)\, d\tau \qquad 2.24$$

where τ is the time lag and $r(\tau)$ is the normalized autocorrelation function as following:

$$r(\tau) = \frac{\langle u(t)\, u(t+\tau)\rangle}{\langle u^2 \rangle} \qquad 2.25$$

The selection of the grid dimension (i.e. resolution of drug particles) and the size of the computational domain were based on an extensive parameter study for optimizing accuracy and computational effort (Cui & Sommerfeld, 2015). The drug particles were resolved by 6 grid cells of the finest mesh by using three grid refinement levels. The domain size was selected by $10.4D_{carrier} \times 9.1D_{carrier} \times 9.1D_{carrier}$ (length × width × height), in total 5.7 million grids were produced. The digital filter (Klein, et al., 2003) was applied at the inlet boundary with 140 × 140 grid cells.

In the turbulent simulation, the length scale was fixed with 1/3 of the carrier diameter (approximately $5\cdot\Delta x_{coarse}$, Δx_{coarse} is the size of most coarse grid), and the filter width was set as 10 in order to fulfil the condition of digital filtering technique (Klein, et al., 2003). In fact the selected length scale and filter width nearly reach to the limitation of our computer capacity. Hence the turbulence intensity was not controlled by the length scale, instead by varying the fluctuation levels (Eq. 2.22). In the present study only the turbulence effect is focused, the size ratio was fixed of 5 µm/100 µm and the coverage degrees kept 50%, finally 882 drug particles were generated in total.

2.5.3.3 Forces on drug particles in turbulent flow

The reliability of the digital filtering technique is validated at the beginning. Simulations without particles are performed for two different mean velocities under the same turbulent kinetic energy. The velocity components are recorded at 15 fluid nodes which lie in the middle of lateral and vertical directions along the stream-wised direction with the same distance.

The velocity contour at the inlet boundary is shown in Fig. 2.35. The instantaneous flow velocity is significantly increased by the turbulence kinetic energy compared to the mean flow velocity, 30 m/s. Many small vortexes can be found inside the domain and its maximum size is predefined as $1/3\cdot D_{carrier}$. The size of vortex has large influence on the computational expense, so it’s better to choose a small value. The velocities on each grid and its adjacent grids remain continuous, since the velocities on the neighbouring nodes are correlated by the filter width.

The probability density distribution of the velocity components on the fluid node which lies in the middle of the fluid domain is illustrated in Fig. 2.36. The mean fluid velocity is pre-defined with 30 m/s in the stream-wised (x) direction and 0 m/s in the lateral and vertical (y and z) directions. All velocity components can be closely represented by a normal distribution function. The standard derivation of the probability density function (PDF) can be controlled by a_{ij} in Eq.2.22.

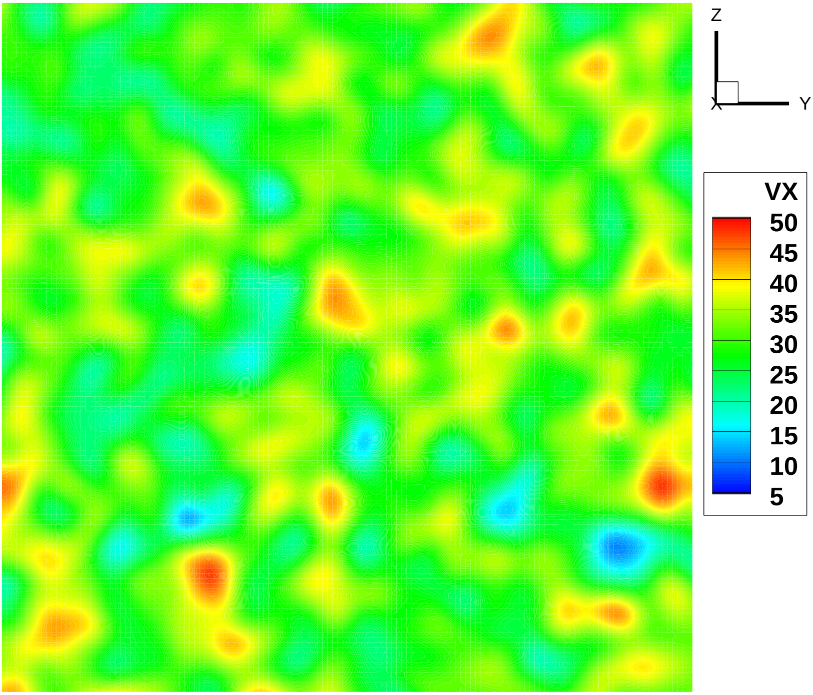

Fig. 2.35 Instantaneous colour contours of the velocity component in x-direction (stream-wise direction) at the inlet boundary of the computational domain at the end of the simulation, i.e. after N = 84,500 time steps (U_{mean} = 30 m/s, I = 15.5% (in the center of the domain), integral time scale T_{int} = 60 s).

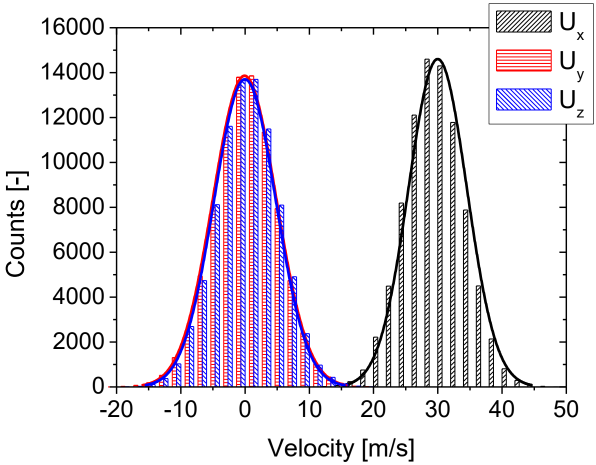

Fig. 2.36 Probability density distribution of the velocity components on the fluid node in the middle of fluid domain; U_x denotes the velocity component in the stream-wised direction; U_y and U_z signify the velocity components in the lateral direction (U_{mean} = 30 m/s, I = 15.5%, averaging period 64,500 to 84,500 time steps, T_{int} = 60 s).

Fig. 2.37 offers an overview of the turbulence intensity recorded at 15 points along the stream-wised direction with the same spacing, $10\Delta x$, for two different fluid velocities. Both cases share same turbulent kinetic energy, k. The turbulence intensity shows a sharp decrease between 0 to $60\Delta x$, follows by a steady period up to $120\Delta x$, and then decreases again near the outlet boundary. At the next step, the particle cluster is placed in the middle of the fluid domain ($x = 80\Delta x$). The turbulence intensity is measured at the fluid node of $x = 60\Delta x$ which can closely represent the turbulence intensity experienced by the particle cluster.

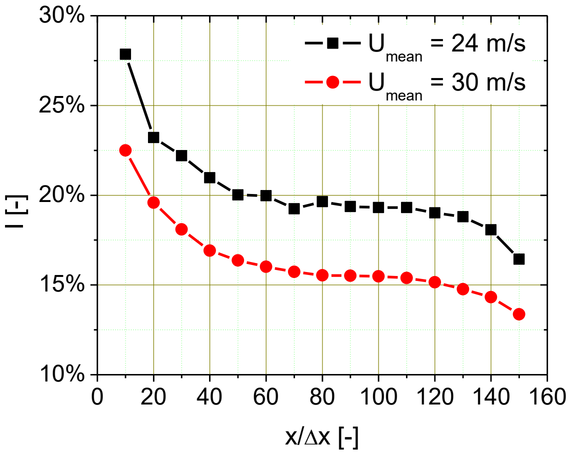

Fig. 2.37 Decaying of the turbulence intensity along the stream-wised direction by the digital filtering technique for different fluid velocities ($k = 11\ m^2/s^2$).

After the validation of the digital filtering technique, simulations are performed with the considered particle cluster by varying particle Reynolds numbers and turbulent kinetic energies. Exemplarily all total force vectors for the drug particles are shown in Fig. 2.38 for laminar and turbulent flows together with the flow field about the cluster. The force vectors only indicate the direction and not the magnitude for clarity (i.e. otherwise many force vectors would not be visible). The directions of the forces are strongly correlated with the flow structure about the cluster. For the laminar flow, I = 0.3%, the force vectors are almost parallel to the carrier surface and a wake region is developed at the rear of the carrier. It should be noted that in laminar flow the turbulence intensity are not exactly zero, since the developing of the wake region produces more noise at higher particle Reynolds numbers (Cui & Sommerfeld, 2015). For the turbulence flow, I = 9.0%, the force vectors are disordered by the turbulent and the streamlines become non-symmetric and fluctuate instantaneously. From the velocity legends, it is obvious that the flow velocity in turbulent flow is much higher than the one in the laminar flow.

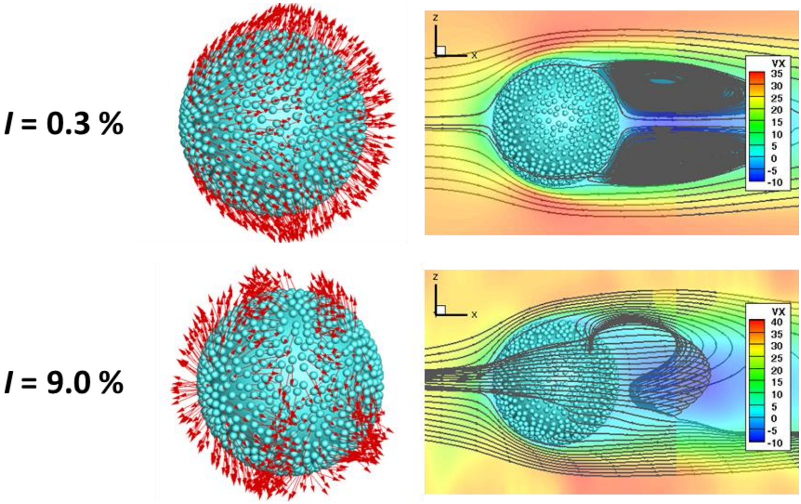

Fig. 2.38 Force vectors and streamlines of the particle cluster for the laminar and turbulence flows (Re = 200, coverage degree = 50%, $D_{drug}/D_{carrier}$ = 5/100, time step N = 75,000).

The temporal variation of the normal force on the drug particle which has the largest time averaged normal force for both the laminar and turbulent flows are presented in Fig. 2.39. The black line indicates the laminar flow while the red line denotes the turbulence flow. It is obvious that a quasi-steady state is reached after 10000 time steps and the fluctuation of the laminar flow is much smaller than the turbulent flow. The maximum normal force was increased from 5 *nN* to 51 *nN* due to the turbulence. Compared to the other influential parameters, turbulence is very effective in increasing the normal force. As may be identified from Fig. 1.3 the highest turbulence levels are found in the swirl chamber and just downstream of the grid. From the inhaler calculations it was also found that the probability of higher turbulence intensities than considered here is rather large.

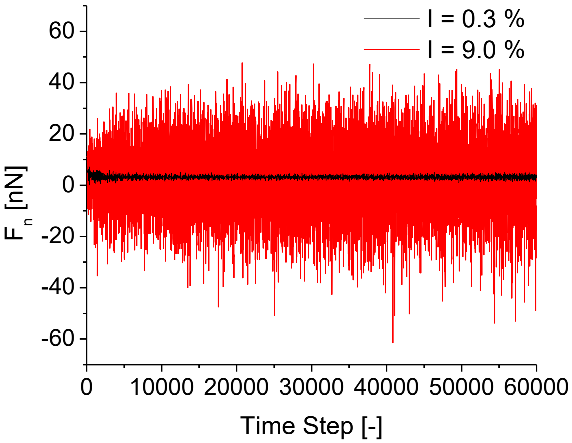

Fig. 2.39 Temporal variation of the normal force on the drug particle which has the largest time averaged normal force (position angle = 85°) for both the laminar and turbulent flows (Re = 200, coverage degree = 50%, $D_{drug}/D_{carrier}$ = 5/100).

3 Flow Detachment Model

To predict the efficiency of drug delivery to the alveoli of the lung, the foremost essential work is to analyse the detachment of drug particles, e.g. how much percent and under what conditions the drugs detach from the carrier particle. Most of the detachment models from literature are based on the combined effect of convective flow and turbulence (Soltani & Ahmadi, 1999; Reeks, et al., 1988; Ibrahim, et al., 2008). In the present study, it is aimed at analyzing the effect of laminar and turbulent flow as well as surface roughness separately. The fluid dynamic force calculated by LBM is employed to detachment criterions. One reason is that the fluid dynamic force of drugs cannot be analytically determined, because the detachment occurs on a curved surface (from large carrier particle surface) and the fluid dynamic force varies depending on its locations (position angle). The other reason is that concerning the precision, in some complicated situations, (e.g. on rough surfaces), the numerical solution of full-resolved particles is more precise than the analytical solutions.

The drug particles detach from carrier particle under various conditions. The carrier particles are much larger than the very fine drug particles so that can be considered as a plane wall. With this simplification it is reasonable to simplify the removal of drug particles from such a large carrier particle surface as the detachment of micro-sized particles from a plane surface exposed to the shear flow. Soltani (1999) and Ibrahim (2008) summarized the detachment model of particles from plane wall. Furthermore, the carrier surface could be modified in order to achieve a lower adhesion force. In this project different surface roughness were produced by the project partner (Cui, et al., 2014). Then the detachment of particle from rough wall should also be taken into consideration. The rough wall detachment model can be referred to the study of Reeks (1988) and Ziskind (1997). The above detachment models are studied in the following two sections, respectively.

3.1 Plane Wall Detachment Model

3.1.1 Detachment criterion

The particle can be detached from a surface by direct lift-off, sliding or rolling. The gravity of drug particle introduces non-symmetry of force distribution on carrier surface. However it is comparatively rather small, therefore the gravity of drug particle is neglected in the following part. The normal force F_n and tangential force F_t (see Fig. 3.1) are the components of the fluid dynamic force from the LBM simulation results. The van der Waals force F_{vdW} is the only adhesion force considered here, and can be measured by using atomic force microscopy (AFM) measurement (see Section 3.1.2).

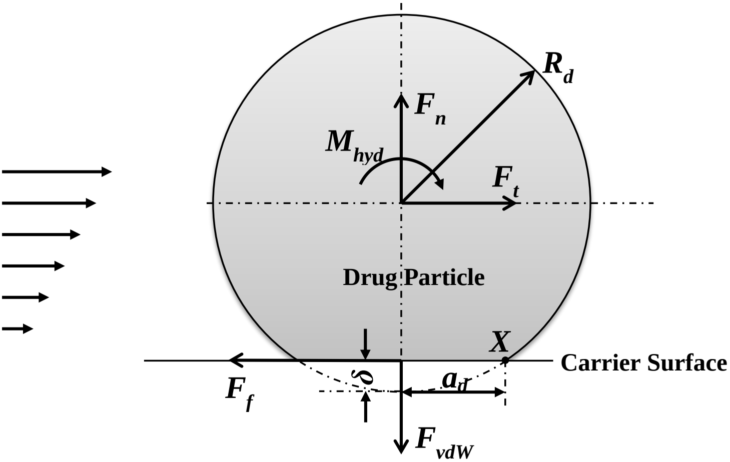

Fig. 3.1 Spherical particle deposited on an ideal plane wall with contact area and relevant forces.

For the lift-off and sliding detachment, the criterions are given:

$$\text{Lift-off: } F_n > F_{vdW} \tag{3.1}$$

$$\text{Sliding: } F_t > F_f \tag{3.2}$$

where

$$F_f = \mu_d \left(F_{vdW} - F_n \right) \qquad 3.3$$

μ_d is the static friction coefficient between the drug and the carrier. When the normal force is larger than the van der Waals force, the lift-off detachment happens; also the sliding detachment is determined by a force balanced between tangential and friction force. The rolling detachment results from a balance of torques around point X in Fig. 3.1, given by:

$$\text{Rolling: } M_{hyd} + R_d F_t + a_d F_n > a_d F_{vdw} \qquad 3.4$$

The hydrodynamic moment M_{hyd} about the drug particle centre of mass is directly obtained from the LBM simulations. The moment balance around point X (Fig. 3.1) is obtained together with the normal F_n and tangential F_t forces acting also at the centre of mass (Eq. 3.4) and the torque arms, namely the drug particle radius R_d (note that here the very small deformation δ is neglected) and the contact radius of the drug particle a_d. The analytical solution of M_{hyd} is given by Hubbe (1984) under the condition that the particle experiences the linear shear flow and very small particle Reynolds numbers, and can be expressed by:

$$M_{hyd} = 0.37 \cdot F_t \cdot R_d \qquad 3.5$$

In Hubbe’s paper, the coefficient of above equation is 0.399. After revision of equations, the correct value should be 0.37 or 0.3699. When two particles or a particle with a plane surface are in contact a finite size circular contact area with the radius a_d develops (i.e. ideally for perfectly smooth objects). The contact area can be determined by the JKR adhesion model (Johnson, et al., 1971). The size of this contact area is depending on the effective normal force, P, and the adhesion properties which are material dependent and are summarised in the composite Young's modulus K. Moreover, the contact radius depends for two particles in contact on the effective radius R.

$$a_d = \sqrt[3]{\frac{R}{K}\left(P + 3\gamma\pi R + \sqrt{6\gamma\pi RP + \left(3\gamma\pi R\right)^2} \right)} \qquad 3.6$$

where

$$P = F_{vdW} - F_n \tag{3.7}$$

$$R = \frac{D_d \cdot D_c}{2 \cdot \left(D_d + D_c\right)} \tag{3.8}$$

$$K = \frac{4}{3} \cdot \left[\frac{1-\sigma_d^2}{E_d} + \frac{1-\sigma_c^2}{E_c} \right]^{-1} \tag{3.9}$$

where γ is the adhesion surface energy, D_d, D_c, E_d, E_c and σ_d, σ_c respect to the diameter, the Young's modulus and the Poisson's ratio of the drug and carrier particle. It should be emphasized that the contact area might be also affected by the way how the fine particles are deposited. Table 3.1 presents the interested material properties for drug and carrier particles from the particle supplier.

	Drug Particle	**Carrier Particle**
Diameter	5 μm	100 μm
Density	1290 kg/m³	2500 kg/m³
Young's Modulus	2.15 GPa	63 GPa
Poisson Ratio	0.3 [-]	0.24 [-]

Table 3.1 Material properties of drug and carrier particles used in the simulations.

The first order approximation of Eq. 3.6 is in fact the Hertz model (Hertz, 1896). The JKR theory of adhesive contact uses a balance between the stored elastic energy and the loss in surface energy, and considers the effect of contact pressure and adhesion only inside the area of contact. Some other models are also available to calculate the contact radius. For example, Derjaguin-Muller-Toporov (DMT) model (Derjaguin, et al., 1975) is an alternative model for adhesion contact. It assumes that the contact profile remains the same as in the Hertzian contact but with additional attractive interactions outside the area of contact. The main difference between the two models is that, JKR assumes linear elastic deformation in contact area whereas DMT assumes quadratic elastic deformation. In the present study the van der Waals force is directly measured by AFM. Therefore the analytical solutions of F_{vdW} in JKR and DMT theories become useless. Only Eq. 3.6 is applied for evaluating the contact radius.

3.1.2 Experimental measurement

As discussed above, some parameters in the detachment criterion are unknown and need to be measured, specifically the van der Waals force, the friction coefficient, the adhesion surface energy and the surface roughness. The van der Waals forces acting between carrier particles and drug particles were determined via atomic force microscopy (AFM). The friction coefficients were determined via a FT4 Powder Rheometer. Moreover, the adhesion surface energy of untreated and physically modified glass beads was determined from the static contact angles of water and α-bromonaphtalene. This part of work is mainly completed by our project partner S. Zellnitz from Technische Universität Graz.

Table 3.2 shows that the adhesion force between surface modified glass beads and salbutamol sulphate is lower than the adhesion force between untreated glass beads and salbutamol sulphate. This can be explained by the rougher surfaces of the modified glass beads. When introducing surface roughness the contact area between the glass beads and the salbutamol sulphate particle is reduced and hence also the adhesion force between them. Glass beads modified with tungsten carbide for 8 hours are rougher than glass beads modified with quartz for 4 hours, and so is the adhesion force lower between glass beads modified with tungsten carbide for 8 hours and salbutamol sulphate. More details about the experimental measurements can be found in Cui et al. (2014) and Zellnitz et al. (2013).

	Adhesion force [nN]	**Friction angle [°]**	**Friction coefficient [-]**	**Surface energy [mJ/m^2]**
Untreated	257.48 ± 59.67	4.49 ± 0.19	0.079 ± 0.003	53.36 ± 7.94
Q 4 h	127.83 ± 28.23	4.79 ± 0.34	0.084 ± 0.006	73.68 ± 5.61
TC 8 h	62.48 ± 52.96	6.34 ± 0.36	0.111 ± 0.0063	65.76 ± 2.99

Table 3.2 Measured adhesion force via AFM (atomic force microscope), wall friction angle and coefficient (mean values und standard deviations obtained out of 3 × 1250 measurements) and adhesion surface energy (mean value and standard deviation out of 20 measurements) for modified glass beads (Cui, et al., 2014).

3.1.3 Lift-off detachment

Lift-off detachment occurs when the normal force is larger than the van der Waals force (Eq. 3.1). As introduced above, the surface treatment method TC 8h created the smallest van der Waals force, and thus such surfaces have the largest propensity of the lift-off detachment. However, the data in section 2.4.1 to 2.4.4 demonstrated that the lift-off is not likely to occur even at high shear rates. The maximum frequent velocity in the inhaler device is calculated as 30 m/s (Fig. 1.3), and the particle Reynolds number is hence 200. While at Re = 200, the maximum normal force is around 1.8 nN (Fig. 2.22), which is far lower than the criterion detachment force, F_{vdW}, in TC 8h (62.48 nN). One prominent cause of the direct lift-off detachment from the plane wall is the turbulence effect. At Re = 200, the maximum normal force can reach to 48 nN (Fig. 2.39) under a turbulence intensity of 9.0%. The macro-scale simulation tells that the turbulence intensity can reach up to 50% in the near grid region inside the inhaler (Fig. 1.3). One should keep in mind that the measured van der Waals force is a stochastic data and has a large standard deviation. The lift-off detachment could occur on some drug particles where large normal forces locate under high turbulence intensities. However, to reach a high percentage detachment ratio is still a problem.

3.1.4 Sliding detachment

This section presents the results of LBM simulation of sliding detachment of drug particles from a carrier surface. Eq. 3.2 gives the theoretical criterion for the sliding detachment. Sliding of drug particles happens when the tangential force resulting from fluid dynamic force is larger than the friction force. The friction force is based on the static friction coefficient, the normal force and the van der Waals force (see Eq. 3.3). The friction coefficient as well as the van der Waals force are constant under a certain surface treatment method, while the normal and tangential components of the fluid dynamic force vary.

Fig. 3.2 exhibits the tangential force corresponding with friction force in the case of TC 8h. The squares are the data of the tangential force and the points signify the friction forces on each drug particles. When the tangential force is larger than the static friction force, the sliding detachment takes place. The scatter of the tangential force is larger than the friction force, and reaches the maximum value around 45° of position angle. As shown in this Fig., the sliding detachment mainly occurs at the front part (25° - 75°) of carrier near the front stagnation point. The vector of fluid dynamic force in this region is close to the direction of tangential force. Accordingly the major part of the fluid dynamic force is the tangential component, and therefore the maximum value of tangential force locates in this region. The scatter of the friction force is delimited approximately along a line, in sharp comparison with the tangential force. The reason is that the static friction coefficient and the van der Waals force are constant in the calculation (see Eq. 3.3). Meanwhile, the value of van der Waals force is much larger than the magnitude of the normal force (Fig. 2.20). As a result the magnitude of friction force has weaker fluctuations on each drug particles.

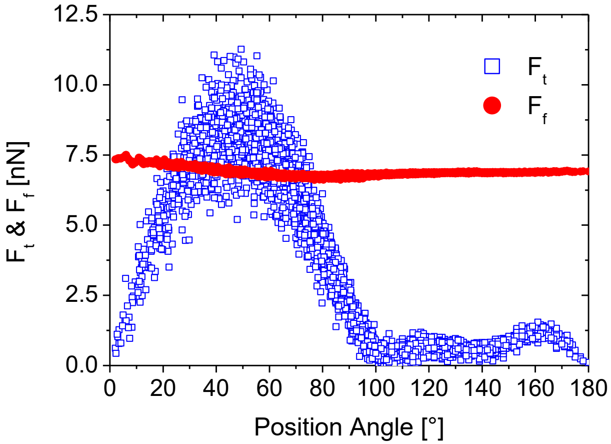

Fig. 3.2 Tangential force and friction force on drug particles as a function of position angle (Re = 200, coverage degree = 50%, $D_{drug}/D_{carrier}$ = 5/100, surface treatment: TC 8h).

Fig. 3.3 offers an overview of the sliding probability as a function of the Reynolds number and the surface treatment methods. The detachment probability is defined by the number of detached drugs divides the total number of drugs. As shown in Table 3.2, the values of the adhesion force, the static friction coefficient and the adhesion surface energy depend on the surface treatment method. Compared to the untreated carrier particle, the adhesion force was reduced significantly with the surface treatment. For untreated carrier, the sliding detachment reaches a 10% detachment probability at Re = 200. Among those surface treatment methods TC 8h has the smallest adhesion force, hence leads to the highest tendency of sliding detachment (Eq. 3.2 & 3.3), and finally reaches up to a detachment probability of 50% at Re = 200.

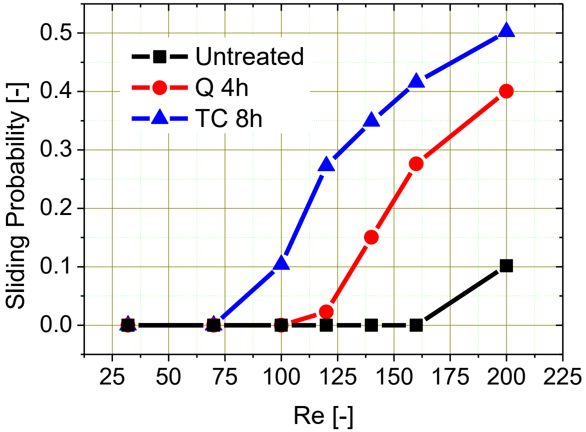

Fig. 3.3 Sliding probability of drug particles as a function of Reynolds number for different surface treatment methods ($D_{drug}/D_{carrier}$ = 5/100, coverage degree = 10%).

Fig. 3.4 shows the sliding probability as a function of the particle Reynolds number and the coverage degree for the TC 8h surface treatment. For a coverage degree of 50% and when the Reynolds number is smaller than 140, none of the particles begin to slide, because of the too small fluid dynamic forces. When the Reynolds number becomes larger than 140, some of the drug particles begin to slide and at a Reynolds number of 200 around 22% drug particles are being detached. For 10% coverage degree, the fluid dynamic forces on the drug particles are much higher and hence they begin to slide already at smaller Reynolds numbers (Fig. 3.4), and then finally around 50% drug particles are being detached by sliding. However, to reach 100% detachment by sliding is still not possible. In conclusion, sliding detachment is a much more probable event than the lift-off detachment, and nearly half of drugs begin to detach by sliding even without the turbulence.

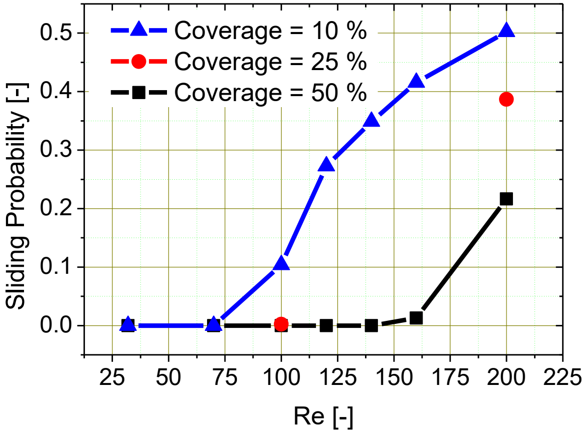

Fig. 3.4 Sliding probability of drug particles as a function of the Reynolds number for different coverage degrees ($D_{drug}/D_{carrier}$ = 5/100, surface treatment: TC 8h).

3.1.5 Rolling detachment

The determination of a possible rolling detachment is based on Eq. 3.4. An essential parameter in this equation is the contact radius of the drug particle, a_d. The contact radius is determined by the geometrical properties, the elastic deformation due to external loads as well as the adhesion surface energy, and was evaluated by JKR adhesion theory (Eq. 3.6 - 3.9). Fig. 3.5 shows the contact radius of drug particles as a function of their position angle. The maximum value was obtained at the front stagnation point of carrier particle, while the minimum value was found at position angle 80°. All the parameters in Eq. 3.6 are constant except the external load, which implies that the magnitude of the contact radius largely depends on the external load, P. As shown in Eq. 3.7, the external load reaches maximum when the normal force decreases to its maximum negative value. The fluid dynamic force pushes the drug particles onto the carrier at the front stagnation point, where the majority of the fluid dynamic force is composed of the normal force, whose value is negative, i.e. point into the carrier. As a result the contact radius has its maximum at the front stagnation point. Departing from the front stagnation point, the contact radius first decreases with the rise of the position angle, and then experiences an increase while approaching the back stagnation point. This is because of the wake developing behind the particle cluster at high Reynolds numbers (Fig. 2.14). The wake does not reduce the normal force but it changes its direction from positive to negative, and hence induces a larger *P* and increases the contact radius near the back stagnation point. However, the divergence of the contact radius is in a small-scale, i.e. 0.00023 µm. Since the van der Waals force is much larger than the normal force, the external load is limited to a narrow range (Eq. 3.7).

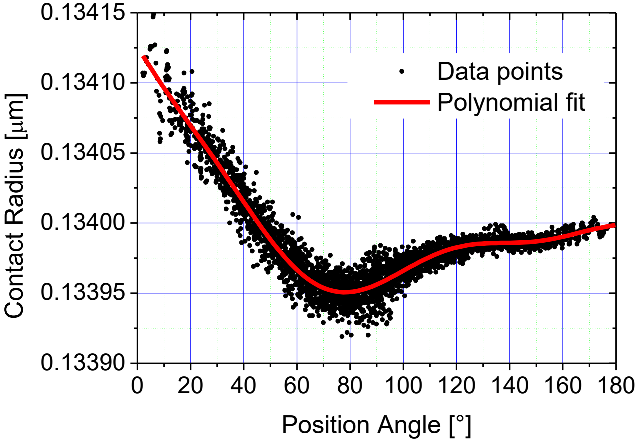

Fig. 3.5 Contact radius of drug particles as a function of the position angle (Re = 200, coverage degree = 50%, $D_{drug}/D_{carrier}$ = 5/100, surface treatment: TC 8h).

Fig. 3.6 exhibits the data points from the numerical (points) and analytical (squares) solution of the hydrodynamic torque around the mass centre of each drug particle. The analytical solution is given by Hubbe (1984) and is calculated according to Eq. 3.5. It should be noted that the tangential force in Eq. 3.5 comes from the simulation results. As shown in Fig. 3.6, the scale and tendency of numerical and analytical data are similar, whereas the analytical parabola becomes a little narrower. While decreasing the degree of coverage from 50% to 25% (Fig. 3.7), the hydrodynamic torque remarkably increased. It is reasonable due to the increase of the fluid dynamic force on drug particles (Fig. 2.25).

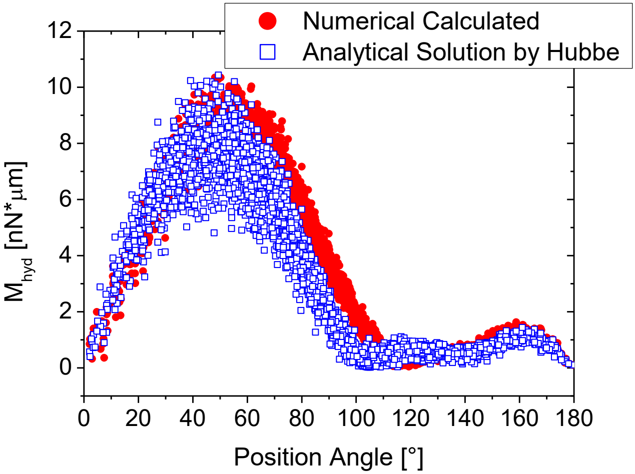

Fig. 3.6 The comparison of the numerical calculated hydrodynamic torque and the analytical solution by Hubbe (Eq. 3.5) as a function of position angle (Re = 200, coverage degree = 50%, $D_{drug}/D_{carrier}$ = 5/100, surface treatment: TC 8h).

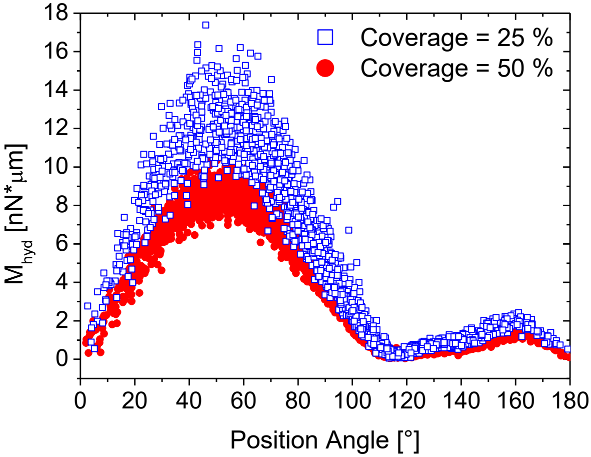

Fig. 3.7 The numerical calculated hydrodynamic torque as a function of position angle for different degree of coverage (Re = 200, $D_{drug}/D_{carrier}$ = 5/100, surface treatment: TC 8h).

The possibility of rolling detachment in dependence of position angle is again calculated from the simulation results by comparing the left and right hand side of Eq. 3.4 for each drug particle on the carrier (Fig. 3.8). The right hand side (points) includes the torque due to the adhesion force and the left hand side (squares) comprises the torque resulting from the fluid dynamic forces around point *X* in Fig. 3.1. Naturally, detachment occurs if the fluid dynamic torque is larger than the adhesion torque. The result (Fig. 3.8) shows that rolling detachment happens over a relatively wide angular range, i.e. from 10° to 90°, which is much larger than for sliding detachment (see Fig. 3.2).

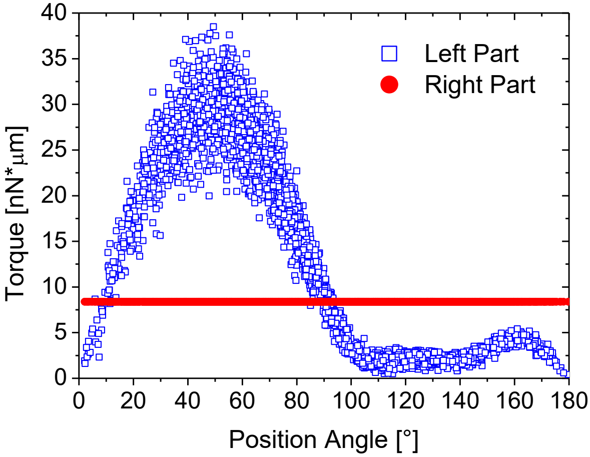

Fig. 3.8 Fluid dynamic torque (left hand side of Eq. 3.4) and adhesion torque (right hand side of Eq. 3.4) as a function of the position angle (Re = 200, coverage degree = 50%, $D_{drug}/D_{carrier}$ = 5/100, surface treatment: TC 8h).

In light of discussions above, it is possible to count the percentage of drug particles which can be detached by rolling. In Fig. 3.9, the rolling probability of different surface treatment methods (untreated, Q 4h and TC 8h) is plotted. At low Reynolds numbers none of the drug particles begin to roll due to the smallness of the fluid dynamic force. When the particle Reynolds number exceeds a certain value, there appears a rapid growth of the rolling probability. However, this tendency does not keep further, instead, the rolling probability rises slowly at higher Reynolds numbers. Referring to Table 3.2, it is found that the increase of the adhesion force has a negative impact on the rolling detachment due to the increase of adhesion torque (Eq. 3.4).

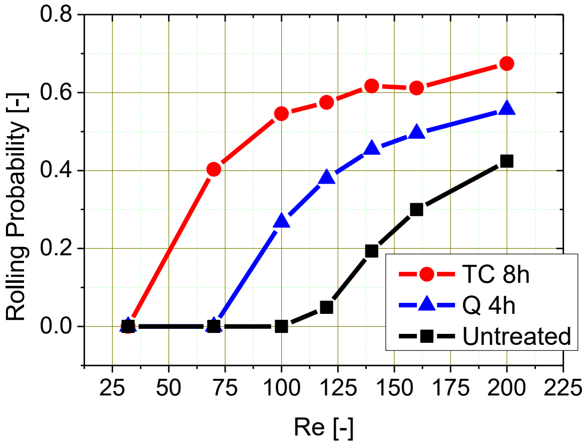

Fig. 3.9 The rolling probability of drug particles as a function of the Reynolds number for different surface treatment methods ($D_{drug}/D_{carrier}$ = 5/100, coverage degree = 10%).

Fig. 3.10 offers an overview of the rolling probability of drug particles under the TC 8h surface treatment method. For a coverage degree of 50% and when the Reynolds number is smaller than 70, none of the particles begin to roll, because of the too small fluid dynamic forces. While increasing the Reynolds number, some of the drug particles begin to roll and around 50% drug particles are being detached by rolling at Re = 200. For lower coverage degrees, e.g. 10%, the fluid dynamic forces acting on the drug particles are relatively higher (Fig. 2.25), hence bring more rolling probability on drug particles (Fig. 3.10), and finally around 67% drug particles are being detached by rolling.

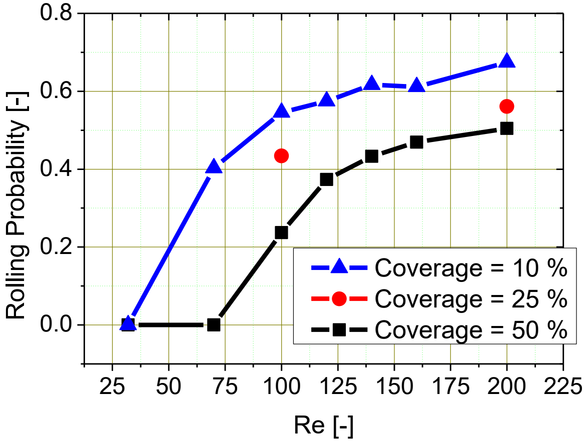

Fig. 3.10 The rolling probability of drug particles as a function of the Reynolds number at different coverage degrees ($D_{drug}/D_{carrier}$ = 5/100, surface treatment: TC 8h).

3.1.6 Comparison of the sliding and rolling detachment

Based on above results it is now also possible to calculate the detachment probability which is defined as the number of drug particles which may be detached in a certain angular bin (i.e. here 10°) over the number of particles being present in this angular range. For the coverage degree of 50% and a Reynolds number of 200 the detachment probability directly results from Fig. 3.2 and Fig. 3.8. It is obvious that the rolling detachment probability is considerably higher than that for sliding (Fig. 3.11a). For Re = 200 detachment is restricted to the front hemisphere, i.e. position angles smaller than about 90°. When the coverage degree is reduced, the detachment probability becomes larger since the fluid dynamic forces on the drug particles are growing (Fig. 3.11b). For a coverage degree of 10% at Re = 200 detachment due to rolling also happens on the rear of the carrier around a position angle of 160°. This is the result of the local maximum of the fluid dynamic torque seen in Fig. 3.8 which is becoming larger for decreasing coverage degree. If the Reynolds number is decreased to 100, rolling detachment on the front hemisphere is only slightly affected whereas rolling is vanishing at the rear. However, the probability of sliding detachment is clearly reduced.

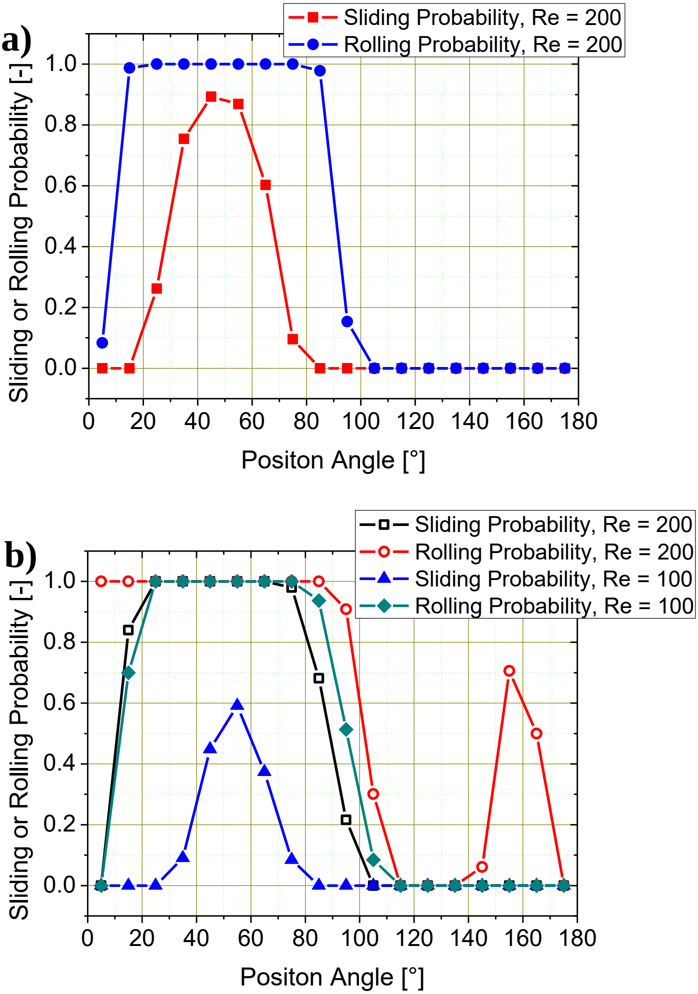

Fig. 3.11 Detachment probability due to sliding and rolling as a function of position angle for different Reynolds numbers; a) coverage degree

= 50%, b) coverage degree = 10%, ($D_{drug}/D_{carrier}$ = 5/100, surface treatment: TC 8h).

Considering the value of the detachment ratio under the same conditions, e.g. at Re = 200, the rolling probability is 67% in comparison with the sliding probability of 50%. It seems that the rolling detachment is easier than the sliding detachment, but is it true? To answer this question, go back to equation 3.2 - 3.4, from which yields a non-dimensional ratio:

$$Ratio = \left(\frac{M_{hyd} + R_d F_t + a_d F_n}{a_d} \right) \Big/ \left(\frac{F_t + \mu_d F_n}{\mu_d} \right) \qquad 3.10$$

If the variable *Ratio* is larger than one, the rolling detachment occurs first; if *Ratio* is smaller than one, the sliding detachment occurs first on the contrary. The *Ratio* is only evaluated for those drug particles which can be detached by both rolling and sliding. The result of Eq. 3.10 is shown in Fig. 3.12 for a Reynolds number of 100 and 200. The straight solid line indicates the critical value. Although some drug particles can be rolling at wider position angles (Fig. 3.8), no sliding happens in that region (Fig. 3.2). Therefore those points were excluded from the calculation of *Ratio*. As shown in Fig. 3.12, the drug particles which can be detached by both rolling and sliding are in the angular range 10° - 100° at Reynolds number of 200. And this angular range becomes narrower at Reynolds number of 100 since the fluid dynamic force is reduced. For the entire angular range rolling detachment will occur first. The statement that the rolling detachment occurs before sliding is not rigorous, since many parameters used for the detachment study are based on the surface treatment as well as the material properties. However, in the present work, based on the precondition given by Table 3.1 and Table 3.2, the rolling detachment always occurs earlier than the sliding one in the plane wall detachment model.

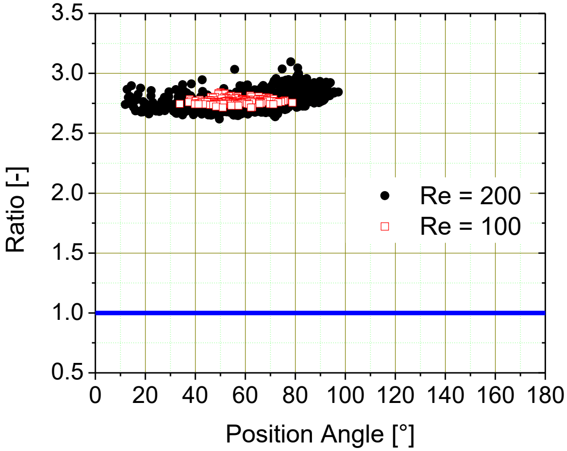

Fig. 3.12 Data points of *Ratio*, Eq. 3.10 (Re = 100 and 200, coverage degree = 10%, $D_{drug}/D_{carrier}$ = 5/100, surface treatment: TC 8h).

3.1.7 Sliding and rolling detachment in turbulent flow

The instantaneous fluid dynamic force fluctuates significantly under turbulent flow conditions (see Fig. 2.39). Therefore, it is no more suitable to use the mean force from a time averaging for the detachment analysis. Instead, we use the temporal normal and tangential force and calculate the instantaneous sliding and rolling probability determined from all drug particles on the carrier over a certain time period. Fig. 3.13 offers an overview of the instantaneous sliding and rolling probability over the last 10,000 time step (≈ 7 s) of the simulation. The red line refers to the sliding probability while the blue line corresponds to the rolling probability. In general the sliding and rolling probability fluctuate over time but keep in a good scale. The rolling rate (mean value = 98%) is higher than sliding ones (mean value = 75%) during the whole time process.

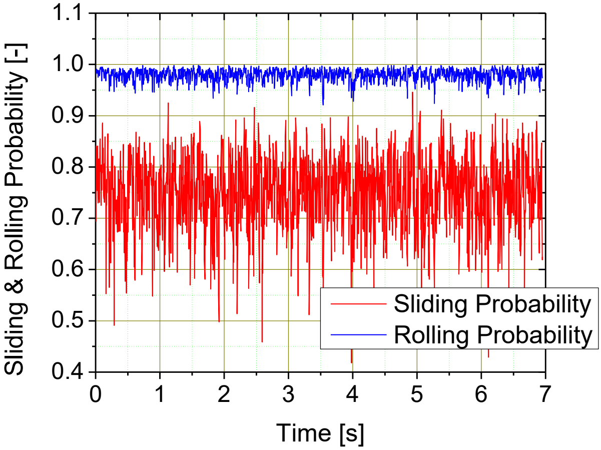

Fig. 3.13 Instantaneous sliding and rolling probability of the drug particles in turbulent flow over a time of 7 s (Re = 200, I = 9.0%, coverage degree = 50%, $D_{drug}/D_{carrier}$ = 5/100, surface treatment: TC 8h).

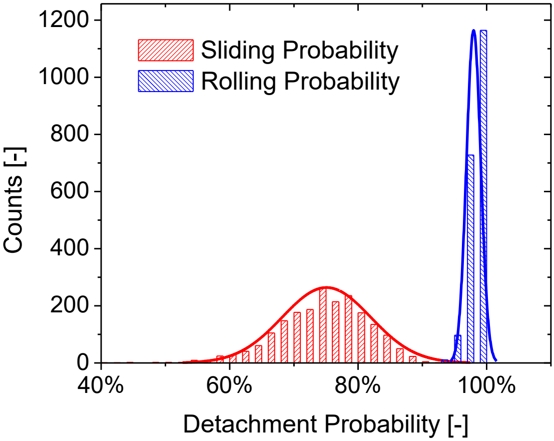

Fig. 3.14 PDF of the instantaneous sliding and rolling probability over a time period of 7 s (Re = 200, I = 9.0%, coverage degree = 50%, $D_{drug}/D_{carrier}$ = 5/100, surface treatment: TC 8h).

From those data now it is possible to perform the statistical analysis as shown in Fig. 3.14. The PDF of sliding fraction can be closely represented by a normal distribution function, while the rolling fraction is approaching 100%. Comparing to the laminar flow (Fig. 3.4 and Fig. 3.10), at *I* = 9.0%, the sliding probability was increased from 22% to 75% and the rolling probability was increased from 59% to 98%. The sliding and rolling detachment become much easier with the help of turbulent. Unfortunately, the turbulent simulations we have done so far are not sufficient to identify the relationship between the turbulence intensity and the particle Reynolds number.

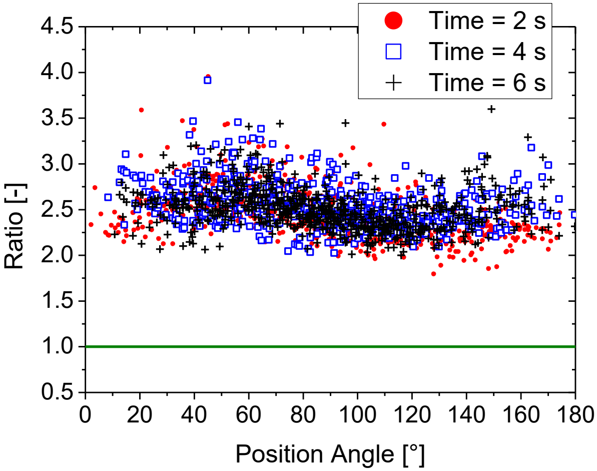

Fig. 3.15 Data points of *Ratio* in turbulent flow as a function of position angle for different snapshots (Re = 200, *I* = 9.0%, coverage degree = 50%, $D_{drug}/D_{carrier}$ = 5/100, surface treatment: TC 8h).

Fig. 3.15 shows the data points of *Ratio* (Eq. 3.10) for a Reynolds number of 200 at three snapshots. The straight solid line indicates the critical value. Different from the finding in laminar flow (Fig. 3.12), the drug particles which can be detached by both sliding and rolling locate over the whole range of position angle, since the sliding and rolling detachment become much easier with the help of turbulent. Moreover, all the data are larger than one, and this indicates the rolling will occurs earlier than sliding in accordance with the finding in the laminar flow.

3.2 Rough Wall Detachment Model

3.2.1 Introduction

Referring to the particle roughness effect one may distinguish two cases: the first case the particle surface is rough and the force on the particle is studied for different roughness dimension. The other case is a smooth particle placed on a rough wall, where the force exerted on the particle is studied under various surface roughnesses.

In the considered situation, the carrier particle is covered with hundreds of drug particles, and only the carrier particle surface is modified to adjust the adhesion force (Zellnitz, et al., 2013). Therefore here it is tried to study the detachment of smooth drug particles from a rough carrier surface. The roughness size from a chemical surface treatment is less than 20 nm (Zellnitz, et al., 2013). It is rather small compared to the size of drug particle (3-5 µm). In this case the influence of the roughness on the fluid dynamic force should be negligibly small. However when the size of the roughness is comparable with the particle diameter, etc. mechanical treatment, the influence of the surface roughness becomes considerable. This effect is discussed in the following.

As aforementioned the size of carrier (100-500 µm) is much larger than the size of the drug (3-5 µm). It is therefore reasonable to simplify the surface of the carrier as a flat wall for sufficiently small drug particles. In general the roughness structure is irregular in shape as well as randomly spatial distributed. For simplicity some authors (Reeks, et al., 1988; Ziskind, et al., 1997; Guingo & Minier, 2008) simplify the roughness elements as hemispheres. Guingo & Minier (2008) assume that the particle resides on two hemispheres in their case C. This geometrical simplification is however apparently unrealistic, because in this case at least three hemispheres are required for the drug particle to reach a mechanically stable position (Ziskind, et al., 1997). Despite of this deficiency, the advantage of this prescription is that the flow is simplified to a single direction: across the alignment of the roughness element (two hemispheres). In the case of three hemispheres supporting one drug particle, various flow directions relative to the location of the three hemispheres, as well as the anisotropic distances between the roughness elements must be considered, making the situation much more complicated. Therefore we further adopt the idea of two roughness elements supporting one drug particle, but change the shape to semi-cylinder, in order to obtain a two-dimensional roughness. Moreover, we consider the influence of the adjacent roughness elements on the drug particle, because roughness eventually affects the flow. Therefore we add more roughness elements along the stream-wised direction, and set the distance between these semi-cylinders equal.

3.2.2 Detachment criterion

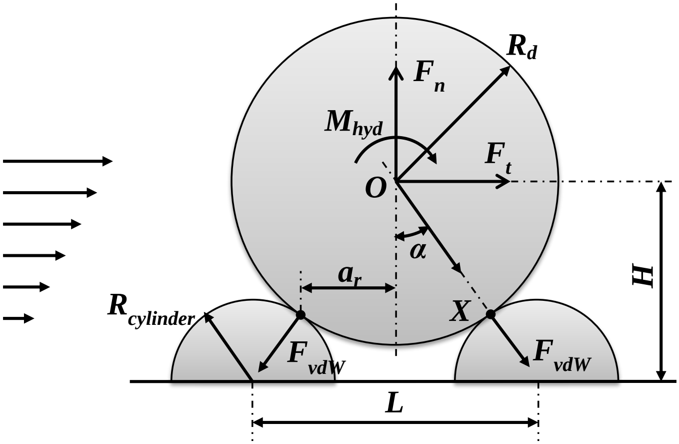

Fig. 3.16 Schematic diagram of a drug particle sitting on a rough wall.

Fig. 3.16 shows schematically the geometrical parameters. The drug particle resides on a pair of semi-cylinder bumps. The carrier roughness can be modified by changing the asperity distance, L, between two semi-cylinders and the size ratio, $R_{cylinder}/R_{drug}$. Both parameters affect the contact distance, a_r, which directly influences the detachment of drug particles. Only one drug particle is considered in the flow domain, i.e. the coverage degree is almost 0%, therefore the total force of the drug particle will be much higher than in the previous simulations presented in Section 2.4.2 (coverage degree ranges from 10% to 50%). In the case of multiple drug particles the analysis becomes substantially more complicated due to the generally random distribution of drug particles on a carrier.

Reeks et al. (1988) and Ziskind et al. (1997) studied the influence of rough surfaces on the particle detachment probability analytically. In Ziskind's study, the roughness was characterized by the asperity radius, $R_{asperity}$, and the distance between the asperities, L. Ziskind and Reeks assumed $R_{particle} >> R_{asperity}$, consequently the adhesion force can be calculated with $R_{asperity}$ instead of $R_{particle}$ (since the asperity plays the role of a small particle and the particle itself plays the role of a flat surface) and $L = 2a_r$ in their case. Moreover, only the contact distance, a_r, was considered for the momentum balance in their papers whereas the contact radius of the drug particle, a_d (Eq. 3.6), was ignored. Our simulation results, together with the experimental data in Table 3.2, show that the ratio of a_d / a_r is in a range of 8% - 13.3%. Therefore, the impact of contact radius, a_d, on the moment balance can be neglected in our cases, in accordance with the assumption of Ziskind (1997) and Reeks (1988).

Because the lift-off detachment criterion is the same as plane wall detachment model (Eq. 3.1), no extra discussion is necessary. Therefore only the sliding and the rolling detachment models are introduced in this section. As shown in Fig. 3.16, there are two contact points of the drug particle on the simplified rough surface. Consequently the total van der Waals force is twice as the experimentally measured value. On account of symmetry the analysis of the sliding and rolling detachment are conducted on only one of the two contact points. Point X (Fig. 3.16) is chosen to be the location of the detachment for both the sliding and rolling cases. Similar to Eq. 3.2 and 3.3, the sliding criterion can be expressed by:

$$F_n \sin\alpha + F_t \cos\alpha > \mu_d \cdot P \qquad 3.11$$

where μ_d is the static friction coefficient between the drug and carrier surfaces. P is the extra load and is given by:

$$P = -F_n \cos\alpha + F_t \sin\alpha + F_{vdW} \tag{3.12}$$

The rolling criterion can be expressed by:

$$M_{hyd} + R_d F_t \cos\alpha + a_r F_n > 2a_r F_{vdW} \cos\alpha \tag{3.13}$$

The hydrodynamic moment M_{hyd} about the drug particle centre of mass is directly obtained from the LBM simulations. The analytical solution of M_{hyd} is given by Hubbe (1984) provided in Eq. 3.5 under the condition that the particle experiences the linear shear flow and the particle Reynolds number is very small. In the considered situation, the flow becomes more complex. In order to have an easier comparison, a parameter named the hydrodynamic torque coefficient (*htc*) is defined as:

$$htc = \frac{M_{hyd}}{F_t R_d} \tag{3.14}$$

From Hubbe’s analytical solution one obtains $htc = 0.37$. The left side of Eq. 3.13 is the hydrodynamic torque around the detachment point X whereas the right side indicates the adhesion torque. Furthermore, the sliding ratio and the rolling ratio are defined as the left part divided by the right part of Eq. 3.11 and 3.13, respectively. The sliding detachment, or the rolling detachment, takes place when the sliding ratio, or the rolling ratio, is larger than one.

3.2.3 Simulation setup

The properties of the surface roughness, namely the asperity distance and the size ratio of $R_{cylinder}/R_{drug}$ are varied in the LBM simulation. For a certain surface roughness also the particle Reynolds number was varied for a systematic parameter study. As aforementioned, the surface of the carrier particle is taken as flat, and therefore the characteristic Reynolds number is defined with the diameter of the drug, denoted as Re_{drug}, and is given by:

$$Re_{drug} = \frac{\rho D_{drug} U_0}{\mu} \tag{3.15}$$

where U_0 is the free stream velocity. For the most popular size ratio of 5 µm/100 µm, the carrier Reynolds number ($Re_{carrier}$) which is used in the previous simulations is 20 times larger than the drug Reynolds number (Re_{drug}) as used in this chapter.

In the simulation one parameter, either the asperity distance or the size ratio, is varied while the other one remains constant. Since the contact distance is the only geometry parameter important for the detachment criterion (Eq. 3.13), the contact distance instead of the asperity distance is chosen for the quantitative analysis. The relation between the asperity distance and the contact distance is given by:

$$a_r = \sqrt{R_{drug}^2 - \left(\frac{R_{drug} H}{R_{drug} + R_{cylinder}} \right)^2} \tag{3.16}$$

where H is the height of the drug particle. When $R_{drug} >> R_{cylinder}$, the above two equations are simplified to $L = 2a_r$ in accordance to Reeks et al. (1988) and Ziskind et al. (1997). These equations are applicable for both the two-semi-cylinder and the two-hemisphere structure of the surface roughness. Throughout the thesis the size ratio is varied by changing the size of the semi-cylinder size while keeping the drug size constant.

Fig. 3.17 displays the relationship between the contact distance, the asperity distance, the size ratio and the particle height. For a fixed size ratio (Fig. 3.17a and b) the height of the particle decreases while the asperity distance linearly increases with the contact distance. For a fixed asperity distance (Fig. 3.17c and d) both of the height and size ratio decrease while increasing the contact distance.

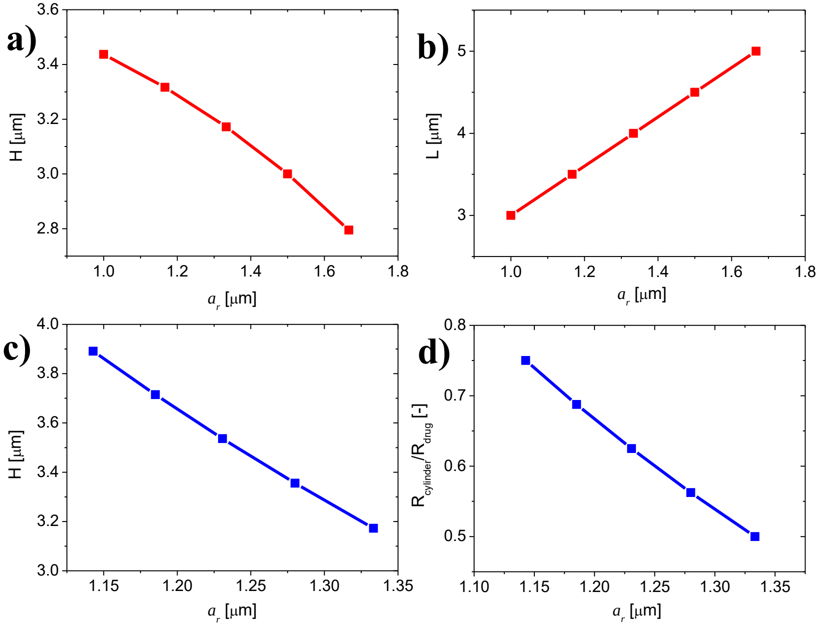

Fig. 3.17 The relationship between the contact distance and the asperity distance, the size ratio and the particle height. a) and b): size ratio fixed, c) and d): asperity distance fixed, R_{drug} = 2.5 µm for all cases.

For the flow simulations, the drug particle was fixed in a rectangular flow domain illustrated in Fig. 3.18 and exposed to different kinds of flow situations. The boundary condition of the wall, including both the semi-cylinder surface and the flat wall part, is assigned as no-slip condition. The velocity profile of the inlet boundary at the left side of the flow domain is set as a plug flow. A shear flow develops downstream due to the no-slip boundary condition of the surface. At the outlet a gradient free condition is applied and at all the other side faces symmetry boundary conditions are being used (Fig. 3.18). For the rough wall calculations a very small gap of $0.002 \cdot D_{drug}$ was used between the drug and the wall to prevent that one solid node belongs to two different objects.

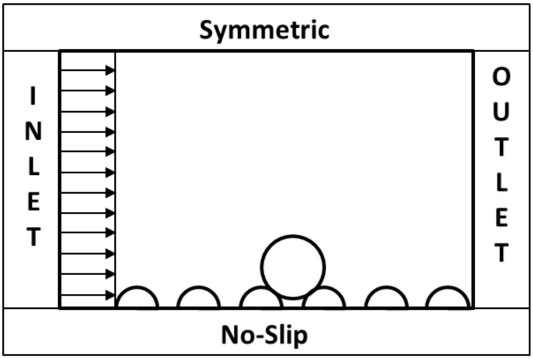

Fig. 3.18 Computational domain with applied boundary conditions for the rough wall simulation.

The selection of the size of the computational domain was based on an extensive parameter study (Fig. 3.19) for optimizing accuracy and computational effort. For each case the particles were resolved by 40 grid cells (10 base grids) of the finest mesh by using three grid refinement levels. The variation of the domain size in stream-wise direction (x/D_d) for fixed dimensions in the lateral and vertical direction ($y/D_d = 10$, $z/D_d = 12$) reveals that 14 particle diameters are sufficient to obtain coefficients which are independent of the dimension (Fig. 3.19a). Moreover, the vertical dimension of the domain was varied by fixing the stream-wise and the lateral domain size ($x/D_d = 10$, $y/D_d = 10$). The results show (Fig. 3.19c) that a vertical dimension of 14 particle diameters should be sufficient. As a result of this study all the calculations for this test case were done for a domain size of $x/D_d = 14$, $y/D_d = 10$, $z/D_d = 14$. The drag and lift coefficients in Fig. 3.19 are defined as:

$$C_D = \frac{F_D}{\frac{\rho}{2} U_0^2 \frac{\pi}{4} D_{drug}^2}, C_L = \frac{F_L}{\frac{\rho}{2} U_0^2 \frac{\pi}{4} D_{drug}^2} \qquad 3.17$$

where F_D and F_L are the drag and lift forces of the drug particle. Fig. 3.20 offers an overview of the mesh of the fluid domain, the total number of grid nodes was 7,214,680.

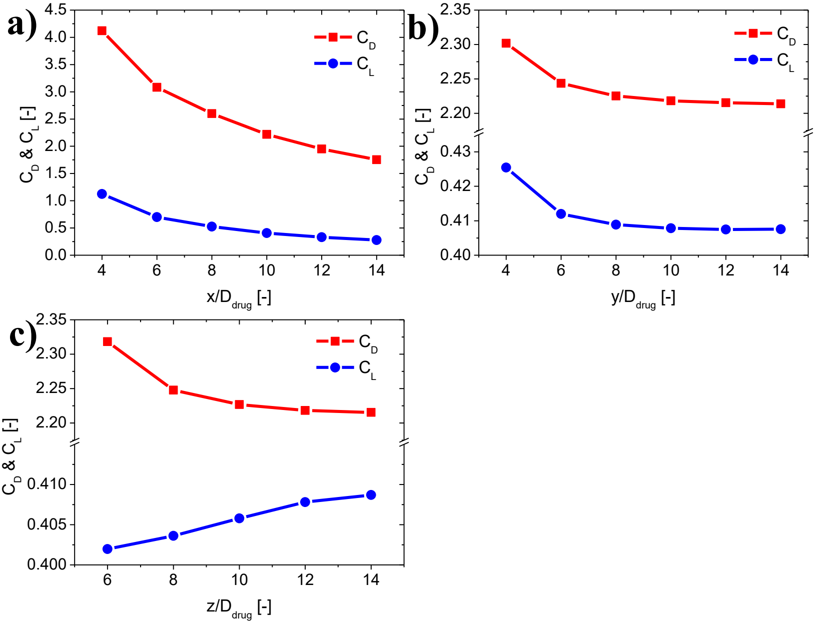

Fig. 3.19 Simulated drag and lift coefficients of the drug particle with increasing domain size in stream-wise (a), the lateral (b) and the vertical (c) directions (Re = 10, $R_{cylinder}/R_{drug}$ = 1.25 μm/2.5 μm, L = 4 μm, initial domain size: $x/D_d = y/D_d = 10$, $z/D_d = 12$). The definition of drag and lift coefficients are based on the inlet velocity and the particle diameter.

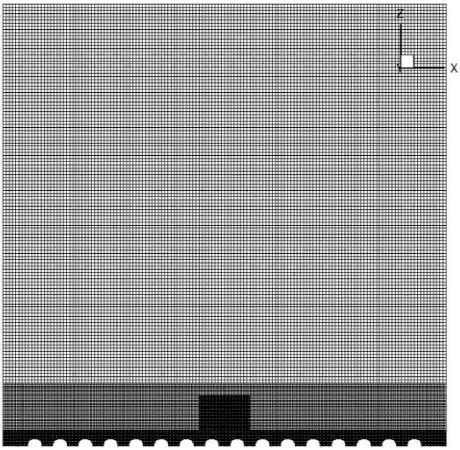

Fig. 3.20 Mesh of the fluid domain for rough wall simulations; resolution: 40 grids cells of the finest mesh per particle diameter with three-level grid refinements; domain size: x/D_d = 14, y/D_d = 10, z/D_d = 14.

3.2.4 Results analysis

Fig. 3.21 shows the velocity contours for different roughness structures in the wall induced shear flow. Case b and d investigate the influence of the asperity distance while keeping the size ratio constant. Case b and c examine the influence of the size ratio with a fixed asperity distance. For the purpose of comparison, Case a is equipped with a smooth surface, while the particle remains at the same location as in Case b, c and d in the x- (left to right) and y- (front to back) directions. It should be noted that the drug particle has contact with the rough elements in Case b, c and d, while in Case a the particle has close contact with the plane wall. This particular setting allows Case a and b to explore the influence of the roughness structure. Since the x-velocity, in the direction from left to right, dominates the other two velocity components, only the magnitude of the x-velocity is displayed, and the displayed range remains the same in all Figures. It shows that the rough wall increases the velocity magnitude.

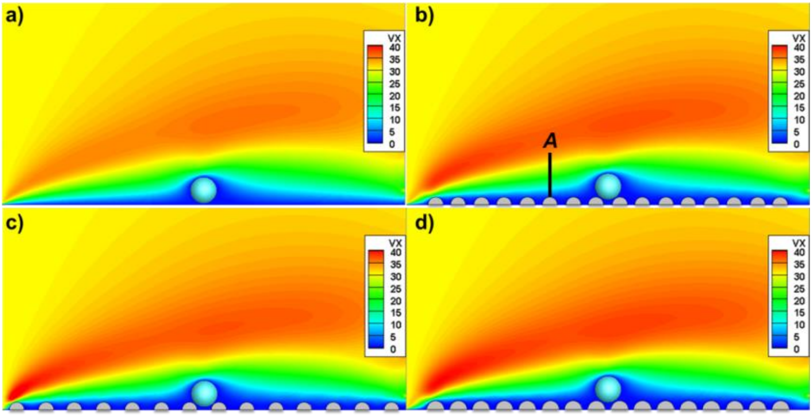

Fig. 3.21 The wall induced shear flow around one particle residing on different roughness structures. a): the particle attach to a plane wall. b) and c): rough elements with the same asperity distance but varying size ratios. b) and d): rough elements with the same size ratio but varying asperity distances. Re = 10 for all cases.

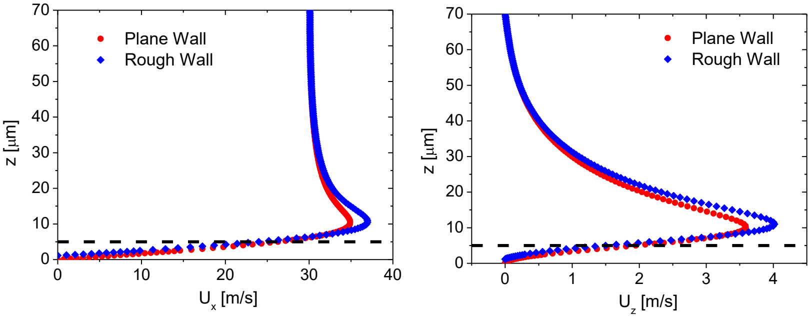

Fig. 3.22 Velocity profiles of the fluid nodes on the line *A* in Fig. 3.21. ‘Rough wall’ corresponds to Case b, and ‘Plane wall’ corresponds to Case a in Fig. 3.21. The straight dashed line indicates the height of particle. Re = 10 for both cases.

Quantitatively, the increase of the velocity magnitude by the existence of the roughness element is exemplarily revealed by the velocity profile along the line *A* in Fig. 3.21b. In order to avoid the influence of the inlet as well as the drug particle on the flow, the location of line *A* is chosen to be at $x = x_{center} - 2.5L$, thus in the middle of the 3rd semi-cylinder ahead of the particle, and at $y = y_{center}$ in the symmetry plane (x_{center} and y_{center} refer to the middle position of the *xy*-plane). The inlet velocity of the fluid domain is set as $U_x = 30\ m/s$, $U_y = U_z = 0\ m/s$ ($Re = 10$). The height of the domain along the z-axis is 70 µm ($14D_d$). Only Case a and b in Fig. 3.21 are considered for a comparison. Fig. 3.22 plots the profiles of the velocity components U_x and U_z in the vertical direction, respectively. And the straight dashed line indicates the height of particle. Far away from the particle, the velocity profiles conform to the inlet boundary condition. The flow near the bottom wall is affected by the no-slip boundary condition, i.e. increases linearly as the height. The existence of the drug particle diminishes the area of the cross section of the flow, thus a velocity increase is seen approximately at the height of 10 µm ($2D_d$). The velocity increase is further enhanced by the existence of the roughness element. The comparison of the velocities at the height of 10 µm reveals that, U_x is increased by 5.7% and U_z is increased by 9.9% though the roughness elements.

The critical parameter *htc* is calculated at different flow conditions. In the LBM simulation, the value of the *htc* fluctuates at a certain flow condition as the computation converged. An average of 10,000 iterations is made at the end of simulation. Fig. 3.23 and Fig. 3.24 show the numerical results. In Fig. 3.23, Hubbe's analytical solution of $htc = 0.37$ is displayed as a straight solid line, under the assumptions of linear shear flow, very small particle size and very small Reynolds number (i.e. $Re << 1$). The squares signify the results from Section 2.2, where the particle has direct contact with the wall and experiences the linear shear flow with a range of particle Reynolds numbers. The circles and triangles refer to the 'plane wall' and the 'rough wall' in Fig. 3.22 Case a and b, respectively. At small particle Reynolds numbers, our simulation results for the linear shear flow are around 0.334, exhibiting a small discrepancy from Hubbe's 0.37. The numerical results show that the *htc* value has a linear decrease with rising particle Reynolds numbers. For higher Reynolds numbers a wake is developed near the back stagnation point of the particle (Fig. 2.14), which reduces the drag coefficient.

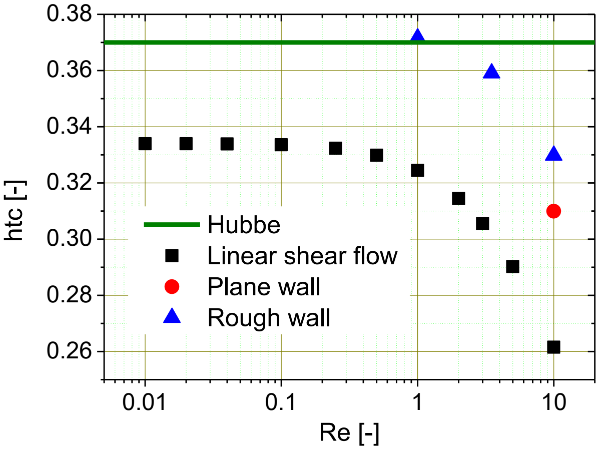

Fig. 3.23 The hydro-torque-coefficient as a function of the particle Reynolds number under various shear flow conditions. The straight solid line denotes the analytical result by Hubbe (1984). The square denotes the linear shear flow and the particle has close contact with the wall (Section 2.2). The circle denotes the wall induced shear flow where the particle has close contact with the wall (Fig. 3.21a). The triangle denotes the wall induced shear flow with a rough wall (Fig. 3.21b) ($R_{cylinder}/R_{drug}$ = 1.25 µm/2.5 µm, *L* = 4 µm).

Comparing the linear shear flow (square) with the wall induced shear flow (cycle) at Re = 10, the value of the *htc* increases considerably. One reason could lie in the difference of the definition of the particle Reynolds number (Eq. 2.13 & 3.15). In the linear shear flow, the flow velocity field is prescribed, so that the flow velocity at the particle centre is known, and the particle Reynolds number is easily determined with this value. In the wall induced shear flow, the most proper way to define the particle Reynolds number is to take the inlet velocity. Therefore the local particle Reynolds number should be smaller than this definition. After adding the roughness elements to the plane wall (triangle), the *htc* increased from 0.31 to 0.33. The main reason is that the height of the particle is increased from 2.5 µm to 3.17 µm by the rough elements, and then the particle encounters much larger effective flow velocity (Fig. 3.22). Another reason could be the rough structure covers part of the particle's contour at the lower half, and thus induces a greater asymmetry of the flow over the drug particle.

Fig. 3.24 exhibits the *htc* for different rough structures under the wall induced shear flow. In order to facilitate a clear comparison, the asperity distance, *L*, and the size ratio, $R_{cylinder}/R_{drug}$, are transformed into the contact distance, a_r, by Eq. 3.16. The data points are therefore clustered into two groups. The squares signify the data collected by changing the contact distance with the variation in asperity distance, while the triangles show data points collected by changing the contact distance by the variation in the size ratio. Additionally, data points at a lower Reynolds number of 3.5 with the contact distance changing by the asperity ratio are also exhibited.

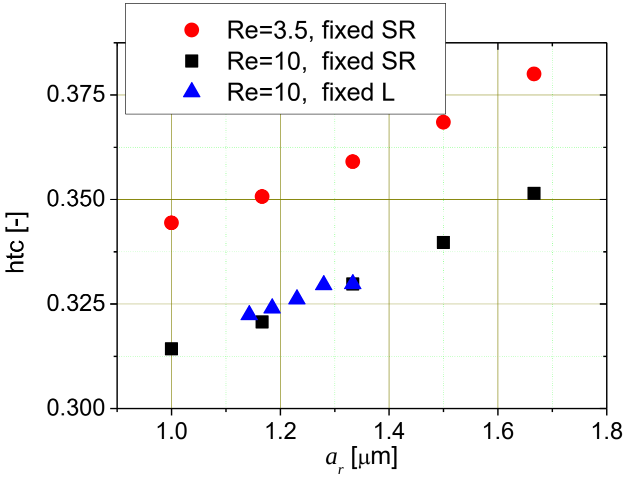

Fig. 3.24 The hydro-torque-coefficient for different rough structures as a function of the contact distance under the wall induced shear flow. Square: varying the asperity distance with fixed size ratio (Fig. 3.21 Case b and d) (Re = 10, $R_{cylinder}/R_{drug}$ = 1.25 µm/2.5 µm).

Triangle: varying the size ratio with fixed asperity distance (Fig. 3.21 Case b and c) (Re = 10, R_{drug} = 2.5 μm, L = 4 μm). Cycle: varying the asperity distance with fixed size ratio (Fig. 3.21 Case b and d) (Re = 3.5, $R_{cylinder}/R_{drug}$ = 1.25 μm/2.5 μm).

The *htc* increases with the rising contact distance for all three curves as shown by Fig. 3.24. The reason is the following. As the contact distance increases, the height of the particle decreases, as shown in Fig. 3.17 Case a and c. Further, the decrease of the height of the particle leads to an effective reduction of the particle Reynolds number as shown in Fig. 3.22. As a result the value of the *htc* increases, as shown in Fig. 3.23. The observed overlapping of the triangles and the square show that the contact distance is the influencing factor for *htc*. The comparison of the two Reynolds numbers, 3.5 and 10, show an agreement with the finding of Fig. 3.23.

Fig. 3.25 reports the drag coefficient and the lift coefficient of the particles as a function of the contact distance. Case a and b investigate the influence of the asperity distance while keeping the size ratio constant. Case c and d examine the influence of the size ratio with a fixed asperity distance. The straight solid lines indicate the drag and lift coefficients in the case of the plane wall (Fig. 3.21a), and its drag and lift coefficients are constant for a fixed particle Reynolds number (see Eq. 3.15 and 3.17). The difference of drag and lift coefficients between the plane and rough wall simulation results is as a result of two conflicting factors. On the one hand, the effective velocity experienced by the particle is enhanced by the existence of the roughness elements (see Fig. 3.22), and then it increases the drag and lift forces. On the other hand, the area of the cross section becomes smaller because part of the particle surface is in the shadow of the roughness elements; therefore the drag and lift forces of the particle become smaller. The ultimate consequence is that the drag and lift coefficients could be either raised or minimized by the addition of the roughness elements. When increasing the contact distance, both the drag and lift coefficients show a decreasing tendency. The main reason is that the height of the drug is decreased (Fig. 3.17a and c) which yields the reduction of effective velocity experienced by the particle.

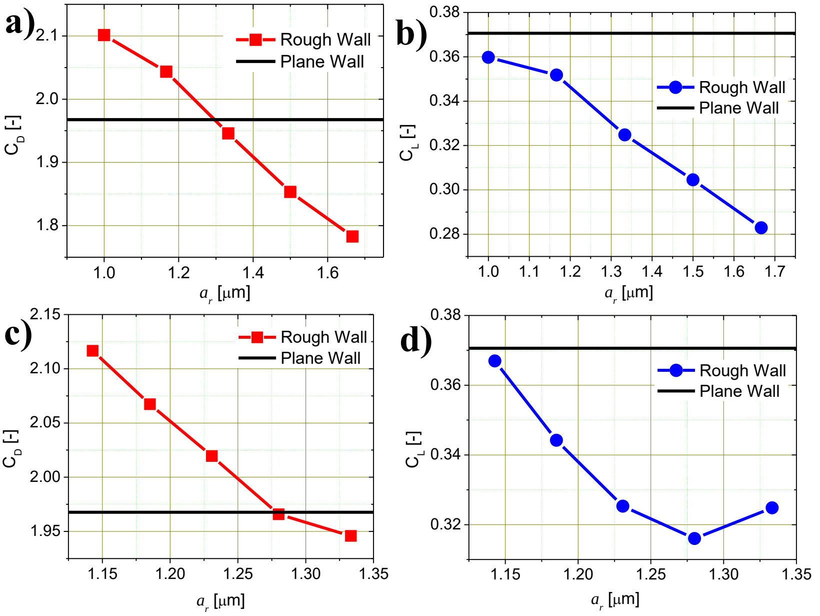

Fig. 3.25 Drag and lift coefficients of the particle as a function of the contact distance for different rough structures. a) and b): the roughness varies in asperity distance with a fixed size ratio ($Re = 10$, $R_{cylinder}/R_{drug} = 1.25$ µm/2.5 µm), c) and d): the roughness varies in size ratio with a fixed asperity distance ($Re = 10$, $R_{drug} = 2.5$ µm, $L = 4$ µm). The definition of drag and lift coefficients are based on the inlet velocity and the particle diameter.

Fig. 3.26 shows the rolling and sliding ratios of the drug particle exposed to wall induced shear flow as a function of the contact distance with a fixed size ratio. The rolling and sliding ratios encounter approximately a linear decrease while increasing the contact distance, which makes the detachment more difficult. This is due to the reduction of the drag and lift coefficients while increasing the contact distance (Fig. 3.25 Case a and b). When the particle Reynolds number grows from 3.5 to 10, rolling and sliding ratios both increase, on account of the increase of the fluid dynamic force. As shown in Fig. 3.26, only sliding detachment occurs at Re = 10.

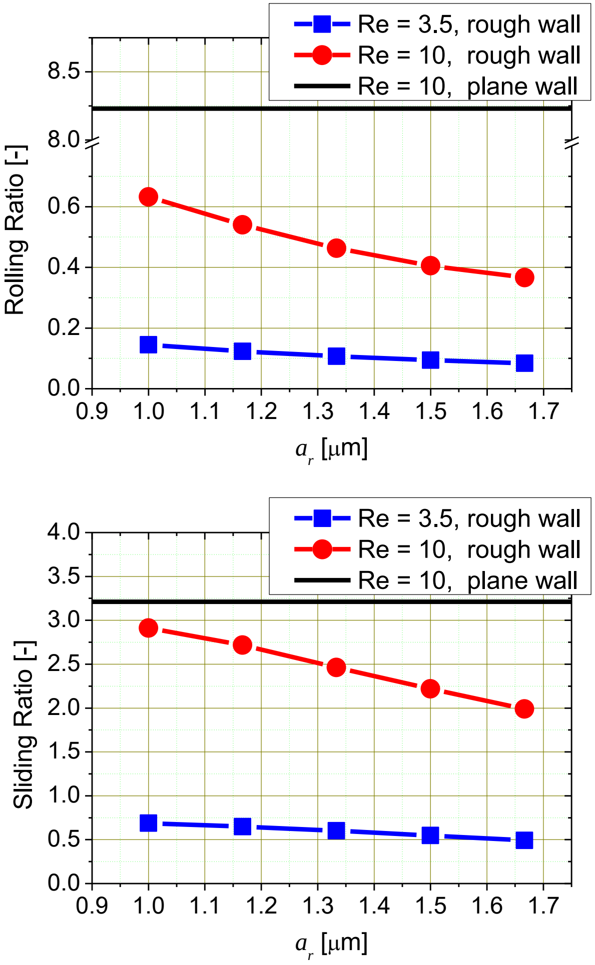

Fig. 3.26 Rolling and sliding ratios of the drug particle as a function of the contact distance with a fixed size ratio ($R_{cylinder}/R_{drug}$ = 1.25 μm/2.5 μm, surface treatment: TC 8h).

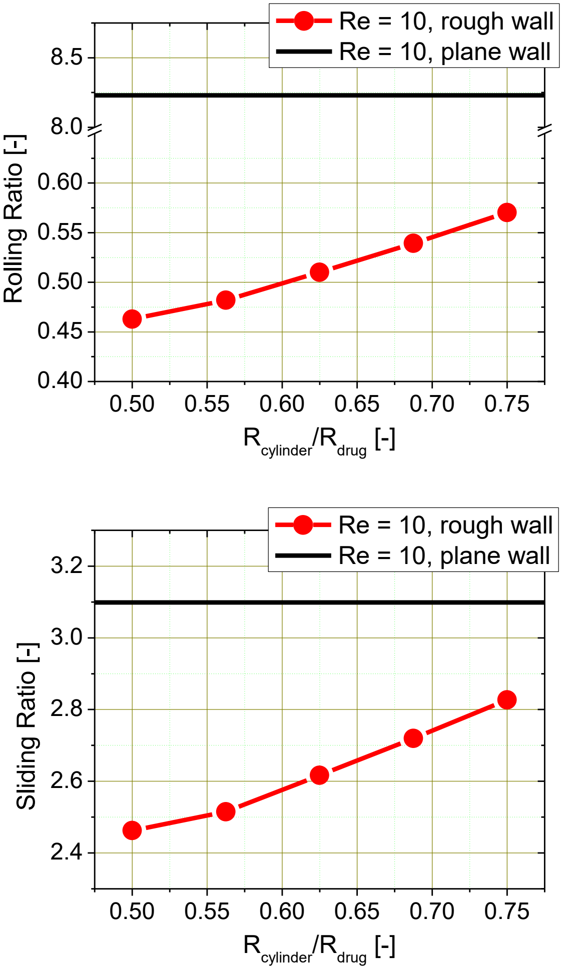

Fig. 3.27 Rolling and sliding ratios of the particle as a function of the size ratio with a fixed asperity distance (L = 4 μm, R_{drug} = 2.5 μm, Re = 10, surface treatment: TC 8h).

Fig. 3.27 shows rolling and sliding ratios as a function of the size ratio with a fixed asperity distance under the wall induced shear flow. Rolling and sliding ratios exhibit nearly a linear increase while the size ratio increases, which leads to an easier detachment. The reason is given by Fig. 3.17 Case c and d. The increasing size ratio results in a decreasing contact distance. Further this leads to the increase of the height of drug particle, and therefore the particle encounters larger drag and lift forces as shown in Fig. 3.25. As indicated by Fig. 3.27, rolling detachment is not likely to occur, whereas sliding detachment happens for a wider range. The straight solid lines in Fig. 3.26 and Fig. 3.27 are rolling and sliding ratios of the plane wall. The value of sliding ratio of the plane wall is 3.21 and is a little higher than the rough wall results. The value of rolling ratio of the plane wall is 8.23, which is much larger than the value of the rough wall.

As discussed in section 3.1.5, the rolling detachment always occurs earlier than the sliding detachment in the plane wall detachment model. In the rough wall detachment model, go back to Eq. 3.11 to 3.13, from which yielding a non-dimensional ratio:

$$Ratio = \frac{\left(M_{hyd} + R_d F_t \cos\alpha + a_r F_n\right) / \left(2a_r \cos\alpha\right)}{\left(F_n\left(\sin\alpha + \mu_d \cos\alpha\right) + F_t\left(\cos\alpha - \mu_d \sin\alpha\right)\right) / \mu_d} \qquad 3.18$$

If the variable *Ratio* is larger than one, the rolling detachment occurs first; if *Ratio* is smaller than one, the sliding detachment occurs first on the contrary. By applying the precondition in Table 3.1 and Table 3.2, it is possible to calculate the value of *Ratio* for different roughness structures. Fig. 3.28 gives an overview of *Ratio* for two different particle Reynolds numbers with a fixed size ratio. The straight solid line indicates the critical value. It is obvious that all values of *Ratio* are smaller than one. The reason is that the contact distance is introduced into the rolling detachment criterion for the rough wall which increases the adhesion torque significantly (Eq. 3.13 right). Therefore, the particle encounters much larger torque resistance in the rough wall detachment model compared to the plane wall detachment model (Eq. 3.4). As a result sliding detachment is easier than rolling detachment in the frame of the rough wall detachment model.

In conclusion the rough structures decrease remarkably the probability of rolling and sliding detachment. It should be emphasized that the above rolling and sliding detachment studies use the same adhesion forces (TC 8h). However, in experiment the increase of roughness reduced the adhesion force. This phenomenon is not considered in the present study.

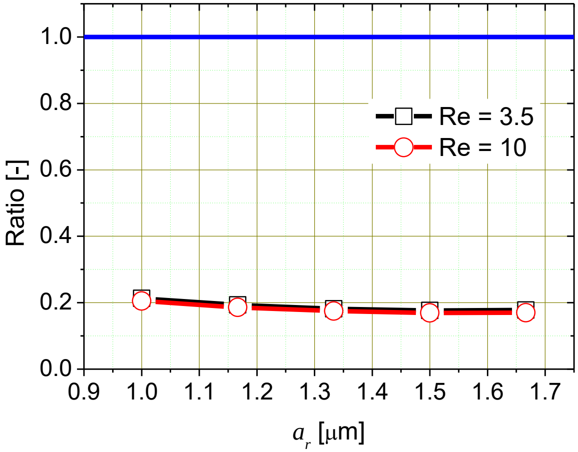

Fig. 3.28 *Ratio* as a function of the contact distance with a fixed size ratio for two particle Reynolds numbers ($R_{cylinder}/R_{drug}$ = 1.25 μm/2.5 μm, surface treatment: TC 8h).

4 Wall Collision Detachment Model

Based on the macro scale simulation of the internal flow field of the inhaler and the accompanied particle trajectory by the OpenFOAM program, high rates of cluster-wall collision were found inside the swirl chamber (Fig. 1.3). When a carrier particle collides with the wall, the inertia force is exerted on the drug particles which reside on the carrier surface. The detachment of the drug particles may happen when the maximum inertia force is larger than a certain level.

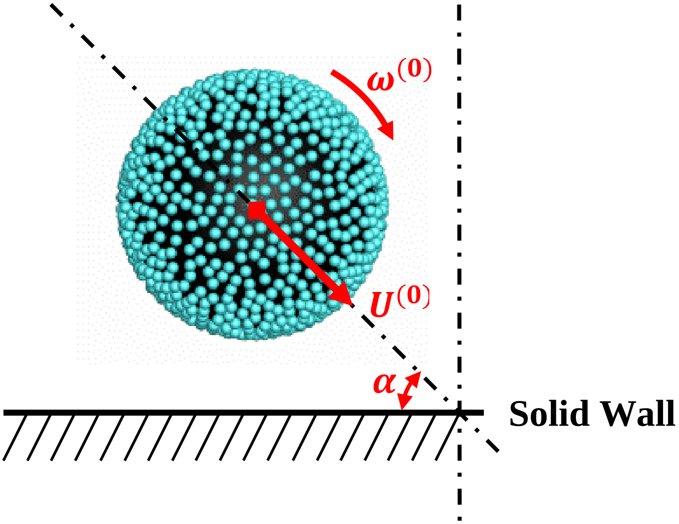

Fig. 4.1 Collision of a particle cluster to the solid wall (coverage degree = 50%, $D_{drug}/D_{carrier} = 5/100$).

Fig. 4.1 illustrates a typical collision of the particle cluster with the solid wall. The carrier particle, covered by hundreds of drug particles, collides on the wall with an initial translational velocity, $U^{(0)}$, an initial angular velocity, $\omega^{(0)}$, and a certain impact angle, α, measured from the plane solid surface. There are two basic collision processes: either the carrier particle surface hits the wall; or the drug particles on the carrier will do so. When the drug particle collides onto the wall first, there exist two deformations. One is in between the colliding drug particle and the wall, and one is in between the colliding drug particle and carrier particle. The deformation between the colliding drug particle and carrier particle cannot be fully developed, since the carrier will slide or roll even at very small deformation. The carrier will be detached from the colliding drug particle and then collides onto the wall again with another impact angle. Therefore, only the situation which the carrier collides with the wall is considered in this chapter.

In the collision study the following four assumptions are taken to simplify the collision process:

I. Vacuum, i.e. particles are very inertial that fluid forces can be neglected;
II. Isotropic and homogeneous particle body;
III. Elastic deformation of carrier and drug particles;
IV. The wall is a rigid body;

The first assumption is reasonable because it will be shown later in this section that the fluid dynamic force is much smaller compared to the inertia force. Assumption II is a common simplification regarding the material property. Assumption III and IV are widely adopted in the theory and application of Hertz contacts so that the conversion formulas of geometry and elasticity are well established (Al-Bender & Moerlooze, 2008).

The collision of a particle onto a rigid solid wall can be divided into two phases: compression phase and recovery phase (Fig. 4.2). Before collision, the particle moves with an initial translational velocity, $U^{(0)}$, which can be normalised on the *xy*-plane, and an initial angular velocity, $\omega_z^{(0)}$, around the z-axis. The rotation around the *x* and *y* axis are not interested since they have no influence on the force. However, the method to evaluate the reduction of ω_x and ω_y during the collision process will be provided either. In the compression phase, the initial kinetic energy of the particle is partly transformed into elastic potential energy. In the recovery phase, the elastic potential energy is transformed back to the kinetic energy. The Coulomb's law of friction is assumed to hold for a sliding collision. The change of the particles translational and rotational velocities during the bouncing process can be calculated from the momentum equations of classical mechanics (Crowe, et al., 2012; Sommerfeld, et al., 2008). Depending on the period during which the particle slides along the wall, the formulation is separated into the following three cases:

Case I: the particle stops sliding in the compression period.
Case II: the particle stops sliding in the recovery period.
Case III: the particle continues to slide throughout the compression and recovery phases.

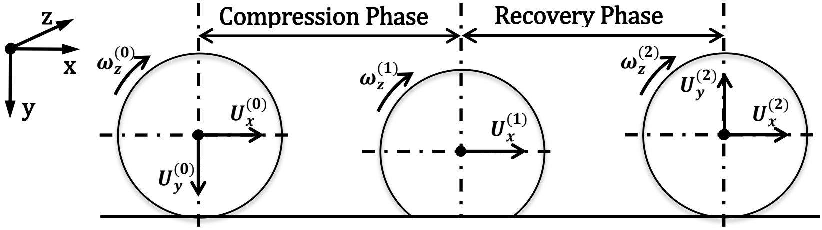

Fig. 4.2 The compression and recovery phases of the particle-wall collision.

A detailed explanation for each case will be given after the introduction of the forces on particles.

4.1 Theory formulation

4.1.1 Force on particles

As shown in Fig. 4.3 left, the carrier particle together with the attached drug particles moves with an initial translational velocity, $U^{(0)}$, on the *xy*-plane, an initial angular velocity, $\omega_z^{(0)}$, around the *z*-axis and approaches the wall with a certain impact angle, α. In the compression phase, the carrier is deformed by the amount y (i.e. y is the temporally varying deformation), which induces the normal force (or resistance force), F_N, on the carrier particle as shown in Fig. 4.3 right. During the compression process, the carrier can slides and rolls on the wall. The tangential velocity component (x-direction) of $U^{(0)}$, $U^{(0)}cos\alpha$, is reduced by the friction force, F_f. By Coulomb's law of friction, $F_f = \mu_w F_N$, where μ_w is the friction coefficient between the colliding particle and the wall. The gravities of the carrier and drugs are rather small comparing to their inertia force and thus are ignored.

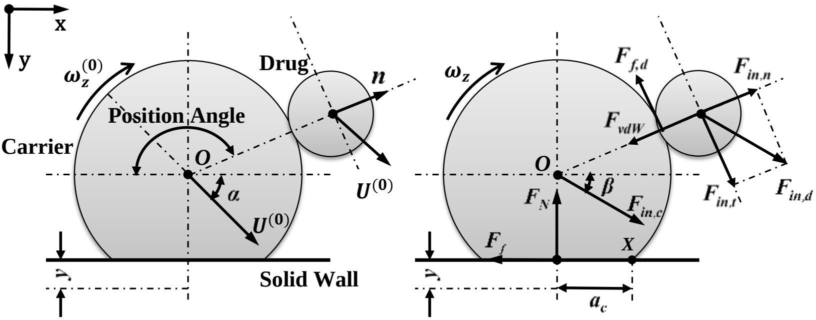

Fig. 4.3 Schematic diagram of a compressed elastic carrier particle with one drug particle attached; left: velocity vectors; right: force vectors.

As shown in Fig. 4.3 right, the inertia force of the carrier, $F_{in,c}$, is introduced to recover Newton's second law in the non-inertial reference frame. The relationships between the normal force, the friction force and the inertia force are given by:

$$\begin{aligned}&\text{x-direction: } \boldsymbol{F_f} = m_c \boldsymbol{a_x},\ \boldsymbol{F_{in,c,x}} = -m_c \boldsymbol{a_x}\\ &\text{y-direction: } \boldsymbol{F_N} = m_c \boldsymbol{a_y},\ \boldsymbol{F_{in,c,y}} = -m_c \boldsymbol{a_y}\end{aligned} \tag{4.1}$$

where $F_{in,c,x} = F_{in,c}\,cos\beta$ and $F_{in,c,y} = F_{in,c}\,sin\beta$ are the tangential and normal components of the inertia force of the carrier with mass m_c. If the drug particles are not detached during the compression phase, the inertia force on the drug particles, $F_{in,d}$, is:

$$\boldsymbol{F_{in,d,x}} = -m_d \boldsymbol{a_x},\ \boldsymbol{F_{in,d,y}} = -m_d \boldsymbol{a_y} \tag{4.2}$$

where m_d is the mass of the drug. If all drugs keep the same size, the inertia forces, $F_{in,d}$, on all drug particles as well as their components have the same value, and preserve the same direction as the inertia force of the carrier particle, $F_{in,c}$. The drug inertia force can be separated into a normal ($F_{in,n}$) and a tangential ($F_{in,t}$) component as shown in Fig. 4.3 right. The normal inertia force is balanced by the van der Waals force (F_{vdW}) which yields a potential lift-off detachment. The tangential inertia force is always a positive value and is balanced by the friction force of the drug particle ($F_{f,d}$). The normal and tangential components of the drug inertia force are essential for the detachment study and can be expressed by:

$$F_{in,n} = \frac{\boldsymbol{F_{in,d}} \cdot \boldsymbol{n}}{|\boldsymbol{n}|}, F_{in,t} = \sqrt{F_{in,d}^2 - F_{in,n}^2} \tag{4.3}$$

where $\boldsymbol{n}$ is the position vector and indicates the location of a drug particle. Although all drugs share the same inertia force, the normal and tangential inertia forces on each drug particle are different depending on their locations. The solution of the normal force, F_N, was given by Landau and Lifshitz (1986) for small deformations of two elastic solid particles as:

$$F_N(y) = \left[D^2 \left(\frac{1}{R_1} + \frac{1}{R_2} \right) \right]^{-0.5} \cdot y^{1.5} \tag{4.4}$$

$$D = \frac{3}{4} \left(\frac{1-\sigma_1^2}{E_1} + \frac{1-\sigma_2^2}{E_2} \right) \tag{4.5}$$

where σ_1, σ_2 and E_1, E_2 are the Poisson's ratio and the Young's modulus of two particles, and R_1, R_2 are the radii of two particles. Since the wall is assumed as a planar rigid body (Assumption IV), the wall's Young's modulus, E_1, becomes infinity and its Poisson's ratio, σ_1, is damped to zero. Hence Eq. 4.4 is simplified to:

$$F_N(y) = \frac{4E_c\sqrt{R_c}}{3\left(1-\sigma_c^2\right)} \cdot y^{1.5} \tag{4.6}$$

where σ_c, E_c and Rc are the Poisson's ratio, the Young's modulus and the radius of the carrier particle. At the end of compression phase, the momentum of the carrier particle in y-direction is fully transformed into the elastic potential energy. From the energy balance we have:

$$\frac{1}{2}m_c\left(U^{(0)}\cdot sin\,\alpha\right)^2=\int_0^h F_N\left(y\right)\cdot dy \qquad 4.7$$

From Eq. 4.6 and 4.7, the maximal compression distance, h, can be written as:

$$h^{2.5}=\frac{15}{16}\cdot\frac{m_c\left(U^{(0)}\cdot sin\,\alpha\right)^2}{\sqrt{R_c}}\cdot\frac{1-\sigma_c^2}{E_c} \qquad 4.8$$

4.1.2 Case I

The symbols used for the translation velocities, angular velocities in Case I are shown in Table 4.1. The compression period in Case I is subdivided into sliding and non-sliding periods. The superscripts of (0), (s), (1) and (2) on velocities relate to the values at the end of the period. At the sliding period a friction force, F_f, acts on the carrier in the direction opposite to the motion of the carrier (Fig. 4.3). The torque of the carrier on the detachment point X is $T_X=F_{in,c,x}\left(R_c-y\right)\approx F_fR_c\neq 0$ which increases the rotation of the carrier. At this period, the translation and rotation of the carrier sphere occur simultaneously. The tangential velocity, U_x, is reduced by the friction force, F_f. Meanwhile the angular velocity, ω_z, starts from $\omega_z^{(0)}$ and is accelerated by the friction force. At the critical value, $U_x=\omega_zR_c$, the carrier thereafter rolls without slipping. At this moment the frictional force disappears, and the sphere begins the next period of its motion. At the non-sliding period, the rolling speed is decelerated by the torque of the rolling resistance. The friction force of these two periods can be expressed by:

$$\begin{aligned}&\text{Sliding: } F_f = \mu_w F_N \text{, when } U_x > \omega_z R_c\\ &\text{Non-sliding: } F_f = 0\text{, when } U_x = \omega_z R_c\end{aligned} \qquad 4.9$$

In the paper of Al-Bender & Moerlooze (2008), stage one is termed ‘Creepage’ and stage two is termed ‘Gross Rolling’. From the above equation we can easily obtain: $\mu_w = F_f / F_N = arctan\beta$.

Pre-collision	Compression period (1)		Recovery period (2)	Post-collision
	sliding period			
Trans. Velocity	$U^{(0)}$	$U^{(s)}$	$U^{(1)}$	$U^{(2)}$
Angular velocity	$\omega^{(0)}$	$\omega^{(s)}$	$\omega^{(1)}$	$\omega^{(2)}$

Table 4.1 Velocities for Case I.

Then it is needed to solve the translational and angular velocities in Table 4.1 for different periods. First the variable carrier velocity in y-direction, U_y, is solved in terms of the compression distance y. From Newton’s second law, $m_c\, dU_y / dt = -F_N$ one can obtain $m_c \frac{dU_y}{dy}\frac{dy}{dt} = -F_N$, then $m_c U_y dU_y = -F_N dy$. Now integrate on the both sides $\int_{U^{(0)} sin\alpha}^{U_y(y)} m_c U_y dU_y = -\int_0^y F_N dy$, finally U_y can be written as:

$$U_y(y) = U^{(0)} sin\alpha\sqrt{1-(y/h)^{2.5}} \qquad 4.10$$

After that, it is needed to calculate the relation between the compression time, t, and the compression distance, y. First write $U_y = dy/dt$, then $dt = U_y^{-1} dy$, integrate on the both sides: $\int_0^t dt = \int_0^y U_y^{-1} dy$, the result is in a form of hypergeometric functions which cannot be solved analytically. Here we calculate the time numerically by applying a constant increment Δy, the relationship between the time and compression distance at the N_{th} time steps can be expressed by:

$$y_N = A_{t=t_N} U^{(0)} \sin\alpha \cdot t_N \tag{4.11}$$

A is a mapping list for the compression distance, y, and time, t, for all time steps. The time for recovery phase is as same as the time for compression phase under Assumption III. If one wants to discretise the compression phase into *1000* time steps, the total elements of A will be *2000* (including the recovery phase) and the increment Δy for every time step is $0.001h$. The above equation builds a bridge between normal and tangential components. At the end of compression phase, $y = h$, the total time for compression, τ, is $y / (0.68\, U^{(0)} \sin\alpha)$.

The tangential velocity, U_x, for the sliding period is solved by accumulating the discretised values for every time steps as following:

$$U_x = U^{(0)} \cos\alpha + \sum_{i=0}^{i=N} \Delta U_{x,i} \tag{4.12}$$

The discretised tangential velocity, ΔU_x, at the N_{th} time step can be derived from Newton's second law, $m_c\, dU_x / dt = -F_f(t)$. Then separate the dU_x and dt onto each side of the equation and integrate on the both sides: $\int_{U_{x,N-1}}^{U_{x,N}} m_c dU_x = -\int_{t_{N-1}}^{t_N} \mu_w F_N(t)\, dt$. $F_N(t)$ can be calculated by Eq. 4.6 and 4.11. Finally the discretised tangential velocity at the N_{th} time step can be expressed by (note that the values of A between two adjacent time steps are considered as equal):

$$\Delta U_{x,N} = -0.5\mu_w \left(U^{(0)} \sin\alpha\right)^{3.5} \frac{t_N^{2.5} - t_{N-1}^{2.5}}{h^{2.5}} A_{t=t_N}^{1.5} \tag{4.13}$$

Rolling friction behaves differently in sliding and non-sliding periods. At the sliding period (creepage), $U_x > \omega_z R_c$, the angular velocity, ω_z, is accelerated by the friction force and reaches the maximum at $\omega_z^{(s)}$. At the non-sliding period (gross rolling), $U_x = \omega_z R_c$, the angular velocity is decelerated by the torque of the rolling resistance. We consider the sliding period at first. The torque at the mass centre *O* of the carrier is given by $T_O = F_f\left(R_c - y\right) \approx F_f R_c$ (*y* is a very small deformation comparing to R_c). By definition we have $T_O = I_c\, d\omega_z / dt$, where $I_c = 0.4 m_c R_c^2$ is the moment of inertia of the carrier sphere. Then separate the $d\omega_z$ and dt onto each side of the equation and integrate on the both sides: $\int_{t_{N-1}}^{t_N} F_f R_c dt = \int_{\omega_{z,N-1}}^{\omega_{z,N}} I_c d\omega_z$. Finally the discretised angular velocity at the N_{th} time step can be written as:

$$\Delta\omega_{z,N} = -2.5\Delta U_{x,N} / R_c \qquad 4.14$$

The angular velocity, ω_z, for the sliding period can be solved by accumulating the discretised values for every time steps as following:

$$\omega_z = \omega_z^{(0)} + \sum_{i=0}^{i=N} \Delta\omega_{z,i} \qquad 4.15$$

The non-sliding period is reached at the time step where $U_x = \omega_z R_c$. At the non-sliding period, no friction force exists and the angular velocity is decelerated by the torque resistance. Therefore, in order to estimate the instantaneous angular velocity during gross rolling, the torque resistance should be known. We start from the contact radius of the carrier which is given by $a_c = \sqrt{R_c^{\ 2} - \left(R_c - y\right)^2}$, expanding to $a_c^{\ 2} = 2R_c y\left(1 - y / 2R_c\right)$. Since *y* is a very small deformation comparing to R_c, the relation between a_c and *y* is simplified by:

$$a_c = \sqrt{2R_c y} \qquad 4.16$$

The contact radius of the carrier is defined as the region *A* in the *xz*-plane: $A = \left\{\left(x, z\right) : x^2 + z^2 \le a_c^{\ 2}\right\}$. The normal stress p_y is given by:

$$p_y\left(x,z\right)=p_0\sqrt{1-\left(x/a_c\right)^2-\left(z/a_c\right)^2} \qquad 4.17$$

with p_0 constant. The total normal force, F_N, can be calculated by the normal stress p_y:

$$F_N=\int_{-a_c}^{a_c}\int_{-a_c(x)}^{a_c(x)}p_y\left(x,z\right)dzdx \qquad 4.18$$

where $a_c\left(x\right)=\sqrt{a_c^2-x^2}$, from Eq. 4.17 and 4.18 we can get the expression of p_0:

$$p_0=\frac{3}{2\pi a_c^2}F_N \qquad 4.19$$

Then the torque resistance can be calculated by:

$$T_o\left(y\right)=\int_0^{a_c}\int_{-a_c(x)}^{a_c(x)}p_y\left(x,z\right)\cdot x\;dzdx=\frac{3}{16}a_cF_N=\frac{\sqrt{2}}{4}\frac{E_cR_c}{1-\sigma_c^2}y^2 \qquad 4.20$$

$T_o(y)$ can transform to $T_o(t)$ by Eq. 4.11. Then the discretised angular velocity at the non-sliding period can be calculated from the integral: $-\int_{t_{N-1}}^{t_N}T_o\left(t\right)dt=\int_{\omega_{z,N-1}}^{\omega_{z,N}}I_cd\omega_z$, and is given by:

$$\Delta\omega_{z,N}=-\frac{5\sqrt{2}}{24}\frac{E_c\left(U^{(0)}\,sin\,\alpha\right)^2}{m_cR_c\left(1-\sigma_c^2\right)}\left(t_N^3-t_{N-1}^3\right)A_{t=t_N}^2 \qquad 4.21$$

Then the angular velocity at N_{th} time step in non-sliding period can be expressed by:

$$\omega_z=\omega_z^{(s)}+\sum_{i=s}^{i=N}\Delta\omega_{z,i} \qquad 4.22$$

s is the time step at the end of sliding period. At the end of compression phase ($t=\tau$), $U^{(1)}$ and $\omega_z^{(1)}$ are directly obtained.

At the recovery phase, the normal velocity, U_y, will be fully recovered under Assumption III and no need to discuss here. The tangential velocity, U_x, stays equal to $\omega_z R_c$ during the recovery period. The determination of the decrement of the angular velocity, $\Delta\omega_z$, is as same as Eq.4.21. The angular velocity at N_{th} time step for recovery period is given by:

$$\omega_z = \omega_z^{(1)} + \sum_{i=\tau}^{i=N} \Delta\omega_{z,i} \qquad 4.23$$

$\omega_z^{(2)}$ can be obtained at $t = 2\tau$ from the above equation, and $U_x^{(2)} = \omega_z^{(2)} R_c$. It should be noted that the carrier is possible to stop rolling during the non-sliding period in compression and recovery phases. The loop should be jump out when this phenomenon happens.

The angular velocities around x and y axis, ω_x and ω_y, are decreased during the whole collision process, and are given by:

$$\omega_x = \omega_x^{(0)} + \sum_{i=0}^{i=N} \Delta\omega_{x,i}\, , \omega_y = \omega_y^{(0)} + \sum_{i=0}^{i=N} \Delta\omega_{y,i} \qquad 4.24$$

where $\Delta\omega_x$ and $\Delta\omega_y$ can be determined by Eq. 4.21 while substitute $\Delta\omega_z$ to $\Delta\omega_x$ and $\Delta\omega_y$. Eq. 4.24 is valid for all cases.

4.1.3 Case II

The procedure for Case II follows that for Case I except that the period of sliding falls in the recovery period. The appropriate variables are shown in Table 4.2.

$U_x^{(1)}$, $\omega_z^{(1)}$ and $U_x^{(s)}$, $\omega_z^{(s)}$ are calculated according to Eq. 4.12 and 4.15 at $t = \tau$ and $t = s$. The sliding periods ends at the time step where $U_x = \omega_z R_c$. During the non-sliding period, the relationship of $U_x = \omega_z R_c$ keeps and the velocities can be calculated by Eq. 4.21 and 4.22. $U_x^{(2)}$ and $\omega_z^{(2)}$ are directly obtained at $t = 2\tau$.

Pre-collision	Compression period (1)	Recovery period (2)	Post-collision
	sliding period		
Trans. Velocity	$U^{(0)}$	$U^{(1)}$ $U^{(s)}$	$U^{(2)}$
Angular velocity	$\omega^{(0)}$	$\omega^{(1)}$ $\omega^{(s)}$	$\omega^{(2)}$

Table 4.2 Velocities for Case II.

4.1.4 Case III

Case III is the simplest because it is not necessary to distinguish between the period of sliding and non-sliding. The variables for Case III are shown in Table 4.3. All velocities can be calculated by Eq. 4.12 and 4.15.

Pre-collision	Compression period (1)	Recovery period (2)	Post-collision
Trans. Velocity	$U^{(0)}$	$U^{(1)}$	$U^{(2)}$
Angular velocity	$\omega^{(0)}$	$\omega^{(1)}$	$\omega^{(2)}$

Table 4.3 Velocities for Case III.

4.1.5 Detachment criterion

The drugs have the maximum detachment fraction when its inertia force reaches the maximum. For case II and III, the maximum inertia force is always found at the end of compression phase, $t = \tau$. However, for case I, the friction force is damped to zero at the non-sliding period, hence the maximum inertia force may be found at $t = s$. The expression of the maximum drug inertia force is given by:

$$\text{Case I: } F_{in,d,max} = max\left\{\sqrt{F_{N,t=\tau}{}^2 + F_{f,t=\tau}{}^2}, \sqrt{F_{N,t=s}{}^2 + F_{f,t=s}{}^2}\right\} \cdot \frac{m_d}{m_c}$$

$$\text{Case II \& III: } F_{in,d,max} = \sqrt{F_{N,t=\tau}{}^2 + F_{f,t=\tau}{}^2} \cdot \frac{m_d}{m_c} \qquad 4.25$$

Then separate the $F_{in,d,max}$ into a normal ($F_{in,n}$) and a tangential ($F_{in,t}$) component by Eq. 4.3 and use these values for the detachment study. The detachment criterion is similar to the plane wall detachment model (Section 3.1.1) while substitute the fluid dynamic force by the inertia force and remove the hydrodynamic toque around drug centre (Assumption I). The lift-off, sliding and rolling detachment criterion are given by:

$$\begin{aligned} &\text{Lift-off: } F_{in,n} > F_{vdW} \\ &\text{Sliding: } F_{in,t} > \left(F_{vdW} - F_{in,n}\right) \cdot \mu_d \\ &\text{Rolling: } F_{in,t} \cdot R_d > \left(F_{vdW} - F_{in,n}\right) \cdot a_d \end{aligned} \qquad 4.26$$

where μ_d is the friction coefficient between the drug and carrier. a_d is the contact radius of the drug particle and can be calculated by the JKR theory (Eq. 3.6).

4.2 Results analysis

The material properties of the carrier and drug particles used for the simulation are based on Table 3.1 and Table 3.2 which are provided by our project partner (Cui, et al., 2014). The carrier particle is covered with a 50% coverage degree by drug particles, together with a size ratio $D_{drug}/D_{carrier} = 5\ \mu m/100\ \mu m$. The friction coefficient between the carrier and the wall, μ_w, vary from 0.1 to 0.5. The range of the impact angle, α, is between $1°$ to $90°$ ($0°$ is not considered since there is no collision). From the preliminary study the initial mean velocity of the cluster, $U^{(0)}$, is approximately $10\ m/s$. The initial angular velocity, $\omega^{(0)}$, is assumed as zero. The surface treatment method of the carrier surface is chosen as *TC 8h* (Table 3.2).

4.2.1 Parameter study

As discussed above, the inertia forces on all drug particles have the same value and preserve the same direction as the carrier inertia force. The maximum drug inertia force in *y*-direction, $F_{in,d,y,max}$ (Eq. 4.2), is always found at $t = \tau$ and is depicted in dependence of the impact angle in Fig. 4.4. The maximum drug inertia force in *x*-direction, $F_{in,d,x,max}$, are not always at $t = \tau$ but sometimes at $t = s$, and thus was not plotted. As shown in Fig. 4.4, $F_{in,d,y,max}$ increases while increasing the impact angle, since more kinematic energy is transformed into the potential energy (Eq. 4.7). From *1°* to *90°* of the impact angle, $F_{in,d,y,max}$ was increased from *141 nN* to *18100 nN*. Comparing to the fluid dynamic forces on drug particles in Section 2.4, the drug inertia force is much larger and can lead to a direct lift-off detachment.

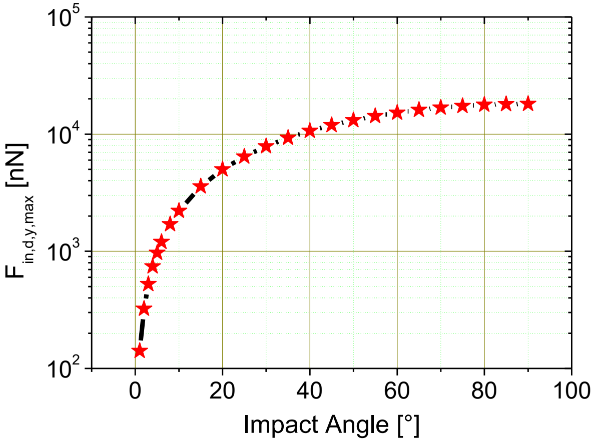

Fig. 4.4 Maximum drug inertia force in *y*-direction as a function of the impact angles (coverage degree = 50%, $D_{drug}/D_{carrier}$ = 5/100, μ_w = 0.1, U_0 = 10 m/s).

Next select the impact angle of *80°* and study the transition of several parameters as a function of compression distance. Fig. 4.5 shows the change of carrier friction force during the compression phase. The friction force of the carrier is initially increased by the growing compression distance. This is the sliding period (creepage) and the friction force is proportional to the normal force (Eq. 4.6 and 4.9). When the carrier reaches to the non-sliding period (gross rolling) at $x = 0.859h$, the friction force is damped to zero according to Eq. 4.9. From Fig. 4.5, it’s clear that the sliding period ends at the compression phase and this is the case I.

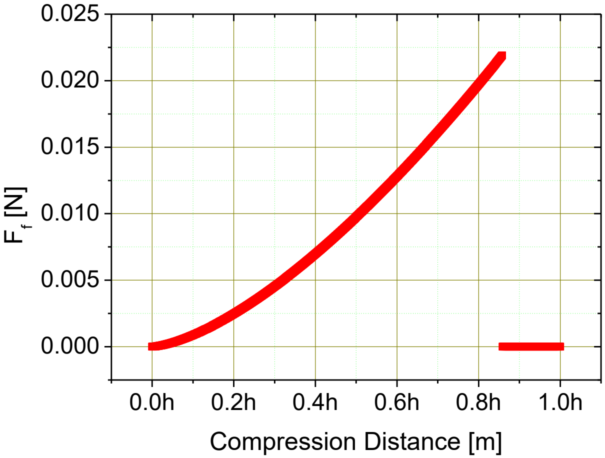

Fig. 4.5 Friction force of the carrier as a function of compression distance (coverage degree = 50%, $D_{drug}/D_{carrier}$ = 5/100, α = 80°, μ_w = 0.1, U_0 = 10 m/s).

Fig. 4.6 offers an overview of the instantaneous velocities of the carrier particle in compression phase. The normal velocity component is decreased from *9.85 m/s* to *0 m/s* according to Eq. 4.10, meanwhile the moment in the normal direction is fully transformed into the potential energy. The tangential velocity of the carrier is decreased from *1.74 m/s* by the friction force (Eq. 4.12 and 4.13) and the angular velocity is increased by the friction force (Eq. 4.14 and 4.15). At $x = 0.859h$, the non-sliding period starts. When $x > 0.859h$, the relationship of $U_x = \omega_z R_c$ keeps and the carrier thereafter rolls without sliding, at the non-sliding period the angular velocity can be calculate by Eq. 4.21 and 4.22.

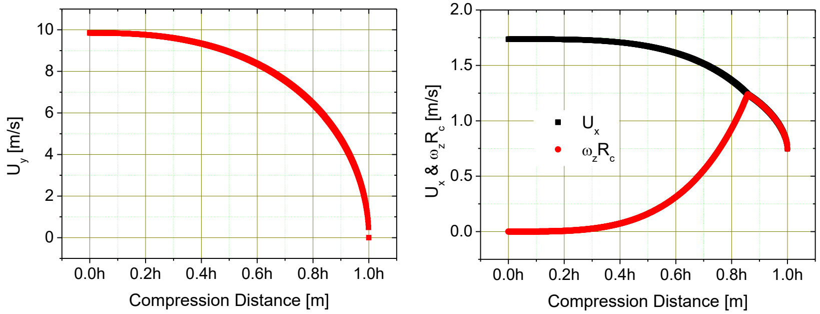

Fig. 4.6 Instantaneous velocities of the carrier sphere as a function of compression distance, left: normal velocity, right: angular and tangential velocities (coverage degree = 50%, $D_{drug}/D_{carrier}$ = 5/100, α = 80°, $\mu_w = 0.1$, U_0 = 10 m/s).

Fig. 4.7 shows the normal inertia force on each drug particles, which is the decomposition force from the inertia force in the direction of centre line between the carrier and drug particles (Eq. 4.3). As shown from Fig. 4.7, the scatter of the normal inertia force becomes larger while increasing the impact angle. This is reasonable due to the increase of the drug inertia force (Fig. 4.4). The data points for a certain impact angle are symmetrical. The reason is that half of the drug particles experience an inertia force which points to the surface of the carrier. Only the other half of drugs encounters an inertia force which points out of the carrier, from where the lift-off detachment may occur. From the experiment, the measured mean van der Waals force for treated carrier particle (TC 8h) is *62.48 nN*. Comparing to the values in Fig. 4.7, nearly half of the drug particles are likely to detach even at impact angle *10°*. The influence of the friction coefficient between the carrier and the wall, μ_w, on the normal inertia force is shown in Fig. 4.8. The friction force of carrier in sliding period increases while raising the μ_w. Hence the maximum drug inertia force increases either. With the increasing friction coefficient the scatter of the normal inertia force on drugs slightly grows and its maximum value moves to the rear. It should be noted that the non-sliding period becomes easier reachable while increasing the μ_w. Therefore, the reader should choose the μ_w carefully.

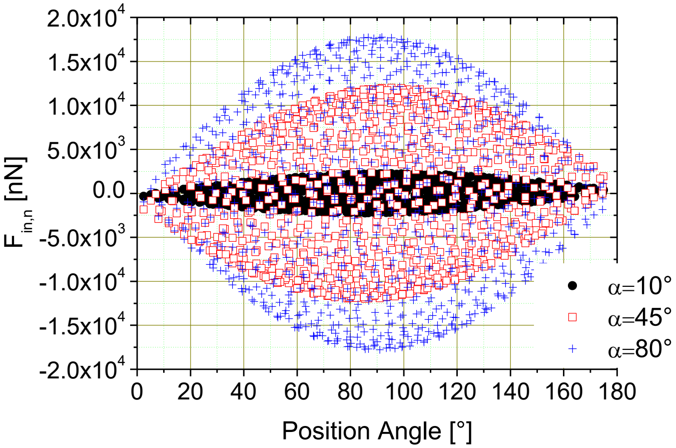

Fig. 4.7 Normal inertia force on the drug particles as a function of the position angle for different impact angles (coverage degree = 50%, $D_{drug}/D_{carrier}$ = 5/100, μ_w = 0.1, U_0 = 10 m/s).

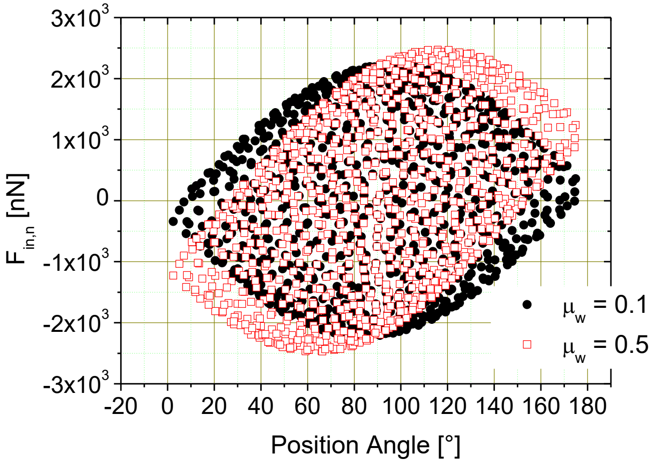

Fig. 4.8 Normal inertia force on the drug particles as a function of the position angle for different friction coefficients between the carrier and the wall (coverage degree = 50%, $D_{drug}/D_{carrier}$ = 5/100, α = 10°, U_0 = 10 m/s).

Fig. 4.9 shows the tangential inertia force on the drug particles under three impact angles. Across the sphere of the carrier particle, the maximum tangential inertia force on drugs is found along a circle, where the inertia force coincide the local tangential direction. Therefore the maximum values of the tangential inertia force are found in a wide range of position angles. The minimum tangential inertia force locates at the positions where absolute normal inertia force reaches the maximum. As shown in Fig. 4.10, there are two minimum of the tangential inertia force, corresponding to the two maximal absolute values of the normal inertia force in Fig. 4.8. While increasing the friction coefficient between the carrier and the wall, the distance between two minimum expands. However, when the non-sliding period is reached or the impact angle becomes *90°*, there only exists one minimum of the tangential inertia force.

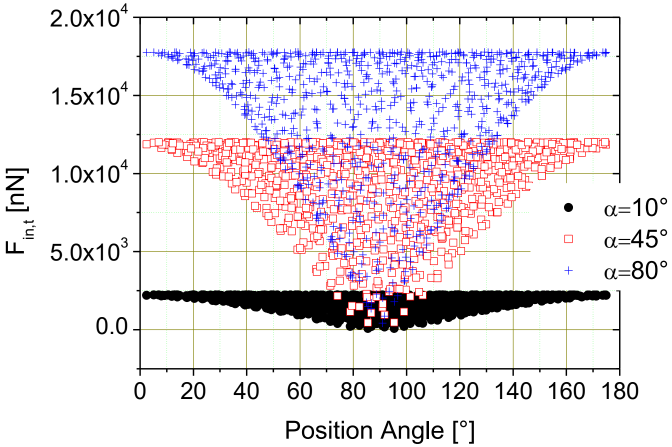

Fig. 4.9 Tangential inertia force on the drug particles as a function of the position angle for different impact angles (coverage degree = 50%, $D_{drug}/D_{carrier}$ = 5/100, $\mu_w = 0.1$, U_0 = 10 m/s).

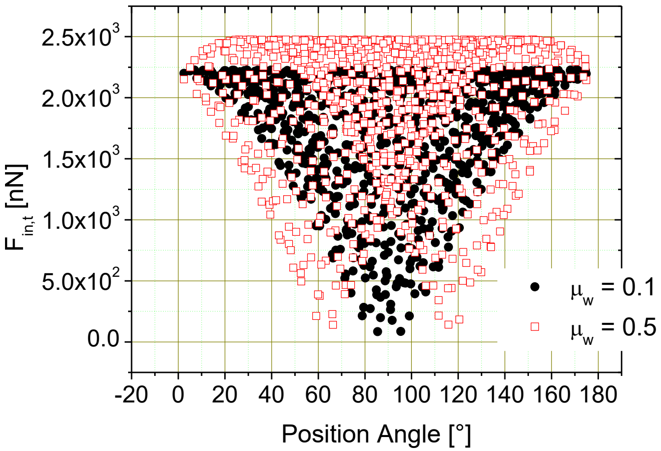

Fig. 4.10 Tangential inertia force on the drug particles as a function of the position angle for different friction coefficients between the carrier and the wall (coverage degree = 50%, $D_{drug}/D_{carrier}$ = 5/100, $\alpha = 10°$, $U_0 = 10$ m/s).

4.2.2 Detachment study

The drugs can be removed from carrier surface by three types of detachment: lift-off, sliding and rolling. The detachment criterion holds for each case is offered by Eq. 4.26. The coverage degree is irrelevant to the inertia force, hence has no influence on the drug detachment. The size of drug particle only influences the contact radius (Eq. 3.6).

Fig. 4.11 plots the lift-off detachment probability as a function of the impact angle. The lift-off probability starts with 27.92% at impact angle 1°. While increasing the impact angle, the maximum inertia force increases significantly (Fig. 4.4), and hence the lift-off probability becomes larger. Finally it reaches up to 49.60% at impact angle 90°. 100% detachment by lift-off is not possible, since half of the drug particles experience negative normal inertia force (Fig. 4.7).

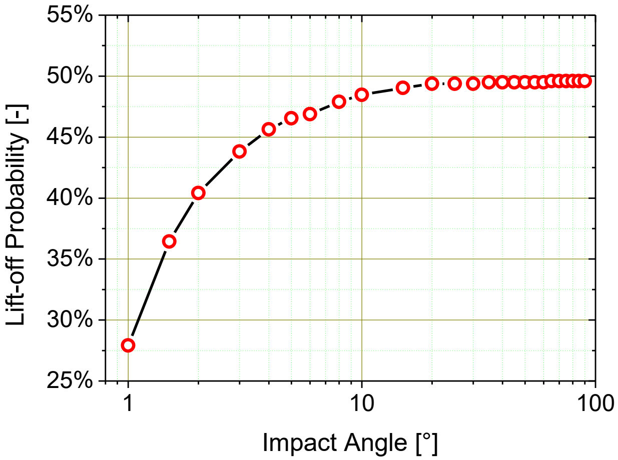

Fig. 4.11 The lift-off probability of drug particles as a function of the impact angles (coverage degree = 50%, $D_{drug}/D_{carrier}$ = 5/100, μ_w = 0.1, U_0 = 10 m/s, surface treatment: TC 8h).

If one drug particle can be detached by the lift-off, there is no more external load on the drug particle to the carrier surface. The friction force does not exist and the contact radius becomes zero. Therefore, the sliding and rolling detachment can only occur on those drug particles which are not yet detached by the lift-off. Fig. 4.12 exhibits the normal inertia force of those drug particles as a function of the position angle. 10° of impact angle is selected as the example for the detachment study. The data points with value larger than the measured van der Waals force (62.48 nN) are already removed from Fig. 4.12. Finally, 51.47% of drugs are remaining on the carrier surface.

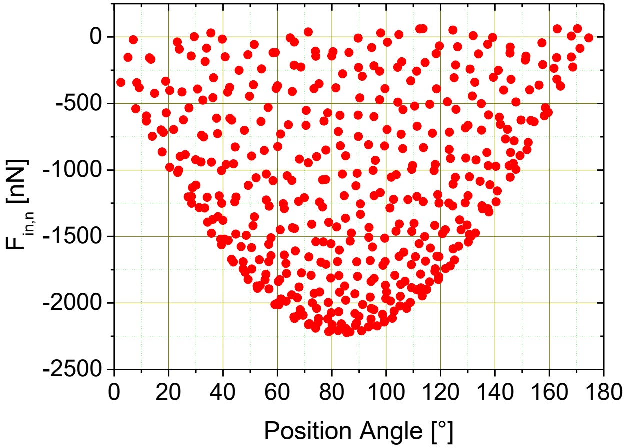

Fig. 4.12 Normal inertia force on non-lift-off drug particles as a function of the position angle (coverage degree = 50%, $D_{drug}/D_{carrier}$ = 5/100, α = 10°, μ_w = 0.1, U_0 = 10 m/s).

Fig. 4.13 exhibits the tangential inertia force corresponding with the friction force for the remaining drug particles. The squares are the data of the tangential inertia force and the points signify the friction forces on each drug particles. When the tangential inertia force is larger than the friction force, the sliding detachment takes place. Plotting the left and right parts of Eq. 4.26 (Rolling) as a function of the position angle, Fig. 4.14 describes the rolling detachment. The squares denote the left part while the points signify the right part of Eq. 4.26 (Rolling). The rolling only occurs when the left part is larger than the right part. Fig. 4.13 and Fig. 4.14 reveal that nearly 100% of the remaining drug particles can be detached by sliding or rolling.

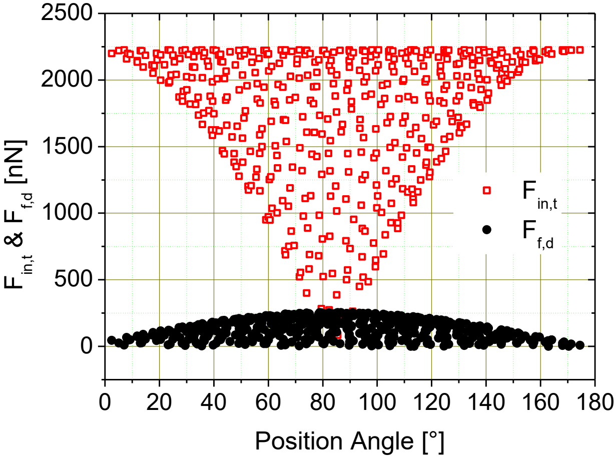

Fig. 4.13 Tangential inertia force and friction force on drug particles as a function of the position angle (coverage degree = 50%, $D_{drug}/D_{carrier}$ = 5/100, α = 10°, μ_w = 0.1, U_0 = 10 m/s, surface treatment: TC 8h).

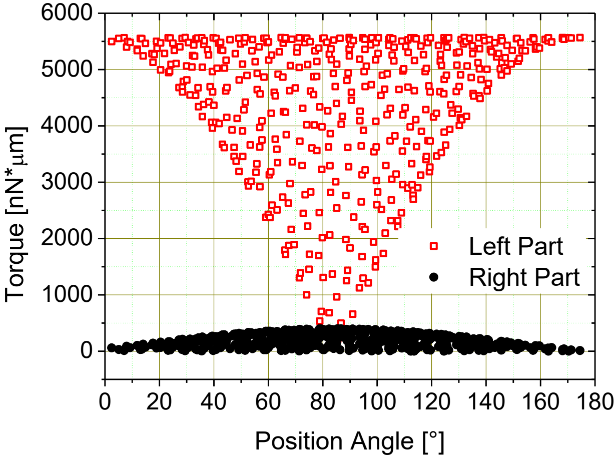

Fig. 4.14 The left and right parts of Eq. 4.26 (Rolling) on drug particles as a function of the position angle (coverage degree = 50%,

$D_{drug}/D_{carrier}$ = 5/100, α = 10°, μ_w = 0.1, U_0 = 10 m/s, surface treatment: TC 8h).

Finally, for those drug particles which can be detached both by sliding and rolling, the question is which detachment phenomenon is actually occurring: sliding or rolling? This may be found from Eq. 4.26 yielding a non-dimensional ratio:

$$Ratio = \left(F_{in,t} \cdot R_d / a_d + F_{in,n}\right) / \left(F_{in,t} / \mu_d + F_{in,n}\right) \qquad 4.27$$

If the variable *Ratio* is larger than one, the rolling detachment occurs first; if *Ratio* is smaller than one, the sliding detachment occurs first on the contrary. Fig. 4.15 depicts the data points of *Ratio* which are displayed as points for every drug particle as a function of the position angle. The straight solid line indicates the critical value. *Ratio* reaches to the maximum at the middle of position angle and all its values are larger than one. It is obvious that the rolling is much easier than the sliding detachment in frame of cluster-wall collision study.

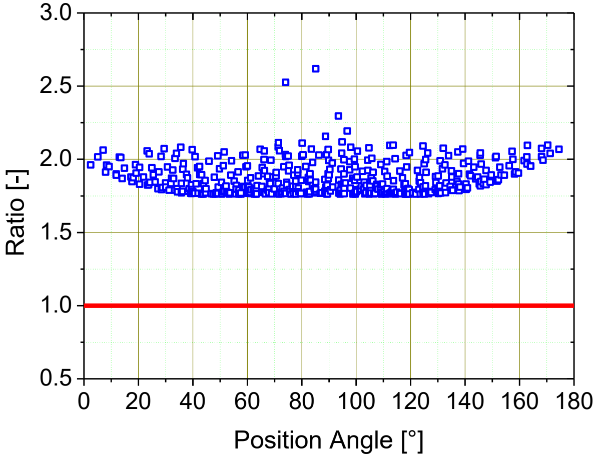

Fig. 4.15 Data points of *Ratio* (coverage degree = 50%, $D_{drug}/D_{carrier}$ = 5/100, α = 10°, μ_w = 0.1, U_0 = 10 m/s, surface treatment: TC 8h).

5 Summary and Outlook

The forces acting on the fine drug particles attached to the surface of a larger carrier particle (dry powder inhaler formulation) were numerically calculated for estimating the drug particle detachment probability during its way through an inhaler. When the particle clusters move through an inhaler device, they will rotate due to the shear in the flow as well as wall collisions whereby more drug particles might detach. Additionally, the flow in an inhaler is highly turbulent so that the drug particles experience higher and strongly fluctuating instantaneous fluid velocities. Therefore, the plane wall detachment model for laminar and turbulent flows, the rough wall detachment model and the particle-wall collision model were studied, respectively.

At first, the particle cluster was placed centrally in a rectangular computational domain and exposed to a laminar plug flow with different carrier Reynolds number (*Re* ranges from 0.5 to 200). The required high spatial resolution of the drug particles was achieved by local grid refinement and a curved wall bounce-back boundary condition. Moreover, a special treatment of the region between particles in close contact (i.e. when the spacing is smaller than a grid cell) was utilized in order to allow the calculation of the fluid forces on the drug particles separately.

To validate the computational approach first the drag and lift coefficients acting on a single particle which is attached to a plane wall and exposed to a linear shear flow was simulated. The comparison with analytical solutions and other numerical simulations showed very good agreement. Furthermore, the required domain size was carefully analysed through numerous simulations and the dimensions were selected in order to obtain accurate results for the forces on the drug particles and to minimize the computational effort.

As to be expected the normal and tangential forces on the fine particles strongly vary with the angular position on the carrier and increase with the Reynolds number. On the front hemisphere of the cluster up to position angles between 60° to 40° (with increasing Re) the normal force is negative (i.e. towards the carrier). The maximum of the normal force moves from the rear stagnation point at small *Re* to an angular position of about 75° at the highest value, Re = 200. Even at this high Reynolds number drug particle detachment by lift-off is not possible when comparing the normal force with the measured van der Waals forces. The tangential force is highest on the front hemisphere of the cluster, between about 10° and 90°, being almost independent on Reynolds number.

With decreasing coverage degree the forces on the drug particles increase remarkably, as more and more small particles are exposed to higher flow velocities. The reduction of the drug particle size diminishes the fluid dynamic forces.

It was shown that a shear flow (in this case G = 100,962 1/s) does not remarkably affect the mean normal force on the drug particles, however, the scatter of the forces is slightly higher than in a plug flow.

The drag coefficient of the particle cluster was found to lie above that of a rigid sphere, especially for high coverage degree and low Reynolds number.

The detachment probability in dependence of the angular position of the drug particles on the carrier was examined. This analysis was based on measured adhesion properties (i.e. van der Waals force, friction coefficient and adhesion surface energy). As mentioned above, lift-off is not possible for the considered Reynolds numbers. Hence, the remaining mechanisms for drug powder detachment are sliding and rolling. Sliding detachment at Re = 200 is only possible in a relatively narrow angular range between 25° and 75°, whereas rolling occurs in the whole range of position angle. Moreover, rolling detachment probability is much higher than that of sliding. From the ratio of the conditions for rolling and sliding it was found that rolling detachment will always occur first for Re = 100 and 200.

Turbulence was successfully generated by a digital filtering technique that was applied at the inlet boundary. For validating this approach, simulations without particles were performed and the velocity components of a series of fluid nodes along the stream-wised direction were recorded during the simulation. From these results, an almost constant turbulence field was found in the middle of the fluid domain, which is the prerequisite of conducting simulations with the particle cluster experiencing defined turbulence properties.

Following that, a LBM simulation at a carrier Reynolds number of Re = 200 and a prescribing turbulence intensity of I = 9.0% was conducted with the particle cluster, and then compared to the laminar flow. As to be expected, the force vector direction on the drug particles is strongly distorted by turbulence resulting from the temporarily varying flow structure about the cluster. The drug particle which has the largest normal force was found at position angle of 85°. Here the instantaneous maximum normal force was raised from 5 *nN* to 51 *nN* when increasing turbulence intensity from 0.3% to 9.0%. Hence, turbulence is very effective for particle detachment.

For calculating detachment possibilities, the instantaneous forces and hydrodynamic moments are required. Lift-off is not likely to occur due to small normal fluid force. Sliding and rolling detachment probabilities are significantly increased through the action of turbulence. Compared to the laminar flow with Re = 200 rolling detachment probability was increased from 50% to 98% while sliding probability was raised from 21% to 75% when prescribing a turbulence intensity of I = 9.0%. Similar to laminar conditions, the rolling detachment probability is higher than that for sliding. In turbulent flow, drugs which can be detached by both rolling or sliding are locate over the whole range of position angle (i.e. 0 to 180°), whereas in laminar flow this is only observed in an angular range between 10° - 100° for the same Re = 200. From the ratio of the conditions for rolling and sliding it was found that rolling detachment will always occur first for Re = 200. Consequently rolling detachment results at typical carrier Reynolds numbers with moderate turbulence intensities in an almost 100% separation of the drug particles from the carrier.

In the rough wall simulation, one smooth drug particle was placed on a rough carrier surface. The size of carrier is much larger than the drug size and thus was assumed as a rough wall. The roughness was simplified by a row of semi-cylinders in the stream-wised direction of the flow on the wall, and was varied by the asperity distance between the rough elements and the size ratio between the semi-cylinder and the drug particle. Both the size ratio and asperity distance can be represented by the contact distance.

The required domain size was carefully analysed through numerous simulations and the dimensions were selected in order to obtain accurate results for the forces on the drug particles and keep the computational effort as small as possible. Furthermore, parameter study was carried to understand the relationship between the contact distance, the asperity distance, the size ratio and the particle height.

At the inlet a plug flow is prescribed, a shear flow develops downstream due to the no-slip boundary condition of the rough wall and was named of the wall induced shear flow. The velocity profiles were extracted along a vertical line which locates in front of the drug particle. The flow velocity was increased of 5% - 10% at the height of $2D_d$ by the wall induced shear flow, and was further enhanced by the existence of the roughness element.

The hydrodynamic torque coefficient (htc) of the drug particle which determines the hydrodynamic torque around the particle centre was numerically calculated. The htc decreases while increasing particle Reynolds number and increases when the contact distance rises up.

The direct lift-off of the drug particle dose not occurs in the rough wall study. Both the sliding and rolling ratios decrease while increasing the contact distance. The rolling detachment is not likely to happen whereas the sliding detachment happens for a wider range. It was shown that the roughness increases the difficulty of the rolling and sliding detachment probability comparing to the plane wall study. Moreover, from the ratio of the conditions for rolling and sliding it was found that sliding detachment will always occur earlier than rolling which is in contrast to the finding in the plane wall detachment study. The reason is that the contact distance is introduced into the rolling criterion of the rough wall detachment model, therefore the particle encounters much larger torque resistance in the rough wall detachment model comparing to the plane wall detachment model. It should be noted that the above rolling and sliding detachment studies use the same adhesion forces (TC 8h in Cui, et al., 2014). However, in experiment the increase of roughness reduced the adhesion force. This phenomenon is not considered in the present study.

When a carrier particle collides onto the wall with an impact angle, the inertia force is exerted on the drug particles which reside on the carrier surface. During the deformation process, the carrier can slide and roll on the wall. Both the translation and rotation of the carrier occur simultaneously. The tangential velocity of the carrier is reduced by the friction force, whereas the angular velocity is accelerated by the friction force. When the linear velocity is equal to the translation velocity, the carrier thereafter rolls without slipping. At this moment the frictional force disappears, and the carrier begins the second stage of its motion. At the gross rolling stage, the rolling speed is decelerated by the torque of the rolling resistance. The whole processes were solved numerically.

With an increasing impact angle the normal inertia force increases, since more kinematic energy is transformed to the potential energy. The tangential inertia force is proportional to the normal component at the rolling-sliding stage, and damps to zero when the gross rolling stage is reached. The friction coefficient of the wall increases the tangential inertia force. However, the wall friction coefficient should be carefully selected, since the gross rolling stage becomes easier reachable while increasing its value.

The centripetal force on the fine drug particles is very tiny comparing to the inertia force and thus was neglected. The hydrodynamic torque disappears and the inertia force is acting on the centre of the drug particles. The inertia force is much larger than the fluid dynamic force and dominates the detachment of drug particles. The lift-off probability increases while increasing the impact angle. However, 100% detachment by lift-off is not possible, since half of the drug particles experience negative normal force. The sliding and rolling detachment can only occur on those drug particles which are not yet detached by the lift-off. It was shown that nearly 100% of the remaining drug particles can be detached by sliding and rolling. Furthermore, from the non-dimensional ratio of the conditions for rolling and sliding it was found that rolling detachment will always occur first than sliding. However, the collision deformation is a time-dependent process. The inertia force of the drug particles is not a pulse but increases instantaneously. Therefore, the rolling detachment occurs first at the early deformation of the carrier, and then followed with the sliding and lift-off detachment at larger deformations. For the optimisation of the DPI high particle-wall collision rate is expected.

In future, more turbulent simulations will be performed to enrich the data. Secondly, the hemisphere will be selected as the rough elements in order to generate the three-dimensional roughness. Thirdly, based on the above findings a Lagrangian detachment model will be developed which can be used for Euler/Lagrange calculations of an inhaler device and allow an optimization with regard to pressure drop and efficiency of drug powder delivery.

Nomenclature

Latin letters		**Unit**
A_P	cross section area of the particle	m^2
a	acceleration speed	m/s^2
a_r	contact distance	m
a_d	contact radius of the drug particle	m
a_c	contact radius of the carrier particle	m
C_d, C_D	drag coefficient	-
C_L, C_{LS}	lift coefficient	-
D, D_P	particle diameter	m
D_c, $D_{carrier}$	diameter of the carrier particle	m
$D_{cluster}$	diameter of the particle cluster	m
$D_{cylinder}$	diameter of the cylinder	m
D_d, D_{drug}	diameter of the drug particle	m
E_c, $E_{carrier}$	Young's modulus of the carrier particle	Pa
E_d, E_{drug}	Young's modulus of the drug particle	Pa
F_D	drag force	N
F_f	friction force	N
$F_{in,c}$	inertia force of the carrier particle	N
$F_{in,d}$	inertia force of the drug particle	N
F_L	lift force	N
F_{lub}	lubrication force	N
F_N	normal force of the carrier	N
F_n	normal force of the drug particle	N
F_t	tangential force of the drug particle	N
F_{total}	total fluid dynamic force of the drug particle	N
F_{vdW}	van der Waals force of the drug particle	N
$f_{\sigma i}$	velocity distribution function	-
$f_{\sigma i}^{(0)}$	equilibrium distribution function	-

G	shear rate	s^{-1}
gl	grid level	-
h	maximal compression distance	m
htc	hydrodynamic torque coefficient	-
I	turbulence intensity	-
I_c	moment of inertia of the carrier particle	$kg \cdot m^2$
k	turbulent energy	m^2/s^2
L	asperity distance of the rough elements	m
m_c	mass of the carrier particle	kg
m_d	mass of the drug particle	kg
M_{hyd}	hydrodynamic moment around particle centre	$N \cdot m$
P	external load	N
R_P	particle radius	m
R_c, $R_{carrier}$	radius of the carrier particle	m
$R_{cylinder}$	radius of the cylinder	m
R_d, R_{drug}	radius of the drug particle	m
Re, Re_p	particle Reynolds number	-
Re_{drug}	drug particle Reynolds number	-
$Re_{carrier}$	carrier particle Reynolds number	-
Re_s	shear Reynolds number of the particle	-
T	turbulence integral time scale	s
t	time	s
$U^{(0)}$	initial translational velocity	m/s
$U^{(1)}$	translational velocity at the end of compression phase	m/s
$U^{(2)}$	translational velocity at the end of recovery phase	m/s
$U^{(s)}$	translational velocity at the end of sliding period	m/s
U_{mean}	mean velocity	m/s

Greek letters		**Unit**
α	impact angle	°
γ	adhesion surface energy	J/m^2
μ	dynamic viscosity of the fluid	Pa·s
μ_w	friction coefficient between the carrier and the wall	-
μ_d	friction coefficient between the drug and the carrier	-
ρ	fluid density	$kg \cdot m^{-3}$
σ_F	forcing amplitude	-
σ_c, $\sigma_{carrier}$	Poisson's ratio of the carrier particle	-
σ_d, σ_{drug}	Poisson's ratio of the drug particle	-
u_{rms}	root-mean-square of the turbulent velocity fluctuations	m/s
τ	compression time	s
ω	angular velocity of the carrier	rad/s

Abbreviations	
AFM	Atomic Force Microscopy
API	Active Pharmaceutical Ingredient
BGK	Bhatnagar-Gross-Krook
CD	Coverage Degree
CFD	Computational Fluid Dynamics
DMT	Derjaguin-Muller-Toporov
DNS	Direct Numerical Simulation
DPI	Dry Powder Inhaler
ED	Emitted Dose
EDF	Equilibrium Distribution Function
FH	Filippova & Hänel
FPD	Fine Particle Dose
FPF	Fine Particle Fraction
HIT	Homogeneous Isotropic Turbulence
JKR	Johnson-Kendall-Roberts
LBE	Lattice Boltzmann Equation

LBM	Lattice Boltzmann Method
PDF	Probability Density Function
RANS	Reynolds-Averaged Conservation Equations
SR	Size Ratio

List of Figures

Fig. 1.1 Summary of multi-scale approach for inhaler optimisation and design. 4

Fig. 1.2 Geometry of a typical swirl-flow inhaler device (left, taken from Donovan et al. 2012) and numerical grid used for the inhaler discretization (right, Sommerfeld & Schmalfuß, 2015). 8

Fig. 1.3 Calculated flow field of the inhaler; a) total velocity modulus and velocity vectors near the inhaler wall; b) turbulent kinetic energy energy (colour scale: m^2/s^2); c) representative particle trajectories for mono-sized particles through the inhaler; (100 L/min) (Sommerfeld & Schmalfuß, 2015). 8

Fig. 2.1 Directions of discrete equilibrium distribution function of the D3Q19 model. 13

Fig. 2.2 Treatment of the wall boundary condition on the particle surface applying the bounce-back approach: (a) stepwise representation of the particle surface inscribing the given geometry; (b) curved-wall boundary condition using the exact wall distance q between fluid node (x_{F00}) and obstacle surface (x_W) (Dietzel & Sommerfeld, 2013). 15

Fig. 2.3 Local grid refinement of a carrier particle covered by many small particles. 17

Fig. 2.4 Definition of node types at the interface between coarse and fine grid sections (Dietzel & Sommerfeld, 2013). 19

Fig. 2.5 Nodes around two particles near contact: the cycles indicate the fluid nodes far away the particle; the squares indicate the adjacent fluid nodes near the particle surface; the triangles indicate the solid nodes inside the particle; the stars indicate the solid-fluid nodes near its neighbouring particle. 20

Fig. 2.6 Boundary conditions for the simulation of a particle attach to the wall under the linear shear flow; the moving wall indicates the full-slip boundary condition; the outlet boundary has zero gradients for all parameters. 22

Fig. 2.7 Discretized mesh of a particle attach to the wall, 40 grids cells of the finest mesh pro particle diameter with three-level grid refinement (x,y,z refer to the length, width and height of the fluid domain). 24

Fig. 2.8 Domain size validation for a particle attached to a plane wall in a linear shear flow; domain size normalized by particle diameter; upper row: variation of domain size in stream-wise direction for constant dimensions in the lateral and vertical directions (y/D = 12, z/D = 12); middle row: variation of lateral dimension of the domain for x/D = 18, z/D = 12; lower row: variation of vertical dimension of the domain for x/D = 18, y/D = 12; left column: drag coefficient; right column: coefficient for slip-shear lift (3 refinement levels, particle Reynolds number Re = 0.01, shear Reynolds number Re_S = 0.02)... 25

Fig. 2.9 Drag coefficient C_D of a particle attached to a wall as a function of particle Reynolds number *Re*, comparison of a universal correlation (Eq. 2.17) based on the result of O`Neill (1968) with several simulation data obtained by different numerical methods (Derksen and Larsen, 2011; Liu et al., 2011; Zeng et al., 2009).29

Fig. 2.10 Lift coefficient C_{LS} of a particle attached to a wall as a function of the shear Reynolds number Re_S, comparison of analytic results of Leighton and Acrivos (1985) for a wall attached fixed sphere and Saffman (1965) for a freely rotating particle in an unbounded linear shear flow with several simulation data obtained by different numerical methods (Derksen and Larsen, 2011; Zeng et al., 2009)... 29

Fig. 2.11 Computational domain with applied boundary conditions. 32

Fig. 2.12 Simulated forces on the fine drug particles in stream-wise (left column) and vertical (right column) direction at different angular positions on the carrier particle; upper row: variation of grid size with increasing resolution, i.e. cells per drug particle diameter ($x/D_{carrier}$ = 7.8, $y/D_{carrier} = z/D_{carrier}$ = 6.5); middle row: variation of stream-wise dimension of the domain for $y/D_{carrier} = z/D_{carrier}$ = 6.5; lower row: variation of lateral dimension of the domain for $x/D_{carrier}$ = 7.8 (Re = 10, $D_{drug}/ D_{carrier}$ = 10/100, coverage degree = 25%, 242 drug particles)... 34

Fig. 2.13 Illustration of forces acting on the fine drug particles positioned on the large carrier particle. 36

Fig. 2.14 Flow field about the particle cluster and resulting total forces on the drug particles for three particle Reynolds numbers; left column: total force vector on drug particles; middle column: streamlines over the particle cluster; right column: experiment measurement by Taneda (1956) (coverage degree = 50%, $D_{drug}/D_{carrier}$ = 5/100). 37

Fig. 2.15 Comparison of the drag coefficient resulting from present simulation results for a particle cluster with the correlation of Schiller and Naumann (1933) for a sphere (particle diameters $D_{cluster} = D_{sphere}$ = 110 μm, coverage degree 10% and 50%, $D_{drug}/D_{carrier}$ = 5/100). 39

Fig. 2.16 Temporal variation of stream-wise force on a single drug particle at a position angle of 61.5° for two Reynolds numbers (coverage degree = 50%, $D_{drug}/D_{carrier}$ = 5/100, Δt = 0.7 ms)...................... 41

Fig. 2.17 Four times random distribution of drug particles (coverage degree = 50%, $D_{drug}/D_{carrier}$ = 5/100). 42

Fig. 2.18 Total force on all the drug particles in dependence of position angle for four different random distributions (coloured dots) and resulting polynomial fitting curve (Re = 100, coverage degree = 50%, $D_{drug}/D_{carrier}$ = 5/100). 42

Fig. 2.19 PDF of total force between position angle 40 – 60 degree; Ftotal; mean = 2.73 nN, standard deviation = 0.36 nN (Re = 100, coverage degree = 50%, Ddrug/Dcarrier = 5/100)..................... 43

Fig. 2.20 Fitting curves for the normal force on the drug particles as a function of position angle for different Reynolds numbers; a) low Re regime, b) high Re regime (coverage degree = 50%, $D_{drug}/D_{carrier}$ = 5/100). 44

Fig. 2.21 Flow field about the particle cluster and resulting direction of total fluid forces on the drug particles for Re = 0.5 (coverage degree = 50%, $D_{drug}/D_{carrier}$ = 5/100). 45

Fig. 2.22 Magnitude and angular location of maximum normal force determined from the fitting curves in dependence of Reynolds number (coverage degree = 50%, $D_{drug}/D_{carrier}$ = 5/100) 46

Fig. 2.23 Standard deviation of the normal force on drug particles in dependence of position angle (Re = 200, coverage degree = 50%, $D_{drug}/D_{carrier}$ = 5/100). 46

Fig. 2.24 Tangential force on the drug particles as a function of position angle for different particle Reynolds numbers (coverage degree = 50%, $D_{drug}/D_{carrier}$ = 5/100) 47

Fig. 2.25 Fitting curves for the normal force on the drug particles as a function of position angle for different degree of coverage (Re = 100, $D_{drug}/D_{carrier}$ = 5/100). 49

Fig. 2.26 Zoom of the flow structure around the particle cluster for different coverage, a) 10%, b) 50% (Re = 200, $D_{drug}/D_{carrier}$ = 5/100). 49

Fig. 2.27 Simulation data and fitting curves for the normal force on the drug particles as a function of position angle for different size ratio (Re = 200, coverage degree = 25%). 50

Fig. 2.28 Comparison of plug and shear flow about the particle cluster at identical Reynolds number (Re = 70); (a) normal forces in dependence of the position angle; (b) flow structure for the plug flow; (c) flow structure for the shear flow (coverage degree = 50%, $D_{drug}/D_{carrier}$ = 5/100). 52

Fig. 2.29 Velocity contour in the cross section area of the grid by the grid generated turbulence method (*porosity = 0.64*). 54

Fig. 2.30 Velocity contour along the stream-wised direction by the grid generated turbulence method (*porosity = 0.64*). 54

Fig. 2.31 Velocity fluctuations as a function of the downstream distance (*porosity = 0.64*). 55

Fig. 2.32 Flow field around a particle under the HIT plus a plug flow; left: I = 4.93%; right: I = 49.22% (Re = 100). 56

Fig. 2.33 Mean drag coefficient on a spherical particle as a function of the particle Reynolds number for different turbulence intensities. .. 57

Fig. 2.34 Turbulence intensity as a function of the forcing amplitude of the spectral forcing scheme (Re = 100). 58

Fig. 2.35 Instantaneous colour contours of the velocity component in x-direction (stream-wise direction) at the inlet boundary of the computational domain at the end of the simulation, i.e. after N = 84,500 time steps (U_{mean} = 30 m/s, I = 15.5% (in the center of the domain), integral time scale T_{int} = 60 s). 62

Fig. 2.36 Probability density distribution of the velocity components on the fluid node in the middle of fluid domain; U_x denotes the velocity component in the stream-wised direction; U_y and U_z signify the velocity components in the lateral direction (U_{mean} = 30 m/s, I = 15.5%, averaging period 64,500 to 84,500 time steps, T_{int} = 60 s). 63

Fig. 2.37 Decaying of the turbulence intensity along the stream-wised direction by the digital filtering technique for different fluid velocities (k = 11 m^2/s^2). 64

Fig. 2.38 Force vectors and streamlines of the particle cluster for the laminar and turbulence flows (Re = 200, coverage degree = 50%, $D_{drug}/D_{carrier}$ = 5/100, time step N = 75,000). 65

Fig. 2.39 Temporal variation of the normal force on the drug particle which has the largest time averaged normal force (position angle = 85°) for both the laminar and turbulent flows (Re = 200, coverage degree = 50%, $D_{drug}/D_{carrier}$ = 5/100). 66

Fig. 3.1 Spherical particle deposited on an ideal plane wall with contact area and relevant forces. 68

Fig. 3.2 Tangential force and friction force on drug particles as a function of position angle (Re = 200, coverage degree = 50%, $D_{drug}/D_{carrier}$ = 5/100, surface treatment: TC 8h). 74

Fig. 3.3 Sliding probability of drug particles as a function of Reynolds number for different surface treatment methods ($D_{drug}/D_{carrier}$ = 5/100, coverage degree = 10%). 75

Fig. 3.4 Sliding probability of drug particles as a function of the Reynolds number for different coverage degrees ($D_{drug}/D_{carrier}$ = 5/100, surface treatment: TC 8h). 76

Fig. 3.5 Contact radius of drug particles as a function of the position angle (Re = 200, coverage degree = 50%, $D_{drug}/D_{carrier}$ = 5/100, surface treatment: TC 8h). 77

Fig. 3.6 The comparison of the numerical calculated hydrodynamic torque and the analytical solution by Hubbe (Eq. 3.5) as a function of position angle (Re = 200, coverage degree = 50%, $D_{drug}/D_{carrier}$ = 5/100, surface treatment: TC 8h)......................... 78

Fig. 3.7 The numerical calculated hydrodynamic torque as a function of position angle for different degree of coverage (Re = 200, $D_{drug}/D_{carrier}$ = 5/100, surface treatment: TC 8h)......................... 79

Fig. 3.8 Fluid dynamic torque (left hand side of Eq. 3.4) and adhesion torque (right hand side of Eq. 3.4) as a function of the position angle (Re = 200, coverage degree = 50%, $D_{drug}/D_{carrier}$ = 5/100, surface treatment: TC 8h). 80

Fig. 3.9 The rolling probability of drug particles as a function of the Reynolds number for different surface treatment methods ($D_{drug}/D_{carrier}$ = 5/100, coverage degree = 10%).......................... 81

Fig. 3.10 The rolling probability of drug particles as a function of the Reynolds number at different coverage degrees ($D_{drug}/D_{carrier}$ = 5/100, surface treatment: TC 8h). 82

Fig. 3.11 Detachment probability due to sliding and rolling as a function of position angle for different Reynolds numbers; a) coverage degree = 50%, b) coverage degree = 10%, ($D_{drug}/D_{carrier}$ = 5/100, surface treatment: TC 8h). 83

Fig. 3.12 Data points of *Ratio*, Eq. 3.10 (Re = 100 and 200, coverage degree = 10%, $D_{drug}/D_{carrier}$ = 5/100, surface treatment: TC 8h). 85

Fig. 3.13 Instantaneous sliding and rolling probability of the drug particles in turbulent flow over a time of 7 s (Re = 200, *I* = 9.0%, coverage degree = 50%, $D_{drug}/D_{carrier}$ = 5/100, surface treatment: TC 8h). 86

Fig. 3.14 PDF of the instantaneous sliding and rolling probability over a time period of 7 s (Re = 200, *I* = 9.0%, coverage degree = 50%, $D_{drug}/D_{carrier}$ = 5/100, surface treatment: TC 8h)......................... 86

Fig. 3.15 Data points of *Ratio* in turbulent flow as a function of position angle for different snapshots (Re = 200, *I* = 9.0%, coverage degree = 50%, $D_{drug}/D_{carrier}$ = 5/100, surface treatment: TC 8h). 87

Fig. 3.16 Schematic diagram of a drug particle sitting on a rough wall.... 90

Fig. 3.17 The relationship between the contact distance and the asperity distance, the size ratio and the particle height. a) and b): size ratio fixed, c) and d): asperity distance fixed, R_{drug} = 2.5 μm for all cases. 94

Fig. 3.18 Computational domain with applied boundary conditions for the rough wall simulation. 95

Fig. 3.19 Simulated drag and lift coefficients of the drug particle with increasing domain size in stream-wise (a), the lateral (b) and the vertical (c) directions (Re = 10, $R_{cylinder}/R_{drug}$ = 1.25 μm/2.5 μm, *L* = 4 μm, initial domain size: $x/D_d = y/D_d = 10$, $z/D_d = 12$). The definition of drag and lift coefficients are based on the inlet velocity and the particle diameter. 96

Fig. 3.20 Mesh of the fluid domain for rough wall simulations; resolution: 40 grids cells of the finest mesh per particle diameter with three-level grid refinements; domain size: $x/D_d = 14$, $y/D_d = 10$, $z/D_d = 14$. 97

Fig. 3.21 The wall induced shear flow around one particle residing on different roughness structures. a): the particle attach to a plane wall. b) and c): rough elements with the same asperity distance but varying size ratios. b) and d): rough elements with the same size ratio but varying asperity distances. Re = 10 for all cases. 98

Fig. 3.22 Velocity profiles of the fluid nodes on the line *A* in Fig. 3.21. 'Rough wall' corresponds to Case b, and 'Plane wall' corresponds to Case a in Fig. 3.21. The straight dashed line indicates the height of particle. Re = 10 for both cases. 98

Fig. 3.23 The hydro-torque-coefficient as a function of the particle Reynolds number under various shear flow conditions. The straight solid line denotes the analytical result by Hubbe (1984). The square denotes the linear shear flow and the particle has close contact with the wall (Section 2.2). The circle denotes the wall induced shear flow where the particle has close contact with the wall (Fig. 3.21a). The triangle denotes the wall induced shear flow with a rough wall (Fig. 3.21b) ($R_{cylinder}/R_{drug}$ = 1.25 μm/2.5 μm, *L* = 4 μm). 100

Fig. 3.24 The hydro-torque-coefficient for different rough structures as a function of the contact distance under the wall induced shear flow. Square: varying the asperity distance with fixed size ratio (Fig. 3.21 Case b and d) (Re = 10, $R_{cylinder}/R_{drug}$ = 1.25 μm/2.5 μm). Triangle: varying the size ratio with fixed asperity distance

(Fig. 3.21 Case b and c) (Re = 10, R_{drug} = 2.5 µm, *L* = 4 µm). Cycle: varying the asperity distance with fixed size ratio (Fig. 3.21 Case b and d) (Re = 3.5, $R_{cylinder}/R_{drug}$ = 1.25 µm/2.5 µm). 101

Fig. 3.25 Drag and lift coefficients of the particle as a function of the contact distance for different rough structures. a) and b): the roughness varies in asperity distance with a fixed size ratio (Re = 10, $R_{cylinder}/R_{drug}$ = 1.25 µm/2.5 µm), c) and d): the roughness varies in size ratio with a fixed asperity distance (Re = 10, R_{drug} = 2.5 µm, *L* = 4 µm). The definition of drag and lift coefficients are based on the inlet velocity and the particle diameter. 103

Fig. 3.26 Rolling and sliding ratios of the drug particle as a function of the contact distance with a fixed size ratio ($R_{cylinder}/R_{drug}$ = 1.25 µm/2.5 µm, surface treatment: TC 8h). 104

Fig. 3.27 Rolling and sliding ratios of the particle as a function of the size ratio with a fixed asperity distance (*L* = 4 µm, R_{drug} = 2.5 µm, Re = 10, surface treatment: TC 8h). 105

Fig. 3.28 *Ratio* as a function of the contact distance with a fixed size ratio for two particle Reynolds numbers ($R_{cylinder}/R_{drug}$ = 1.25 µm/2.5 µm, surface treatment: TC 8h). 107

Fig. 4.1 Collision of a particle cluster to the solid wall (coverage degree = 50%, $D_{drug}/D_{carrier}$ = 5/100). 109

Fig. 4.2 The compression and recovery phases of the particle-wall collision. 111

Fig. 4.3 Schematic diagram of a compressed elastic carrier particle with one drug particle attached; left: velocity vectors; right: force vectors.. 112

Fig. 4.4 Maximum drug inertia force in *y*-direction as a function of the impact angles (coverage degree = 50%, $D_{drug}/D_{carrier}$ = 5/100, μ_w = 0.1, U_0 = 10 m/s)... 122

Fig. 4.5 Friction force of the carrier as a function of compression distance (coverage degree = 50%, $D_{drug}/D_{carrier}$ = 5/100, α = 80°, μ_w = 0.1, U_0 = 10 m/s).. 123

Fig. 4.6 Instantaneous velocities of the carrier sphere as a function of compression distance, left: normal velocity, right: angular and tangential velocities (coverage degree = 50%, $D_{drug}/D_{carrier}$ = 5/100, α = 80°, μ_w = 0.1, U_0 = 10 m/s). 124

Fig. 4.7 Normal inertia force on the drug particles as a function of the position angle for different impact angles (coverage degree = 50%, $D_{drug}/D_{carrier}$ = 5/100, μ_w = 0.1, U_0 = 10 m/s). 125

Fig. 4.8 Normal inertia force on the drug particles as a function of the position angle for different friction coefficients between the carrier and the wall (coverage degree = 50%, $D_{drug}/D_{carrier}$ = 5/100, α = 10°, U_0 = 10 m/s). 125

Fig. 4.9 Tangential inertia force on the drug particles as a function of the position angle for different impact angles (coverage degree = 50%, $D_{drug}/D_{carrier}$ = 5/100, μ_w = 0.1, U_0 = 10 m/s). 126

Fig. 4.10 Tangential inertia force on the drug particles as a function of the position angle for different friction coefficients between the carrier and the wall (coverage degree = 50%, $D_{drug}/D_{carrier}$ = 5/100, α = 10°, U_0 = 10 m/s). 127

Fig. 4.11 The lift-off probability of drug particles as a function of the impact angles (coverage degree = 50%, $D_{drug}/D_{carrier}$ = 5/100, μ_w = 0.1, U_0 = 10 m/s, surface treatment: TC 8h). 128

Fig. 4.12 Normal inertia force on non-lift-off drug particles as a function of the position angle (coverage degree = 50%, $D_{drug}/D_{carrier}$ = 5/100, α = 10°, μ_w = 0.1, U_0 = 10 m/s). 129

Fig. 4.13 Tangential inertia force and friction force on drug particles as a function of the position angle (coverage degree = 50%, $D_{drug}/D_{carrier}$ = 5/100, α = 10°, μ_w = 0.1, U_0 = 10 m/s, surface treatment: TC 8h). 130

Fig. 4.14 The left and right parts of Eq. 4.26 (Rolling) on drug particles as a function of the position angle (coverage degree = 50%, $D_{drug}/D_{carrier}$ = 5/100, α = 10°, μ_w = 0.1, U_0 = 10 m/s, surface treatment: TC 8h). 130

Fig. 4.15 Data points of *Ratio* (coverage degree = 50%, $D_{drug}/D_{carrier}$ = 5/100, α = 10°, μ_w = 0.1, U_0 = 10 m/s, surface treatment: TC 8h). 131

Fig. 1.1 Summary of multi-scale approach for inhaler optimisation and design. 4

Fig. 1.2 Geometry of a typical swirl-flow inhaler device (left, taken from Donovan et al. 2012) and numerical grid used for the inhaler discretization (right, Sommerfeld & Schmalfuß, 2015). 8

Fig. 1.3 Calculated flow field of the inhaler; a) total velocity modulus and velocity vectors near the inhaler wall; b) turbulent kinetic energy energy (colour scale: m^2/s^2); c) representative particle trajectories for mono-sized particles through the inhaler; (100 L/min) (Sommerfeld & Schmalfuß, 2015). 8

Fig. 2.1 Directions of discrete equilibrium distribution function of the D3Q19 model. 13

Fig. 2.2 Treatment of the wall boundary condition on the particle surface applying the bounce-back approach: (a) stepwise representation of the particle surface inscribing the given geometry; (b) curved-wall boundary condition using the exact wall distance q between fluid node (x_{F00}) and obstacle surface (x_W) (Dietzel & Sommerfeld, 2013). 15

Fig. 2.3 Local grid refinement of a carrier particle covered by many small particles. 17

Fig. 2.4 Definition of node types at the interface between coarse and fine grid sections (Dietzel & Sommerfeld, 2013). 19

Fig. 2.5 Nodes around two particles near contact: the cycles indicate the fluid nodes far away the particle; the squares indicate the adjacent fluid nodes near the particle surface; the triangles indicate the solid nodes inside the particle; the stars indicate the solid-fluid nodes near its neighbouring particle. 20

Fig. 2.6 Boundary conditions for the simulation of a particle attach to the wall under the linear shear flow; the moving wall indicates the full-slip boundary condition; the outlet boundary has zero gradients for all parameters. 22

Fig. 2.7 Discretized mesh of a particle attach to the wall, 40 grids cells of the finest mesh pro particle diameter with three-level grid refinement (x,y,z refer to the length, width and height of the fluid domain). 24

Fig. 2.8 Domain size validation for a particle attached to a plane wall in a linear shear flow; domain size normalized by particle diameter; upper row: variation of domain size in stream-wise direction for constant dimensions in the lateral and vertical directions (y/D = 12, z/D = 12); middle row: variation of lateral dimension of the domain for x/D = 18, z/D = 12; lower row: variation of vertical dimension of the domain for x/D = 18, y/D = 12; left column: drag coefficient; right column: coefficient for slip-shear lift (3 refinement levels, particle Reynolds number Re = 0.01, shear Reynolds number Re_S = 0.02).. 25

Fig. 2.9 Drag coefficient C_D of a particle attached to a wall as a function of particle Reynolds number *Re*, comparison of a universal correlation (Eq. 2.17) based on the result of O`Neill (1968) with several simulation data obtained by different numerical methods (Derksen and Larsen, 2011; Liu et al., 2011; Zeng et al., 2009).29

Fig. 2.10 Lift coefficient C_{LS} of a particle attached to a wall as a function of the shear Reynolds number Re_S, comparison of analytic results of Leighton and Acrivos (1985) for a wall attached fixed sphere and Saffman (1965) for a freely rotating particle in an unbounded linear shear flow with several simulation data obtained by different numerical methods (Derksen and Larsen, 2011; Zeng et al., 2009).. 29

Fig. 2.11 Computational domain with applied boundary conditions. 32

Fig. 2.12 Simulated forces on the fine drug particles in stream-wise (left column) and vertical (right column) direction at different angular positions on the carrier particle; upper row: variation of grid size with increasing resolution, i.e. cells per drug particle diameter ($x/D_{carrier}$ = 7.8, $y/D_{carrier}$ = $z/D_{carrier}$ = 6.5); middle row: variation of stream-wise dimension of the domain for $y/D_{carrier}$ = $z/D_{carrier}$ = 6.5; lower row: variation of lateral dimension of the domain for $x/D_{carrier}$ = 7.8 (Re = 10, D_{drug}/ $D_{carrier}$ = 10/100, coverage degree = 25%, 242 drug particles)... 34

Fig. 2.13 Illustration of forces acting on the fine drug particles positioned on the large carrier particle. 36

Fig. 2.14 Flow field about the particle cluster and resulting total forces on the drug particles for three particle Reynolds numbers; left column: total force vector on drug particles; middle column:

streamlines over the particle cluster; right column: experiment measurement by Taneda (1956) (coverage degree = 50%, $D_{drug}/D_{carrier}$ = 5/100). 37

Fig. 2.15 Comparison of the drag coefficient resulting from present simulation results for a particle cluster with the correlation of Schiller and Naumann (1933) for a sphere (particle diameters $D_{cluster}$ = D_{sphere} = 110 μm, coverage degree 10% and 50%, $D_{drug}/D_{carrier}$ = 5/100). 39

Fig. 2.16 Temporal variation of stream-wise force on a single drug particle at a position angle of 61.5° for two Reynolds numbers (coverage degree = 50%, $D_{drug}/D_{carrier}$ = 5/100, Δt = 0.7 ms). 41

Fig. 2.17 Four times random distribution of drug particles (coverage degree = 50%, $D_{drug}/D_{carrier}$ = 5/100). 42

Fig. 2.18 Total force on all the drug particles in dependence of position angle for four different random distributions (coloured dots) and resulting polynomial fitting curve (Re = 100, coverage degree = 50%, $D_{drug}/D_{carrier}$ = 5/100). 42

Fig. 2.19 PDF of total force between position angle 40 – 60 degree; Ftotal; mean = 2.73 nN, standard deviation = 0.36 nN (Re = 100, coverage degree = 50%, Ddrug/Dcarrier = 5/100). 43

Fig. 2.20 Fitting curves for the normal force on the drug particles as a function of position angle for different Reynolds numbers; a) low Re regime, b) high Re regime (coverage degree = 50%, $D_{drug}/D_{carrier}$ = 5/100). 44

Fig. 2.21 Flow field about the particle cluster and resulting direction of total fluid forces on the drug particles for Re = 0.5 (coverage degree = 50%, $D_{drug}/D_{carrier}$ = 5/100). 45

Fig. 2.22 Magnitude and angular location of maximum normal force determined from the fitting curves in dependence of Reynolds number (coverage degree = 50%, $D_{drug}/D_{carrier}$ = 5/100) 46

Fig. 2.23 Standard deviation of the normal force on drug particles in dependence of position angle (Re = 200, coverage degree = 50%, $D_{drug}/D_{carrier}$ = 5/100). 46

Fig. 2.24 Tangential force on the drug particles as a function of position angle for different particle Reynolds numbers (coverage degree = 50%, $D_{drug}/D_{carrier} = 5/100$) 47

Fig. 2.25 Fitting curves for the normal force on the drug particles as a function of position angle for different degree of coverage (Re = 100, $D_{drug}/D_{carrier} = 5/100$). 49

Fig. 2.26 Zoom of the flow structure around the particle cluster for different coverage, a) 10%, b) 50% (Re = 200, $D_{drug}/D_{carrier}$ = 5/100)... 49

Fig. 2.27 Simulation data and fitting curves for the normal force on the drug particles as a function of position angle for different size ratio (Re = 200, coverage degree = 25%). 50

Fig. 2.28 Comparison of plug and shear flow about the particle cluster at identical Reynolds number (Re = 70); (a) normal forces in dependence of the position angle; (b) flow structure for the plug flow; (c) flow structure for the shear flow (coverage degree = 50%, $D_{drug}/D_{carrier} = 5/100$).. 52

Fig. 2.29 Velocity contour in the cross section area of the grid by the grid generated turbulence method (*porosity = 0.64*)......................... 54

Fig. 2.30 Velocity contour along the stream-wised direction by the grid generated turbulence method (*porosity = 0.64*)......................... 54

Fig. 2.31 Velocity fluctuations as a function of the downstream distance (*porosity = 0.64*)... 55

Fig. 2.32 Flow field around a particle under the HIT plus a plug flow; left: I = 4.93%; right: I = 49.22% (Re = 100)................................... 56

Fig. 2.33 Mean drag coefficient on a spherical particle as a function of the particle Reynolds number for different turbulence intensities... 57

Fig. 2.34 Turbulence intensity as a function of the forcing amplitude of the spectral forcing scheme (Re = 100). 58

Fig. 2.35 Instantaneous colour contours of the velocity component in x-direction (stream-wise direction) at the inlet boundary of the computational domain at the end of the simulation, i.e. after N = 84,500 time steps (U_{mean} = 30 m/s, I = 15.5% (in the center of the domain), integral time scale T_{int} = 60 s).................................... 62

Fig. 2.36 Probability density distribution of the velocity components on the fluid node in the middle of fluid domain; U_x denotes the velocity component in the stream-wised direction; U_y and U_z signify the velocity components in the lateral direction (U_{mean} = 30 m/s, I = 15.5%, averaging period 64,500 to 84,500 time steps, T_{int} = 60 s). 63

Fig. 2.37 Decaying of the turbulence intensity along the stream-wised direction by the digital filtering technique for different fluid velocities (k = 11 m^2/s^2). 64

Fig. 2.38 Force vectors and streamlines of the particle cluster for the laminar and turbulence flows (Re = 200, coverage degree = 50%, $D_{drug}/D_{carrier}$ = 5/100, time step N = 75,000). 65

Fig. 2.39 Temporal variation of the normal force on the drug particle which has the largest time averaged normal force (position angle = 85°) for both the laminar and turbulent flows (Re = 200, coverage degree = 50%, $D_{drug}/D_{carrier}$ = 5/100). 66

Fig. 3.1 Spherical particle deposited on an ideal plane wall with contact area and relevant forces. 68

Fig. 3.2 Tangential force and friction force on drug particles as a function of position angle (Re = 200, coverage degree = 50%, $D_{drug}/D_{carrier}$ = 5/100, surface treatment: TC 8h). 74

Fig. 3.3 Sliding probability of drug particles as a function of Reynolds number for different surface treatment methods ($D_{drug}/D_{carrier}$ = 5/100, coverage degree = 10%). 75

Fig. 3.4 Sliding probability of drug particles as a function of the Reynolds number for different coverage degrees ($D_{drug}/D_{carrier}$ = 5/100, surface treatment: TC 8h). 76

Fig. 3.5 Contact radius of drug particles as a function of the position angle (Re = 200, coverage degree = 50%, $D_{drug}/D_{carrier}$ = 5/100, surface treatment: TC 8h). 77

Fig. 3.6 The comparison of the numerical calculated hydrodynamic torque and the analytical solution by Hubbe (Eq. 3.5) as a function of position angle (Re = 200, coverage degree = 50%, $D_{drug}/D_{carrier}$ = 5/100, surface treatment: TC 8h). 78

Fig. 3.7 The numerical calculated hydrodynamic torque as a function of position angle for different degree of coverage (Re = 200, $D_{drug}/D_{carrier}$ = 5/100, surface treatment: TC 8h)........................ 79

Fig. 3.8 Fluid dynamic torque (left hand side of Eq. 3.4) and adhesion torque (right hand side of Eq. 3.4) as a function of the position angle (Re = 200, coverage degree = 50%, $D_{drug}/D_{carrier}$ = 5/100, surface treatment: TC 8h). 80

Fig. 3.9 The rolling probability of drug particles as a function of the Reynolds number for different surface treatment methods ($D_{drug}/D_{carrier}$ = 5/100, coverage degree = 10%)......................... 81

Fig. 3.10 The rolling probability of drug particles as a function of the Reynolds number at different coverage degrees ($D_{drug}/D_{carrier}$ = 5/100, surface treatment: TC 8h). 82

Fig. 3.11 Detachment probability due to sliding and rolling as a function of position angle for different Reynolds numbers; a) coverage degree = 50%, b) coverage degree = 10%, ($D_{drug}/D_{carrier}$ = 5/100, surface treatment: TC 8h). 83

Fig. 3.12 Data points of *Ratio*, Eq. 3.10 (Re = 100 and 200, coverage degree = 10%, $D_{drug}/D_{carrier}$ = 5/100, surface treatment: TC 8h). 85

Fig. 3.13 Instantaneous sliding and rolling probability of the drug particles in turbulent flow over a time of 7 s (Re = 200, I = 9.0%, coverage degree = 50%, $D_{drug}/D_{carrier}$ = 5/100, surface treatment: TC 8h). 86

Fig. 3.14 PDF of the instantaneous sliding and rolling probability over a time period of 7 s (Re = 200, I = 9.0%, coverage degree = 50%, $D_{drug}/D_{carrier}$ = 5/100, surface treatment: TC 8h)........................ 86

Fig. 3.15 Data points of *Ratio* in turbulent flow as a function of position angle for different snapshots (Re = 200, I = 9.0%, coverage degree = 50%, $D_{drug}/D_{carrier}$ = 5/100, surface treatment: TC 8h). 87

Fig. 3.16 Schematic diagram of a drug particle sitting on a rough wall.... 90

Fig. 3.17 The relationship between the contact distance and the asperity distance, the size ratio and the particle height. a) and b): size ratio fixed, c) and d): asperity distance fixed, R_{drug} = 2.5 µm for all cases.. 94

Fig. 3.18 Computational domain with applied boundary conditions for the rough wall simulation. 95

Fig. 3.19 Simulated drag and lift coefficients of the drug particle with increasing domain size in stream-wise (a), the lateral (b) and the vertical (c) directions (Re = 10, $R_{cylinder}/R_{drug}$ = 1.25 μm/2.5 μm, *L* = 4 μm, initial domain size: $x/D_d = y/D_d = 10$, $z/D_d = 12$). The definition of drag and lift coefficients are based on the inlet velocity and the particle diameter. 96

Fig. 3.20 Mesh of the fluid domain for rough wall simulations; resolution: 40 grids cells of the finest mesh per particle diameter with three-level grid refinements; domain size: $x/D_d = 14$, $y/D_d = 10$, $z/D_d = 14$. 97

Fig. 3.21 The wall induced shear flow around one particle residing on different roughness structures. a): the particle attach to a plane wall. b) and c): rough elements with the same asperity distance but varying size ratios. b) and d): rough elements with the same size ratio but varying asperity distances. Re = 10 for all cases. . 98

Fig. 3.22 Velocity profiles of the fluid nodes on the line *A* in Fig. 3.21. ‘Rough wall’ corresponds to Case b, and ‘Plane wall’ corresponds to Case a in Fig. 3.21. The straight dashed line indicates the height of particle. Re = 10 for both cases. 98

Fig. 3.23 The hydro-torque-coefficient as a function of the particle Reynolds number under various shear flow conditions. The straight solid line denotes the analytical result by Hubbe (1984). The square denotes the linear shear flow and the particle has close contact with the wall (Section 2.2). The circle denotes the wall induced shear flow where the particle has close contact with the wall (Fig. 3.21a). The triangle denotes the wall induced shear flow with a rough wall (Fig. 3.21b) ($R_{cylinder}/R_{drug}$ = 1.25 μm/2.5 μm, *L* = 4 μm). 100

Fig. 3.24 The hydro-torque-coefficient for different rough structures as a function of the contact distance under the wall induced shear flow. Square: varying the asperity distance with fixed size ratio (Fig. 3.21 Case b and d) (Re = 10, $R_{cylinder}/R_{drug}$ = 1.25 μm/2.5 μm). Triangle: varying the size ratio with fixed asperity distance (Fig. 3.21 Case b and c) (Re = 10, R_{drug} = 2.5 μm, *L* = 4 μm). Cycle: varying the asperity distance with fixed size ratio (Fig.

3.21 Case b and d) (Re = 3.5, $R_{cylinder}/R_{drug}$ = 1.25 μm/2.5 μm). 101

Fig. 3.25 Drag and lift coefficients of the particle as a function of the contact distance for different rough structures. a) and b): the roughness varies in asperity distance with a fixed size ratio (Re = 10, $R_{cylinder}/R_{drug}$ = 1.25 μm/2.5 μm), c) and d): the roughness varies in size ratio with a fixed asperity distance (Re = 10, R_{drug} = 2.5 μm, L = 4 μm). The definition of drag and lift coefficients are based on the inlet velocity and the particle diameter. 103

Fig. 3.26 Rolling and sliding ratios of the drug particle as a function of the contact distance with a fixed size ratio ($R_{cylinder}/R_{drug}$ = 1.25 μm/2.5 μm, surface treatment: TC 8h). 104

Fig. 3.27 Rolling and sliding ratios of the particle as a function of the size ratio with a fixed asperity distance (L = 4 μm, R_{drug} = 2.5 μm, Re = 10, surface treatment: TC 8h). 105

Fig. 3.28 *Ratio* as a function of the contact distance with a fixed size ratio for two particle Reynolds numbers ($R_{cylinder}/R_{drug}$ = 1.25 μm/2.5 μm, surface treatment: TC 8h). 107

Fig. 4.1 Collision of a particle cluster to the solid wall (coverage degree = 50%, $D_{drug}/D_{carrier}$ = 5/100). 109

Fig. 4.2 The compression and recovery phases of the particle-wall collision. 111

Fig. 4.3 Schematic diagram of a compressed elastic carrier particle with one drug particle attached; left: velocity vectors; right: force vectors. 112

Fig. 4.4 Maximum drug inertia force in y-direction as a function of the impact angles (coverage degree = 50%, $D_{drug}/D_{carrier}$ = 5/100, μ_w = 0.1, U_0 = 10 m/s). 122

Fig. 4.5 Friction force of the carrier as a function of compression distance (coverage degree = 50%, $D_{drug}/D_{carrier}$ = 5/100, α = 80°, μ_w = 0.1, U_0 = 10 m/s). 123

Fig. 4.6 Instantaneous velocities of the carrier sphere as a function of compression distance, left: normal velocity, right: angular and tangential velocities (coverage degree = 50%, $D_{drug}/D_{carrier}$ = 5/100, α = 80°, μ_w = 0.1, U_0 = 10 m/s). 124

Fig. 4.7 Normal inertia force on the drug particles as a function of the position angle for different impact angles (coverage degree = 50%, $D_{drug}/D_{carrier}$ = 5/100, μ_w = 0.1, U_0 = 10 m/s). 125

Fig. 4.8 Normal inertia force on the drug particles as a function of the position angle for different friction coefficients between the carrier and the wall (coverage degree = 50%, $D_{drug}/D_{carrier}$ = 5/100, α = 10°, U_0 = 10 m/s). 125

Fig. 4.9 Tangential inertia force on the drug particles as a function of the position angle for different impact angles (coverage degree = 50%, $D_{drug}/D_{carrier}$ = 5/100, μ_w = 0.1, U_0 = 10 m/s). 126

Fig. 4.10 Tangential inertia force on the drug particles as a function of the position angle for different friction coefficients between the carrier and the wall (coverage degree = 50%, $D_{drug}/D_{carrier}$ = 5/100, α = 10°, U_0 = 10 m/s). 127

Fig. 4.11 The lift-off probability of drug particles as a function of the impact angles (coverage degree = 50%, $D_{drug}/D_{carrier}$ = 5/100, μ_w = 0.1, U_0 = 10 m/s, surface treatment: TC 8h). 128

Fig. 4.12 Normal inertia force on non-lift-off drug particles as a function of the position angle (coverage degree = 50%, $D_{drug}/D_{carrier}$ = 5/100, α = 10°, μ_w = 0.1, U_0 = 10 m/s). 129

Fig. 4.13 Tangential inertia force and friction force on drug particles as a function of the position angle (coverage degree = 50%, $D_{drug}/D_{carrier}$ = 5/100, α = 10°, μ_w = 0.1, U_0 = 10 m/s, surface treatment: TC 8h). 130

Fig. 4.14 The left and right parts of Eq. 4.26 (Rolling) on drug particles as a function of the position angle (coverage degree = 50%, $D_{drug}/D_{carrier}$ = 5/100, α = 10°, μ_w = 0.1, U_0 = 10 m/s, surface treatment: TC 8h). 130

Fig. 4.15 Data points of *Ratio* (coverage degree = 50%, $D_{drug}/D_{carrier}$ = 5/100, α = 10°, μ_w = 0.1, U_0 = 10 m/s, surface treatment: TC 8h). 131

List of Tables

Table 2.1 Domain size specified in terms of carrier particle size and the number of cells for the coarse base-grid, as well as the total number of grid cells used for the fluid domain. 35

Table 3.1 Material properties of drug and carrier particles used in the simulations. 70

Table 3.2 Measured adhesion force via AFM (atomic force microscope), wall friction angle and coefficient (mean values und standard deviations obtained out of 3 × 1250 measurements) and adhesion surface energy (mean value and standard deviation out of 20 measurements) for modified glass beads (Cui, et al., 2014). 72

Table 4.1 Velocities for Case I. 115

Table 4.2 Velocities for Case II. 120

Table 4.3 Velocities for Case III. 120

Bibliography

Al-Bender, F. & Moerlooze, K. D., 2008. A model of the transient behavior of the tractive rolling contacts. *Advances in Tribology,* Volume 2008, p. Article ID 214894.

Alemani, D., Chopard, B., Galceran, J. & Buffle, J., 2007. Study of three grid refinement methods in the Lattice Boltzmann framework for reactive-diffusive processes. *Int. J. Mod0. Phys. C,* 18(4).

Benzi, R., Succi, S. & Vergassola, M., 1992. The lattice Boltzmann equation: theory and applications. *Phys. Rep.,* Volume 222, pp. 145-197.

Bhatnagar, P. L., Gross, E. P. & Krook, M., 1954. A model for collision processes in gases. I. small amplitude processes in charged and neutral one-component systems. *Phys. Rev.,* 94(3), pp. 511-525.

Biasi, L., de los Reyes, A., Reeks, M. & de Santi, G., 1988. Use of a simple model for the interpretation of experimental data on particle resuspension in turbulent flows. *J. Aerosol Sci.,* Volume 32, pp. 1175-1200.

Bouzidi, M., Firdaouss, M. & Lallemand, P., 2001. Momentum transfer of a Boltzmann-lattice fluid with boundaries. *Phys Fluids,* Volume 13, pp. 2452-3459.

Chen, S. & Doolen, G. D., 1998. Lattice Boltzmann method for fluid flows. *Annu. Fluid Mech.,* Volume 30, pp. 329-364.

Chew, N. Y. K., Chan, H. -K., Bagster, D. F. & Mukhraiya, J., 2002. Characterization of pharmaceutical powder inhalers: estimation of energy input for powder dispersion and effect of capsule device configuration. *J. Aerosol Sci.,* Volume 33, pp. 999-1008.

Coates, M. S., Chan, H. -K., Fletcher, D. F. & Chiou, H., 2007. Influence of mouthpiece geometry on the aerosol delivery performance of a dry powder inhaler. *Pharm. Res.,* Volume 24, pp. 1450-1456.

Coates, M. S., Fletcher, D. F., Chan, H. -K. & Raper, J. A., 2004. Effect of design on the performance of a dry powder inhaler using computational fluid dynamics. Part 1: grid structure and mouthpiece length. *J. Pharm. Sci.,* Volume 93, pp. 2863-2876.

Crouse, B., 2003. *Lattice-Boltzmann fluid flow simulations on treedata structures.* Thesis, Technische Universität München.

Crowe, C. T., Schwarzkopf, J. D., Sommerfeld, M. & Tsuji, Y., 2012. *Multiphase flows with droplets and particles.* 2nd ed. Boca Raton: CRC Press.

Cui, Y., Schmalfuß, S. & Sommerfeld, M., 2013. *On the detachment of fine drug powder from carrier particles within an inhaler device.* Jeju, Korea, 8th International Conference on Multiphase Flow.

Cui, Y. et al., 2014. Towards the optimisation and adaptation of dry powder inhalers. *International Journal of Pharmaceutics,* 470(1-2), pp. 120-132.

Cui, Y. & Sommerfeld, M., 2012. *Forces on micron-sized particles randomly distributed on the surface of larger carrier particles.* Friedrichshafen, Germany, 7th International Conference for Conveying and Handling of Particulate Solids.

Cui, Y. & Sommerfeld, M., 2015. Forces on micron-sized particles randomly distributed on the surface of larger particles and possibility of detachment. *International Journal of Multiphase Flow,* Volume 72, pp. 39-52.

Cyrus, K. A. & Jonathan, R. C., 2010. Lattice-Boltzmann method for complex flows. *Annu. Rev. Fluid Mech.,* Volume 42, pp. 439-72.

de Koning, J. P., 2011. *Dry powder inhalation: technical and physiological aspects, prescribing and use,* PHD Thesis: University of Groningen.

Derjaguin, B., Muller, V. & Toporov, Y., 1975. Effect of contact deformations on the adhesion of particles. *Journal of Colloid and Interface Science,* 53(2), pp. 314-326.

Derksen, J. J. & Larsen, R. A., 2011. Drag and lift forces on random assemblies of wall-attached spheres in low-Reynolds-number shear flow. *J. Fluid Mech.,* Volume 673, pp. 548-573.

Dietzel, M. & Sommerfeld, M., 2009. LBM simulations on agglomerate transport and deposition. *AIP Conf. Proc.,* Volume 1207, pp. 796-801.

Dietzel, M. & Sommerfeld, M., 2013. Numerical calculation of flow resistance for agglomerates with different morphology by the Lattice-Boltzmann method. *Powder Technology,* Volume 250, pp. 122-137.

Djenidi, L., 2006. Lattice-Boltzmann simulation of grid-generated turbulence. *J. FLuid Mech.,* Volume 552, pp. 13-35.

Donovan, M. J., Kim, S. H., Raman, V. & Smyth, H. D., 2012. Dry powder inhaler device influence on carrier particle performance. *J. Pharm. Sci.,* 101(3), pp. 1097-107.

Ernst, M., Dietzel, M., Cui, Y. & Sommerfeld, M., 2013. *Lattice-Boltzmann simulations for analysing particle-scale phenomena.* Jeju, Korea, 8th International Conference on Multiphase Flow.

Ernst, M., Dietzel, M. & Sommerfeld, M., 2013. Simulation of the sedimentation and agglomeration of resolved particles. *Acta Mechanica,* Volume 224, pp. 2425-2449.

Ernst, M. & Sommerfeld, M., 2012. On the volume fraction effects of inertial colliding particles in homogeneous isotropic turbulence. *J. of FLuids Eng.,* Volume 134(3), 031302.

Eswaran, V. & Pope, S. B., 1988. A deterministic forcing scheme for direct numerical simulations of turbulence. *Comput. Fluids,* Volume 27, pp. 11-28.

Filippova, O. & Hänel, D., 1998. Boundary-fitting and local grid refinement for lattice-BGK models. *Int. J. Mod. Phys. C,* Volume 9, pp. 1271-79.

Filippova, O. & Hänel, D., 1998. Grid refinement for lattice-BGK models. *J. Comput. Phys.,* Volume 147, pp. 219-228.

Guingo, M. & Minier, J., 2008. A new model for the simulation of particle resuspension by turbulent flows based on a stochastic description of wall roughness and adhesion forces. *Journal of Aerosol Science,* Volume 39, pp. 957-973.

Guo, Z. & Shu, C., 2013. *Lattice Boltzmann Method and its Applications in Engineering.* 1st ed. Singapore: World Scientific Publishing Co. Pte. Ltd..

Guo, Z., Zheng, C. & Shi, B., 2002. An extrapolation method for boundary conditions in lattice Boltzmann method. *Physics of Fluids,* 14(6), pp. 2007-2010.

Hertz, H., 1896. Über die berührung fester elastischer Körper. *J. reine und angewandte Mathematik,* Volume 92, p. 156.

Hölzer, A. & Sommerfeld, M., 2009. Lattice Boltzmann simulations to determine drag, lift and torque acting on non-spherical particles. *Computers & Fluids,* Volume 38, pp. 572-589.

Hubbe, M. A., 1984. Theory of detachment of colloidal particles from flat surfaces exposed to flow. *Colloids and Surfaces,* Volume 12, pp. 151-178.

Huber, C., Gomaa, H. & Weigand, B., 2011. Application of a novel turbulence generator to multiphase flow computations. *High Performance Computing in Science and Engineering '10,* pp. 273-286.

Ibrahim, A. H., Dunn, P. F. & Qazi, M. F., 2008. Experiments and validation of a model for microparticle detachment from a surface by turbulent air flow. *Aerosol Science,* Volume 39, pp. 645-656.

Islam, N. & Gladki, E., 2008. Dry powder inhalers (DPIs) - a review of device reliability and innovation. *Int. J. Pharm.,* Volume 360, pp. 1-11.

Johnson, K. L., Kendall, K. & Roberts, A. D., 1971. Surface energy and the contact of elastic solids. *Proc. R. Soc. Lond. A,* Volume 324, pp. 301-313.

Kim, S. & Karilla, S., 1991. *Microhydrodynamics: principles and selected applications.* Boston: Butterworth Heinemann.

Klein, M., Sadiki, A. & Janicka, J., 2003. A digital filter based generation of inflow data for spatially developing direct numerical or large eddy simulations. *Journal of Computational Physics,* Volume 186, pp. 652-665.

Ladd, A. J. C., 1994. Numerical simulations of particulate suspensions via a discretized Boltzmann equation. Part 2. Numerical results. *Journal of Fluid Mechanics,* Volume 271, pp. 311-339.

Landau, L. D. & Lifshitz, E. M., 1986. Theory of Elasticity. In: *Course of Theoretical Physics.* s.l.:Elsevier, pp. 25-37.

Larsen, R., Eskin, D. & Derksen, J., 2010. *Lift and drag on agglomerates attached to walls.* Tampa, Florida, USA, May 30-June 4, 7th International Conference on Multiphase Flow, ICMF 2010.

Leighton, D. & Acrivos, A., 1985. The lift on a small sphere touching a plane in the presence of a simple shear flow. *Journal of Applied Mathematics and Physics,* Volume 36, pp. 174-178.

Liu, C.-N.et al., 2011. Drag coefficient of a spherical particle attached on a flat surface. *Aerosol Air Qual. Res.,* Volume 11, pp. 482-486.

Lund, T., Wu, X. & Squires, D., 1998. Generation of turbulent inflow data for spatially-developing boundary layer simulations. *J. Comp. Phys.,* Volume 140, pp. 233-258.

Newman, S. & Busse, W., 2002. Evolution of dry powder inhaler design, formulation, and performance. *Respiratory Medicine,* 96(5), pp. 293-304.

Nguyen, N. Q. & Ladd, A. J. C., 2002. Lubrication corrections for lattice-Boltzmann simulations of particle suspensions. *Phys. Rev. E,* Volume 66:046708.

O`Neill, M. E., 1968. A sphere in contact with a plane wall in a slow linear shear flow. *Chem. Eng. Sci.,* Volume 23, pp. 1293-1298.

Phares, D. J., Smedley, G. T. & Flagan, R. C., 2000. Effect of particle size and material properties on aerodynamic resuspension from surfaces. *J. Aerosol Sci.,* Volume 31, pp. 1335-1353.

Pietro, P., Gijs, O., Andreas, T. C. & Julian, C. R. H., 2006. Interaction and collisions between particles in a linear shear flow near a wall at low Reynolds number. *J. Fluid Mech.,* Volume 555, pp. 113-130.

Reeks, M. & Hall, D., 2001. Kinetic models for particle resuspension in turbulent flows: theory and measurement. *J. Aerosol Sci.,* Volume 32, pp. 31-39.

Reeks, M. W., Reed, J. & Hall, D., 1988. On the resuspension of small particles by a turbulent flow. *J. Phys. D: Appl. Phys.,* Volume 21, pp. 574-589.

Roos, F. W. & Willmarth, W. W., 1971. Some experimental results on sphere and disk drag. *AIAA Journal,* 9(2), pp. 285-291.

Saffman, P. G., 1965. The lift on a small sphere in a slow shear flow. *Journal of Fluid Mechanics,* 22(02), pp. 385-400.

Schiller, L. & Naumann, A., 1933. Über die grundlegende Berechnung bei der Schwerkraftaufbereitung. *Ver. Deut. Ing.,* Volume 44, pp. 318-320.

Smith, I. J. & Parry-Billings, M., 2003. The inhalers of the future? A review of dry powder devices on the market today. *Pulm. Pharmacol. Therapeut,* Volume 16, pp. 79-95.

Soltani, M. & Ahmadi, G., 1994. On particle adhesion and removal mechanisms in turbulent flows. *J. Adhesion Sci. Technol,* Volume 8, pp. 763-785.

Soltani, M. & Ahmadi, G., 1999. Detachment of Rough Particles with Electrostatic Attraction from Surfaces in Turbulent Flows. *J. Adhesion Sci. Technol.,* Volume 13, pp. 325-355.

Sommerfeld, M., 2010. Part 11. In: *Particle motion in fluids.* s.l.:VDI-Buch: VDI Heat Atlas, Springer Verlag Berlin/Heidelberg; ISBN 978-3-540-77877-9, pp. 1181-1196.

Sommerfeld, M. & Schmalfuß, S., 2015. Numerical analysis of carrier particle motion in a dry powder inhaler. *ASME Journal of Fluid Engineering.*

Sommerfeld, M., van Wachem, B. & Oliemans, R., 2008. Best parctice guidelines for computational fluid dynamics of dispersed multiphase flows. *ERCOFTAC,* Volume ISBN 978-91-633-3564-8, pp. 978-991.

Srichana, T., Martin, G. P. & Marriott, C., 1998. Dry powder inhalers: the influence of device resistance and powder formulation on drug and lactose deposition in vitro. *Eur. J. Pharm. Sci.,* Volume 7, pp. 73-80.

Steckel, H. & Müller, B. W., 1997. In vitro evaluation of dry powder inhalers I: drug deposition of commonly used devices. *Int. J. Pharm.,* Volume 154, pp. 19-29.

Sweeney, L. G. & Finlay, W. H., 2007. Lift and drag forces on a sphere attached to a wall in a Blasius boundary layer. *Aerosol Sci.,* Volume 38, pp. 131-135.

Taneda, S., 1956. Experimental investigation of the wake behind a sphere at low Reynolds numbers. *J. Phys. Soc. Japan,* 11(10), pp. 1104-1108.

Telko, M. J. & Hickey, A. J., 2005. Dry powder inhaler formulation. *Respiratory Care,* 50(9), pp. 1209-1227.

Uhlherr, P. H. T. & Sinclair, C. G., 1970. The effect of freestream turbulence on the drag coefficient of spheres. *Proc. CHEMECA,* Volume 1, p. 1.

Wang, L.-P., Wexler, A. S. & Zhou, Y., 1998. On the collision rate of small particles in isotropic turbulence. I. zero-inertia case. *Phys. Fluids,* Volume 10, pp. 266-276.

Wen, H. Y. & Kasper, G., 1989. On the kinetics of particle reentrainment from surfaces. *J. Aerosol Sci.,* Volume 20, pp. 483-498.

Zellnitz, S. et al., 2013. Preparation and characterization of physically modified glass beads used as model carriers in dry powder inhalers. *International Journal of Pharmaceutics,* Volume 447, pp. 132-138.

Zellnitz, S., Redlinger-Pohn, J. D., Schröttner, H. & Urbanetz, N. A., 2011. *Improving the performance of dry powder inhalers by ailoring interparticle interactions.* Edinburgh, Drug Delivery to the Lung (DDL22).

Zeng, L., Najjar, F., Balachandar, S. & Fischer, P., 2009. Forces on a finite-sized particle located close to a wall in a linear shear flow. *Physics of Fluids,* Volume 21, p. 033302.

Zhang, F., Reeks, M. & Kissane, M., 2013. Particle resuspension in turbulent boundary layers and the influence of non-gaussian removal forces. *J. Aerosol Sci.,* Volume 58, pp. 103-128.

Zhang, F., Reeks, M., Kissane, M. & Perkins, R., 2013. Resuspension of small particles from multilayer deposits in turbulent boundary layers. *J. Aerosol Sci.,* Volume 66, pp. 31-61.

Ziskind, G., Fichman, M. & Gutfinger, C., 1997. Adhesion moment model for estimating particle detachment from a surface. *J. Aerosol Sci.,* 28(4), pp. 623-634.

Curriculum Vitae

Personal Data

Name:	Yan Cui
Birthday:	19.11.1985
Sex:	Male
Marital Status:	Married, no Kids
Place of Birth:	Anhui, China
Nationality:	Chinese
Address:	Charlottenstr. 3, 06108 Halle, Germany

Education

10.2007 – 01.2010
Bergische Universität Wuppertal, Wuppertal, Germany
Master of Science, Computational Mechanical Engineering
Thesis: CFD-calculation for the flow around a 3D aircraft model

09/2003 – 06/2007
Huazhong University of Science & Technology, Wuhan, China
Bachelor of Science, Mechanical Design, Manufacturing & Automation
Thesis: Experimental study on the dynamic mechanical behaviour of combining sites within the CNC machine

Experience

09.2010 – 08.2016
Martin-Luther-Universität Halle-Wittenberg, Halle, Germany
Position: Research Assistant (Wissenshaftlicher Mitarbeiter) at the chair for mechanical process engineering.
Head of the chair: Prof. Dr. –Ing habil. Martin Sommerfeld
Working on the project “The importance of inter-particle interactions for the application of dry powder inhaler” within the scope of DFG SPP 1486 “Particle in Contact” and in corporation with COST Actions MP1404 SimInhale.

Journal Publications

Cui, Y. & Sommerfeld, M., 2016. Application of lattice-Boltzmann method for analysing detachment of micron-sized particles from carrier particles in turbulent flows (submitted to Flow, Turbulence & Combustion, July 2016).

Cui, Y. & Sommerfeld, M., 2015. Forces on micron-sized particles randomly distributed on the surface of larger particles and possibility of detachment. *Int. J. Multiphase Flow*, Volume 72, pp. 39-52.

Cui, Y., Schmalfuß, S., Zellnitz, S., Sommerfeld, M., Urbanetz, N., 2014. Towards the optimisation and adaptation of dry powder inhalers. *Int. J. Pharm.*, 470(1-2), pp. 120-132.

Conference Proceedings

Cui, Y. and Sommerfeld, M., 2016. Modelling carrier particle wall collision for predicting drug detachment efficiency inside dry powder inhalers. PARTEC 2016, Nuremberg, Germany, April 19.21.

Cui, Y., Schmalfuß, S., Sommerfeld, M., 2013. On the detachment of fine drug powder from carrier particles within an inhaler device. ICMF 2013, Jeju, Korea, Paper No. 438.

Ernst, M., Dietzel, M., Cui, Y., Sommerfeld, M., 2013. Lattice-Boltzmann simulations for analysing particle-scale phenomena. ICMF 2013, Jeju, Korea, Paper No. 441.

Cui, Y. and Sommerfeld, M., 2012. Forces on micron-sized particles randomly distributed on the surface of larger carrier particles. CHoPS 2012, Friedrichshafen, Germany, Paper No. 1067.

Halle (Saale), den 15.01.2016 Yan Cui

Erklärung

Hiermit erkläre ich an Eides statt, dass ich die vorliegende Arbeit selbständig und ohne fremde Hilfe angefertigt und keine anderen als die angegebenen Quellen und Hilfsmittel benutzt sowie die den benutzten Werken wörtlich und inhaltlich übernommenen Stellen als solche kenntlich gemacht habe.

Halle (Saale), den 15.01.2016 Yan Cui